Analysis of Degrading Concrete Structures: The Morandi Bridge, a Case Study

William D. Galik

A thesis submitted in partial fulfillment of the
requirements for the degree of

Master of Science in Civil Engineering

University of Washington
2021

Committee:
Paolo M. Calvi
Richard Wiebe
John F. Stanton

Program Authorized to Offer Degree:
Civil and Environmental Engineering

University of Washington

Abstract

Analysis of Degrading Concrete Structures: The Morandi Bridge, a Case Study

William D. Galik

Chair of the Supervisory Committee:
Paolo M. Calvi
Civil and Environmental Engineering

The concrete infrastructure of the United States is reaching its nominal design life. More than 65% of the highway bridges in the US are reinforced concrete or prestressed concrete construction and 20% of those bridges do not meet current minimum design standards. Damage in these structures often manifests as reinforcement corrosion, an insidious mechanism that may remain hidden until damage has progressed to an advanced state. Corrosion reduces reinforcement area, reduces bond strength, and induces concrete cracking. The deterioration process is exacerbated by live loads that increase over time. Cyclic live loads are especially damaging when paired with corrosion damage, reducing reinforcement fatigue life by magnitudes. The challenge of dealing with aging infrastructure must begin with the identification of at-risk structures. Failure of aging structures is often characterized by a lack of redundancy, defined as the ability of a structure to withstand the loss of a load-resisting component. In the case of load redistribution due to member failure, a structure may develop complex and unanticipated stress distributions. Proper tools

are needed to analyze the complex stress-states that arise upon load-redistribution due to member failure.

This study presents two analytical schemes for the analysis of combined corrosion and fatigue, based on experimental data from the literature. The methods can predict the fatigue life of corroded reinforcement if alternating stresses in the reinforcement are known. Additionally, this thesis reviews truss model theories for the prediction of a prestressed concrete member's response to combined loads, with a focus on the torsional response. The tools are implemented in a case study of the Morandi Bridge, which partially collapsed on August 14, 2018 in Genoa Italy, killing 43. Potential collapse mechanisms observed from surveillance footage are investigated with the aid of the corrosion, fatigue, and combined loading tools presented in this work. The results of the study suggest that failure of the Morandi Bridge could have originated in the cable stay due to the combined effect of corrosion and fatigue. After failure of a stay, the unbalanced structure would not have been able to redistribute the loads and the bridge's main deck would have failed in torsion.

TABLE OF CONTENTS

LIST OF TABLES

LIST OF FIGURES

FIGURE PAGE

ACKNOWLEDGMENTS

First, I would like to thank my thesis advisor, Professor Paolo Calvi, for providing me this opportunity and trusting me to tackle this challenge with him. His guidance and patience have made this an invaluable learning and growing experience. I must also mention my appreciation for University of Washington professors Richard Wiebe, John Stanton and Peter Mackenzie-Helnwein, whose teaching, mentorship and insight have extended far beyond what I could have hoped for when I first came to the University of Washington.

I would also like to thank my friends and classmates, who have made this adventure both rewarding and enjoyable. I could not imagine the last two years without my friends David Tyus, Matt Jenkins, Tatsu Sweet, Tanakij Hanmongkolpipat, Jacob Chekal, Katie Harris, Mike Carovillano and Nikki Redden.

Finally, I need to acknowledge the never-ending support of my family. My two awesome brothers, Matthew and John, constantly motivate me to become a better student, brother and friend. My parents, John and Tina, have given so much to me. This thesis surely would not have been completed without their support — not only during my time at UW, but throughout my development.

CHAPTER 1

INTRODUCTION

1.1 Motivation

The concrete infrastructure of the United States is reaching its nominal design life. More than 65% of the highway bridges in the US are reinforced concrete or prestressed concrete construction and 25% of those bridges were constructed over 50 years ago. In the years since, traffic volume and vehicle weights have increased steadily. Older methods of protecting concrete structures from environmental damage would not satisfy current quality standards. As such, engineers face the difficult challenge of assessing aging structures for corrosion and fatigue damage and determining appropriate remedial actions. This task can be difficult, as corrosion and fatigue of reinforced concrete structures are insidious damage mechanisms, often progressing undetected until sudden, catastrophic failure.

Many aging highway bridges were not designed to withstand the 80 kip maximum truck load that is standard in today's design practice [Jang (2018)]. With a steady increase in Average Daily Truck Traffic (ADTT) and Gross Vehicle Weights (GVW), these bridges are increasingly susceptible to damage from truck overloads. A 2017 study of bridge traffic in Pennsylvania [Lou et al. (2017)] revealed that, for some highways, up to 20% of truck traffic exceeds the 80 kip weight limit. A similar study of Illinois traffic [Jang (2018)] found that 10% of truck traffic exceeds the weight limit, requiring special permits. Lou [Lou et al. (2017)] has correlated the service life of prestressed concrete (PC), multi-span bridges with the ADTT and the number of overloaded trucks that travel the bridge daily, noting a significant drop in estimated service life if the percent of ADTT composed by overloaded trucks increases from 1%

to 10%. As many older bridges remain within common trucking corridors, fatigue damage is a concern.

Lou observed that the main cause of failure for PC bridges is deterioration at beam ends and construction joints (e.g., cracking, cover spalling, and tendon corrosion). Analysis of bridge data [Lou et al. (2017)] shows that bridge health declines rapidly after observation of visible cracks, suggesting that corrosion ingress often controls damage progression. When corrosion deterioration is combined with fatigue loads, the damage can become catastrophic, as both corrosion and fatigue cause brittle structural responses. Embrittlement is especially significant for old structures, whose strength capacity may be less than that of modern structures. The low design strength of the older bridges means that fewer fatigue cycles are required to fail at-risk bridge components. This fact is particularly concerning since Mohammadi [Mohammadi and Polepeddi (2000)] suggests that current procedures for granting overload permits to heavy trucks do not adequately consider cumulative fatigue damage.

Member failure due to corrosion and fatigue is more likely for aging structures. To prevent collapse, these at-risk structures must exhibit sufficient structural redundancy, which is the ability of a structure to redistribute load in the case of a component failure. However, many older structures adopted simple structural schemes that were statically determinate; such structures are easily analyzed but lack robustness. As such, the coupled effect of environmental degradation and fatigue damage poses an impending threat of sudden collapse for many aging buildings and bridges, which may not be able to effectively redistribute loads in the case of the failure of a critical structural member.

Examples of Structural Collapse The general issues outlined above are illustrated in this section by briefly discussing specific structural collapses.

In 1980, the roof of the Berlin Congress Hall partially collapsed, killing one. Corrosion of roof tendons is one reason cited for collapse [Helmerich and Zunkel (2014)]. Investigation reports identified that the roof tendons in the collapsed region were constructed with minimal cover protection, which was easily bypassed by constant moisture from a nearby fountain. The high moisture region accelerated the corrosion progression. Furthermore, tendon ducts were poorly grouted or not grouted at all. As will be discussed in Chapter 2, interaction between reinforcement and concrete paste produces a passive oxide layer on the surface of reinforcement that protects against corrosion onset. In the absence of grout, no such passive layer would have formed on the surface of the Berlin Congress Hall tendons.

In another example of corrosion failure, the Ynysygwas bridge collapsed in 1985, 32 years after construction. The bridge's single 60 ft span was constructed with the post-tensioned segmental method that is popular for its modularity. Collapse investigations reported high levels of tendon corrosion at the joints between bridge segments. Grout caps were missing in several locations and grout was voided or absent in about a quarter of the tendon ducts [Woodward (1988)]. Corrosion was initiated by chloride attack from the heavy use of de-icing salts on the bridge and testing showed that a non-expansive rust covered the surface of the fractured tendons, belying the outward appearance of structural soundness. The particularly damaging form of non-expansive corrosion will be discussed in Chapter 2.

An early example of structural robustness failure is the partial collapse of the 22-story Ronan Point apartment tower in 1968. A gas explosion in an 18th floor

apartment damaged some load-bearing walls, and was followed by the progressive collapse of an entire corner of the building.

1.2 Thesis Scope

The failures discussed above highlight the need for:

- Accurate tools for the identification of at-risk structures
- Increased familiarity with the analysis tools available for evaluation of corrosion, fatigue, and complicated stress-states that may arise in the case of a structural member failure

This work focuses on the second task, providing simplified tools for the analysis of corrosion, fatigue, and complex three-dimensional stress states. It is hoped that the simple analytical schemes within this thesis will become common knowledge for most structural engineers. To this end, a case study is performed on the Morandi Bridge, a prestressed concrete cable-stayed bridge that partially collapsed on August 14, 2018 after 51 years of service life. Forty-three people died as a result. Video footage suggests that failure originated in a cable stay, followed by torsional failure of the main deck, which was unable to resist the load redistribution from the stay loss. Post-collapse investigation revealed heavy corrosion on the tendons within the stay. This work's analysis investigates the combined levels of corrosion and fatigue that would have been required to fail the stay. The absence of extreme load events (e.g., impact or heavy winds) is assumed throughout the work. After the stay collapse is studied, the torsional capacity of the deck is investigated.

1.3 Thesis Outline

Chapter 1 presents motivation and outlines this work.

Chapter 2 reviews literature concerning corrosion of reinforced and prestressed concrete structures. A simple model is proposed for the static analysis of prestressed members subject to corrosion and creep.

Chapter 3 reviews two common prediction schemes for fatigue life. Each fatigue method is combined with experimental corrosion data (specific to bridge wire) to produce two analysis methods for combined corrosion and fatigue.

Chapter 4 reviews torsion theory. Torsion is not well understood by many students, but occurs commonly in structural responses.

Chapter 5 reviews truss models for the prediction of a beam's response to combined loads. Models from the literature are presented along with a truss model variation proposed by the author that uses some elements of the existing models. The author's proposed model has only been verified for combined torsion, shear, and axial loads. The inclusion of bending moments has not yet been implemented. A simpler model is presented that accounts for combined torsion, shear, bending moments and axial loads. This model is useful for 'back-of-the-envelope' calculations.

Chapter 6 implements the corrosion, fatigue, and combined loading theories into a case study of the Morandi Bridge. The stay collapse is predicted with the corrosion and fatigue models of Chapter 2 & 3, then the simple combined loading model from Chapter 5 predicts the torsional deck capacity, given the stay collapse.

Chapter 7 summarizes the outcomes of this work and suggests improvements.

CHAPTER 2

CORROSION DAMAGE OF REINFORCED CONCRETE STRUCTURES

2.1 Prevalance of Corrosion-Damaged Structures

A few examples of corrosion-based structural collapses were discussed in Chapter 1. Despite the continued occurence of corrosion incidents, there is a lack of resources that discuss corrosion of prestressed concrete, precisely because the stressing operation is designed to compress the concrete, providing a shield against destructive corrosion agents. However, improper construction can destroy this corrosion protection, allowing environmental deterioration to proceed - sometimes undetected - until costly rehabilitation is required, or worse, corrosion manifests as a brittle failure. This chapter discusses the corrosion process, from corrosion inititiation through the progression of damage in both reinforcing and concrete materials. Then, corrosion issues specific to prestressed construction techniques are discussed. Finally, a simple procedure for the analysis of corroded, prestressed elements is presented.

2.2 Corrosion Review

A brief review of corrosion is presented here, focusing on corrosion inducing factors and the effects of corrosion on the behavior of reinforced concrete structures. More information can be found elsewhere [Habibi (2017); Collins and Mitchell (1991)].

2.2.1 Corrosion Electrochemistry

Corrosion is an electrochemical process in which metals degrade via interactions with the environment. A chemically-balanced corrosion reaction requires two sub-

processes to occur: oxidation and reduction. In the oxidation process, metals lose electrons (and therefore mass). In the presence of enough water and oxygen, the extra electrons are consumed in the reduction reaction. Reinforced concrete provides these components; reinforcement provides a conductive surface and water in the concrete paste acts as an electrolyte. The corrosion onset of reinforcing bars may be delayed, or completely impeded, by a phenemonon called passification that occurs naturally for iron in basic (high pH) environments. Concrete paste typically has a pH near 12.5 that aids the development of thin protective oxide-layer at the surface of reinforcement. This oxide layer must be broken down before the oxidation of the metal can begin. Typically, the passive layer is destroyed by carbonation or chloride attack. Once the corrosion process initiates, its rate is dependent on the limiting components of the oxidation and reduction reactions. Though highly sensitive to environmental conditions, some common corrosion rates are shown in Fig. 2.1.

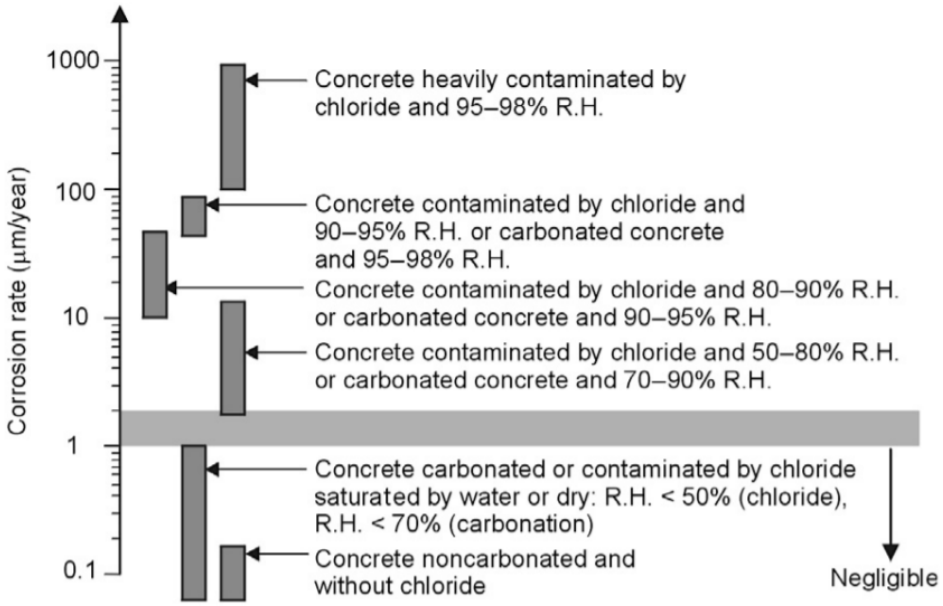

Figure 2.1: Common corrosion rates for varied environmental conditions, copied from [Bertolini et al. (2013)]

2.2.2 Corrosion Types

Though corrosion can take various forms, two in particular are relevant for reinforced concrete structures: uniform and pitting corrosion. The form that corrosion takes has been shown [Lee and Cho (2009)] to depend on the manner in which the reinforcement's passive layer is broken down; carbonation often results in uniform corrosion while chloride attack - such as may occur in marine environments - tends to produce corrosion pits. Uniform corrosion occurs with similar intensity over the entire bar surface whereas pitting corrosion is highly local (and therefore varies along the length of a reinforcing member) and difficult to detect. A schematic of the two corrosion types is shown in Fig. 2.2. Though these two corrosion forms result from different environmental attacks and create different rust by-products, it is not unlikely for the two to exist simultaneously throughout the same structure.

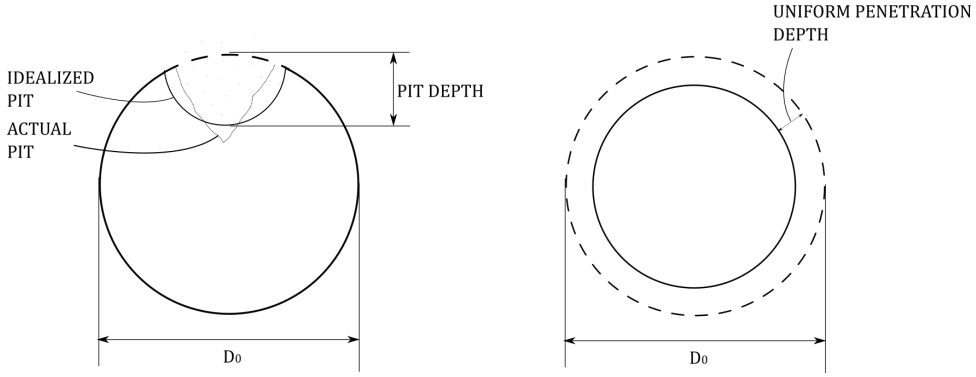

Figure 2.2: Idealization of corrosion pit geometry, adapted from [Stewart and Al-Harthy (2008)]

2.2.3 Corrosion Rate

The corrosion rate provides a quantitative description of corrosion phenomena, allowing engineers to make predictions for design and analysis purposes. Additionally, the corrosion rate is a controlling input for the determination of corroded reinforce-

ment mechanical properties, discussed in Section 2.2.4. The corrosion rate is often expressed in terms of the thickness of material lost per unit time (mm/yr). If predictions are to be made, it is helpful to understand relevant parameters that affect corrosion rates. Many researchers [Liu and Weyers (1998); Vu and Stewart (2000)] have postulated various rate relationships, most of which agree that concrete water content, ambient temperature, humidity, and cover depth are all important. Lu [Lu et al. (2008)] has lumped these factors into a single corrosion parameter, i_{corr}, which represents the corrosion current density at the onset of corrosion.

$$i_{corr}(t_0) = \frac{T_K H_r (w/c)}{d_c} \tag{2.1}$$

where:

T_K = Temperature in Kelvin

H_r = Relative humidity

w/c = water/cement ratio

d_c = cover depth

The corrosion penetration rate is commonly described by Faraday's law [Habibi (2017)], which assumes a constant thickness reduction throughout time based on the initial corrosion current density.

$$\frac{dr}{dt} = \frac{i_{corr}(t_0)}{nF} \tag{2.2}$$

where:

$\frac{dr}{dt}$ = corrosion penetration rate

n = electrons per mole of iron

F = Faraday's constant

It is noteworthy that some researchers [Lu et al. (2008); Li et al. (2011)] have suggested corrosion rates should decrease with time, noting that concrete pore water is consumed as corrosion progresses and that rust may fill the pores, preventing water access to the reinforcement. Despite this, a constant rate formulation is used in this work so that results can be readily compared to those of the finite element software used in Chapter 6, for which the formulation relies on Faraday's law.

It can be seen from Eq. 2.1 that the corrosion rate is assumed by researchers to be controlled by the oxygen and moisture supply (via w/c and H_r). It is uncertain to what extent corrosion rates increase upon cracking of concrete when the oxygen supply may no longer be the limiting reactant. Furthermore, the effect of crack width on corrosion rates is unclear. Some [Gerwick and Mehta (1982)] have suggested that cracks on the microscale are enough to magnify corrosion rates and others [Beeby (1983)] have surmised that any additional crack width beyond microcracking may not impact the corrosion rate. Collins [Collins and Mitchell (1991)] states that cracks transverse to the reinforcement are not as damaging as longitudinal cracks, because transverse cracks only bisect a reinforcement slice. Longitudinal cracks, on the other hand, provide corrosion agents access to an entire length of bar.

2.2.4 Mechanical Effects of Corrosion

Cover Cracking The by-products of uniform corrosion reactions vary depending on the amount of oxygen and carbon dioxide in the environment, but generally occupy a larger volume than iron, with a typical volume ratio of rust product to iron between 2-6. Expansion of the steel-concrete interface induces hoop tension in the concrete, which, depending on the severity of corrosion and volume ratio of by-product to iron, produces longitudinal concrete cracks that may reach the concrete

exterior surface given sufficient time. Cracking due to rust expansion is derived in Appendix A.

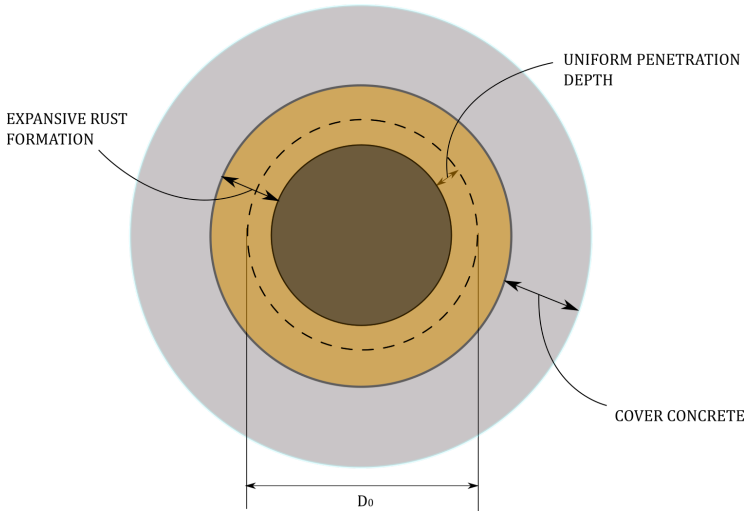

Figure 2.3: Radial expansion of corrosion product and resulting hoop tension in cover concrete, adapted from Habibi [Habibi (2017)]

Unlike uniform corrosion, pitting corrosion does not produce an expansive rust product [Habibi (2017)]. This makes pitting corrosion a particularly insidious degradation mode, as there is no cracking evidence to indicate the presence of underlying damage.

Bond Strength Bond between reinforcement and concrete allows the two materials to resist loads via composite action. The efficacy of this action is affected by reinforcement corrosion levels. Small corrosion levels tend to slightly increase the bond strength, likely because of the increased friction at the steel-concrete interface from low levels of rust expansion. However, intense corrosion significantly reduces bond strength because of poor adherence of flaky rust products as well as longitudinal cover cracking. A schematic of the effect is shown in Fig. 2.4.

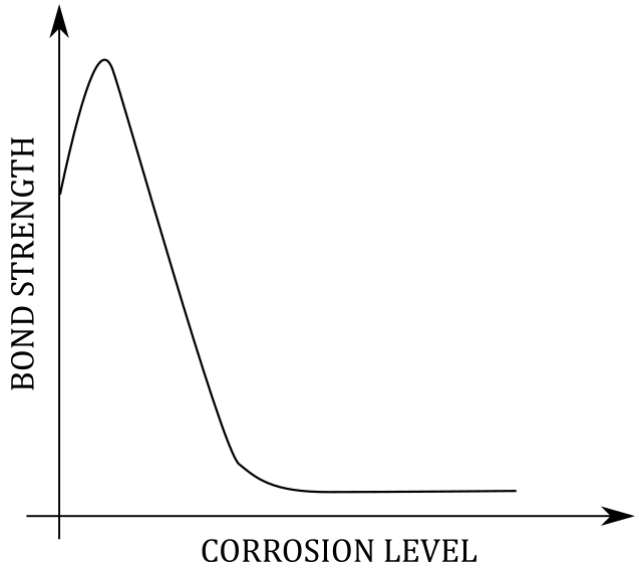

Figure 2.4: Schematic for the variation of bond strength with increased corrosion levels

Reduction of Reinforcement Mechanical Properties

Pitting Corrosion: Reinforcement subject to local corrosion damage has been observed to exhibit reduced strength and ductility. Many researchers [Morinaga (1996); Cairns et al. (2005); Lee and Cho (2009); Du et al. (2007)] have proposed relationships between average corrosion levels (i.e., fraction of coss-sectional area reduction due to corrosion) and mechanical properties. Generally, these relationships take the following form, where the empirical coefficients are provided in Table 2.1 from the results of various researchers.

$$f_y = (1 - \alpha_y \eta) f_{y0} \tag{2.3}$$

$$f_u = (1 - \alpha_u \eta) f_{u0} \tag{2.4}$$

$$\epsilon_u = (1 - \alpha_1 \eta) \epsilon_{u0} \tag{2.5}$$

where:

η = fractional reduction of reinforcement cross-section area from corrosion

$f_{y0}, f_{u0}, \epsilon_{u0}$ = yield strength, ultimate strength, ultimate strain of uncorroded bars

f_y, f_u, ϵ_u = yield strength, ultimate strength, ultimate strain of corroded bars

$\alpha_y, \alpha_u, \alpha_1$ = empirical coefficients, presented in Table 2.1

Table 2.1: Effect of pitting corrosion on mechanical properties on reinforcement

Researcher	α_y	α_u	α_1
Du	1.5	1.5	3.9
Cairns	1.2	1.1	3.0
Morinaga	1.7	1.8	6.0
Lee	2.0	1.6	2.6

Although Lee [Lee and Cho (2009)] has reported a reduction of reinforcement mechanical properties for uniform corrosion, the effect was not as significant as for pitting corrosion. This may be a result of the spatial variability of pitting corrosion. Maximum pitting depths may be considerably larger than the average penetration attack for which the reduction equations are formulated. The remainder of this work assumes that mechanical properties of reinforcement are only reduced if pitting corrosion is present.

2.3 Common Corrosion Issues with Prestressed Concrete

Much of the research summarized in Section 2.2 was performed for ordinary reinforced concrete. While the electrochemical corrosion process is no different for reinforced concrete or prestressed concrete, some researchers [Li et al. (2011)] have observed that corroded prestressed concrete structures deteriorate differently than

corroded reinforced concrete structures. Prestressed concrete structures exhibit minimal corrosion cracking, but often fail more catastrophically than reinforced concrete structures. Li et al. [Li et al. (2011)] attributes this to microstructural and geometrical differences in prestressed tendons that lead to preferential formation of pitting corrosion. Some corrosion issues for prestressed concrete technology are briefly reviewed here.

Prestressed concrete structures are designed to remain in compression throughout their service life. Collins et al. [Collins and Mitchell (1991)] suggest that carbonation of compressed concrete progresses too slowly to penetrate the cover depth within typical structure lifespans. Yet, many cases of corrosion problems have been observed for prestressed structures [Schupack and Suarez (1982)]. For example, the segmentally constructed Ynysygwas Bridge collapsed due to corrosion penetration at construction joints [Woodward (1988)]. High tendon stresses from post-tensioning operations (i.e., stress transfer at ends of prestressed members) may also lead to a network of longitudinal microcracks that provide entry to corrosion agents.

Another consequence of the high stresses experienced by prestressing wires is the potential for stress-corrosion cracking (SCC), a phenomenon in which steels become brittle that is often observed when residual stresses exceed 50% of the ultimate stress. One case of brittle tendon failure due to SCC was observed in parking garage slab regions near column locations, where local tendon curvatures were large [Schupack and Suarez (1982)]. However, Li et al. [Li et al. (2011)] have suggested that SCC may not occur in high chloride environments where pitting corrosion is likely. As a result, pitting corrosion is more common than SCC for prestressed structures.

A majority of corrosion incidents occur for unbonded post-tensioned construction, where corrosion protection is provided by grease instead of grout. Some failures

have also been partially attributed to poor grouting procedures [Calvi et al. (2019); Schupack and Suarez (1982)].

2.4 Simplified Analysis Method for Corroded Prestressed Elements

In this section, a simple strain-based approach is presented for the analysis of corroded prestressed concrete elements that are restrained from creep. Creep restraint induces concrete tensile strains, which may hasten concrete cracking and corrosion advancement. Of course, creep may occur freely in simply supported structural elements, but that case is not as critical for ingress of corrosion agents via concrete tensile cracks. The analytical method is presented for concentrically tensioned elements, such as may occur in bridge cable stays or ring beam elements. Flexural effects are easily incorporated by superposition of a linear bending strain profile with the axial strains from prestressing and external loads.

Post-tensioning a non-corroded member A concentrically post-tensioned structure will develop compression stress in the concrete, as well as in any reinforcement that is bonded to the concrete at the time of stressing. This analysis assumes that deformed reinforcement (E_d, A_d) is bonded with concrete (E_c, A_c) before the stressing of tendons (E_p, A_p). The compressive post-tensioning force applied to the PC element depends on the jacking strain in the tendons, ϵ_j, as shown:

$$F_p = E_p A_p \epsilon_j \tag{2.6}$$

Slipback of the anchorage will occur as the concrete deforms to accomodate the tendon stress. The amount of slipback is related to the compressive strain induced in the concrete:

$$\epsilon_{comp} = \frac{-E_s A_s \epsilon_j}{E_c A_c + E_d A_d} \tag{2.7}$$

The effective strain in the tendons after slipback is now calculated.

$$\epsilon_p = \epsilon_j + \epsilon_{comp} \tag{2.8}$$

Similarly, the concrete strain and bonded reinforcement strain after the stressing operation are calculated:

$$\epsilon_c = \epsilon_{c0} + \epsilon_{comp} \tag{2.9}$$

$$\epsilon_d = \epsilon_{d0} + \epsilon_{comp} \tag{2.10}$$

where:

ϵ_{c0}, ϵ_{d0} are concrete and reinforcement strains present before the stressing operation.

After stressing and grouting procedures, all aditional loads are resisted compositely by concrete, deformed bars, and prestressing tendons. The composite structure can be treated as springs in parallel:

$$\epsilon_{ext} = \frac{F_{ext}}{(EA)_c + (EA)_d + (EA)_p} \tag{2.11}$$

Uniform Corrosion and Reduction of Reinforcement Area As discussed in Sec. 2.2.4, corrosion of reinforcement produces three main effects: cover cracking, bond reduction, and reduced reinforcement properties. Of the three effects, only the reduction of reinforcement properties is considered in this simple scheme. Cover cracking can be solved analytically, but is more of a serviceability limit state than a strength limit state. That being said, if corrosion induced cracking reaches the surface and is not addressed, the rate of corrosion ingress may increase, exacerbating other corrosion effects. However, the relationship between crack size and corrosion rate is too sensitive to make such an analysis practical. Additionally, bond reduction is not considered because, for prestressed structures, the tendon anchorage will enforce strain compatibility between tendons and concrete in the absence of bond. It is assumed that the bond reduction of the deformed bars will only negligibly reduce the composite stiffness.

First, the effect of uniform corrosion is considered. Uniform corrosion reduces the cross-sectional area of reinforcement uniformly along the length of reinforcement at a rate that depends on cover depth, concrete quality and ambient temperature. For a given corrosion penetration rate, the residual cross-sectional area of reinforcement, A', can be calculated:

$$A' = A_0(1 - \eta) \tag{2.12}$$

where:

A_0 = original cross-sectional area of reinforcement.

η = fractional reduction of reinforcement cross-section area

Reduction of reinforcement area disrupts equilibrium of the axial-load system. After losing area, the reinforcement will contribute less internal resistance and the composite system will extend until equilibrium is achieved. This extension produces a

tensile strain in all components of the composite force resisting system:

$$\epsilon_\eta = \frac{F_\eta}{E_c A_c + E_p A'_p + E_d A'_d} \tag{2.13}$$

where:

$F_\eta = \eta_p E_p A_{p0} \epsilon_p + \eta_d E_d A_{d0} \epsilon_p$

Creep Restraint Creep is a long term effect by which concrete continues to deform under constant application of loads. The amount of concrete creep deformation depends on both the magnitude of the permanent concrete stress and the creep coefficient. Collins et. al. [Collins and Mitchell (1991)] present an expression for the creep coefficient that captures the effect of concrete strength, volume to surface area ratio, humidity, and time of initial load application:

$$\phi = \phi(t, t_i, \frac{V}{S}, f'c, H_r) \tag{2.14}$$

The effect of creep is to 'soften' the concrete modulus:

$$E_{c_{eff}} = \frac{E_c}{1 + \phi(t, t_i)} \tag{2.15}$$

In the absence of creep restraint, the free concrete creep strain due to a constant load, f_{ci}, applied t_i days after casting is calculated:

$$\epsilon_{free} = \frac{f_{c_i}}{E_{c_{eff}}} \tag{2.16}$$

Typically, concrete elements are isolated while they harden, when the effect of creep (and shrinkage) is largest. Creep of post-tensioned structures will continue to occur after the stressing operation but will be partially restrained by any bonded reinforcement that resists free concrete creep. Once the prestressed element is connected to

the rest of the structure, any additional creep will be restrained. Figure 2.5 shows that creep deformation decreases exponentially with time.

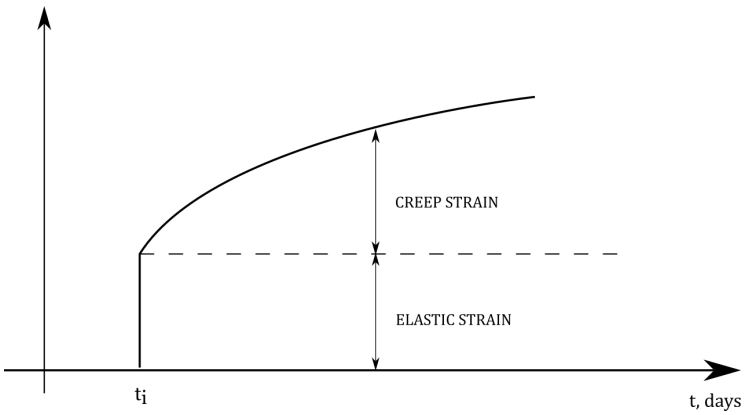

Figure 2.5: Evolution of creep strain with time

After the stressing operation and before connection with the structure, creep of a post-tensioned element will be partially restrained. Figure 2.6 demonstrates the effect of composite behavior on concrete strains during the partial creep restraint phase. Figure 2.6a shows that, based on equilibrium considerations, the composite system strains less than the plain, unrestrained concrete. The difference in these two strains is the tension strain induced in the concrete. Throughout time, the tensile creep restraint and the compressive jacking strain sum, resulting in a reduced permanent stress in the concrete. The permanent, creep inducing, stress, Eq. (2.16), decreases in time, as shown in Fig. 2.6b, where σ_i is the permanent concrete stress at a time increment, t_i.

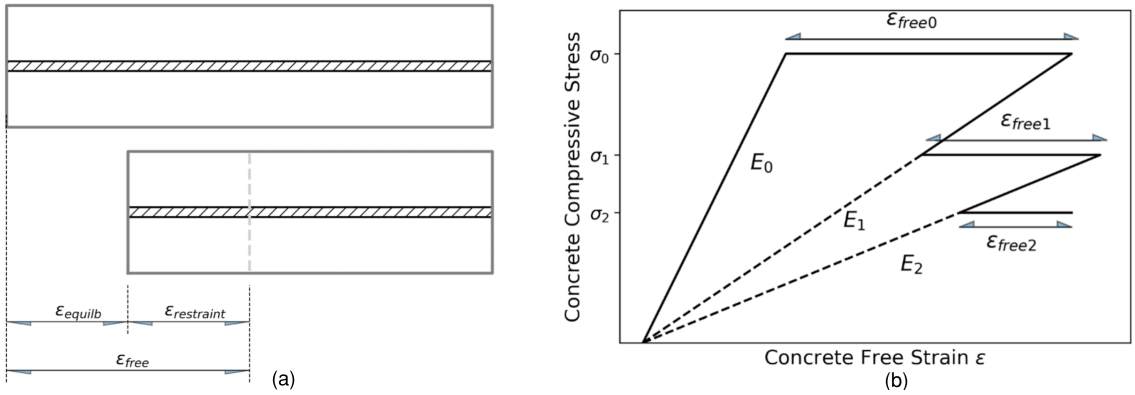

Figure 2.6: (a) Equilibrium creep is less than free creep for a composite member (b) Free creep strains are reduced as the prestressing force from tendons is reduced

The cumulative free creep strain at any time can be derived from Fig. 2.6b if the creep coefficient and free creep strain at a previous time are known.

$$\epsilon_{free_{cum}} = \sum_{n=0}^{i-1} (\epsilon_{free_{i-1}}) + \frac{\sigma_i (E_{i-1} - E)i)}{E_{i-1} E_i} \tag{2.17}$$

Most creep deformation occurs early in the life before the tendon corrosion levels are high, so the restraint calculations are effectively independent from the corrosion rate.

Nonlinear Stress-Strain Responses and Pitting Corrosion In the preceding paragraphs, the simplified method was developed assuming an elastic structural response. This keeps the equations simple and familiar. However, the method must be extended to consider the nonlinear stress-strain curves of concrete and reinforcement. The concrete response accounts for creep softening and the reinforcement responses are modified to capture pitting corrosion effects, from Eqs. (2.3)-(2.5).

Material strains are no longer calculated from Eqs. (2.7),(2.11), and (2.13), which assume linear behavior. Instead, the strains are updated in an iterative numerical

process until equilibrium of external loads and internal forces is achieved. At each converged strain point, material stresses are calculated from the stress-strain curves shown in Fig. 2.7.

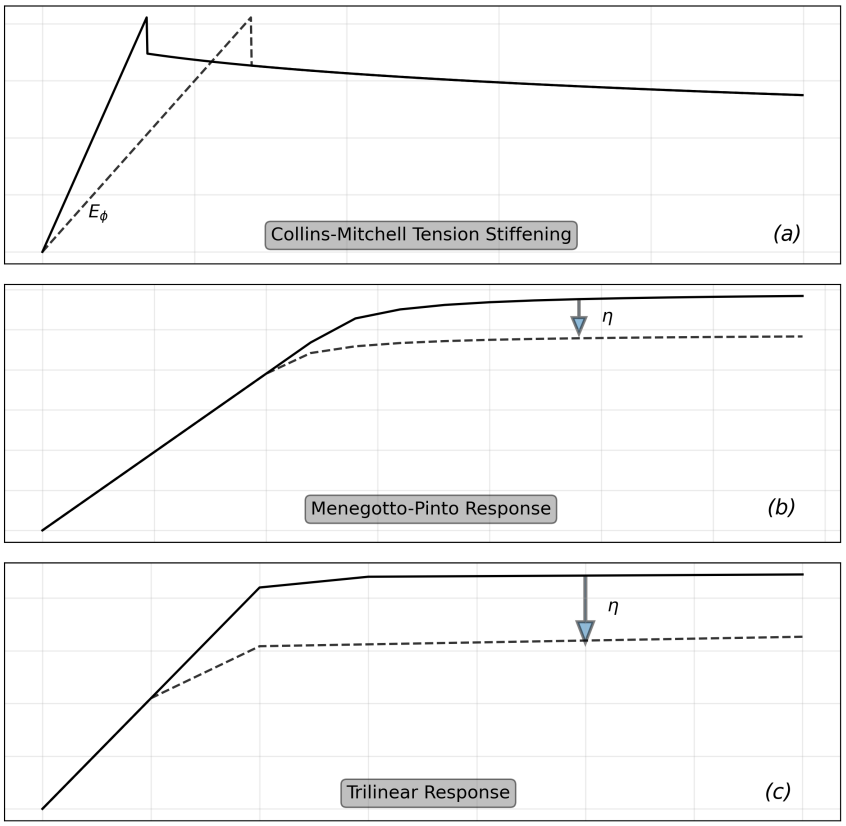

Figure 2.7: Material curves used in analysis method of corroded PC structures

Figure 2.7a shows the tensile stress-strain response of concrete, proposed by Collins Collins and Mitchell (1991). The elastic portion of the curve softens in time (dashed line) to capture the creep effects of Eq. (2.15). Figures 2.7b&c show the stress-strain curves for prestressing reinforcement and deformed bars, which are modified to capture pitting corrosion effects. This is done by decreasing the yield stress, ultimate stress, and yield strain, depending on the average reinforcement corrosion levels, η.

CHAPTER 3

FATIGUE OF REINFORCEMENT

3.1 Review of Fatigue Damage

Fatigue is a structural failure mode of reinforcement in which damage is accumulated via repeated loads. The magnitude of cyclic load to cause failure can be significantly lower than the nominal stress capacity, making fatigue a subtle and often overlooked failure mechanism. The fatigue life of reinforcement is defined as the number of load cycles sustained before failure, which often manifests in brittle fashion. Fatigue life depends on the magnitude of applied stress, reinforcement geometry, and material properties. Broadly, fatigue life is separated into two phases: crack nucleation and crack growth, as shown in Fig. 3.1.

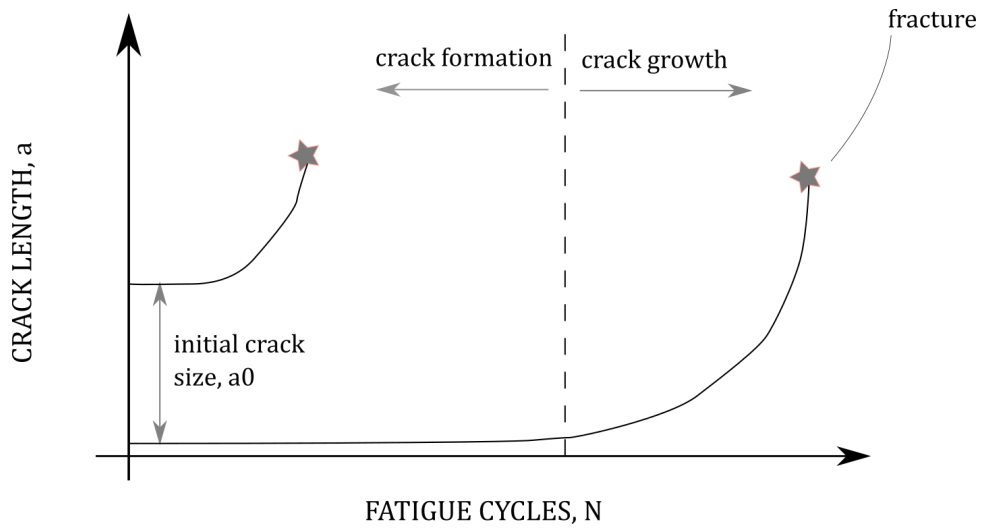

Figure 3.1: Schematic of fatigue crack evolution, with and without initial flaws, adapted from [Grandt (2004)]

For a non-damaged bar (i.e., no initial flaws), the crack nucleation phase contributes a non-negligible portion of the fatigue life. The presence of any surface flaws in the

form of cracks or notches effectively annihilates the fatigue life associated with crack formation. The effect of a surface flaw on fatigue life is shown in Fig. 3.1.

3.1.1 Fatigue Crack Growth

Assuming certain criteria are met (see Sec. 3.2.2), a crack will grow after the nucleation phase, extending with each load cycle at a rate that depends on the following factors:

- Amplitude of cyclic load cycles, $\Delta\sigma$
- Ratio of minimum to maximum cyclic stress amplitude (i.e., load ratio, $R = \frac{\sigma_{min}}{\sigma_{max}}$)
- Load history
- Environmental conditions

A schematic of important fatigue load parameters is shown in Fig. 3.2.

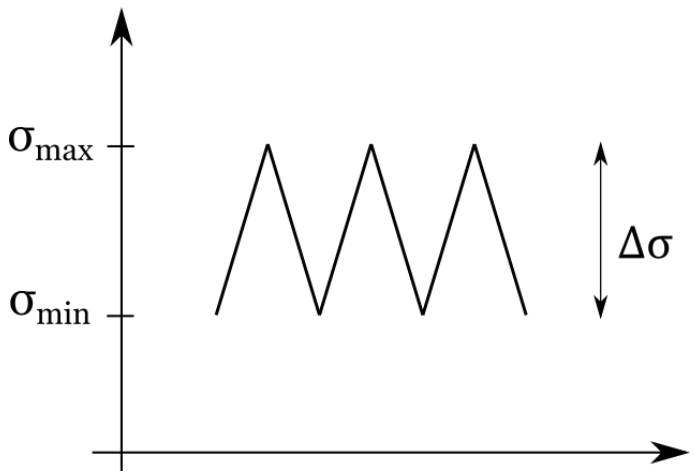

Figure 3.2: Fatigue load parameters that impact crack growth rate, adapted from [Grandt (2004)]

A full characterization of fatigue loading requires specification of at least two of the following parameters: $R, \sigma_{min}, \sigma_{max}, \Delta\sigma$. A common crack growth rate model is presented in Sec. 3.2.2, where more tools are introduced.

The specific load-cycle history has been shown to produce unusual crack growth behavior. For instance, a high-amplitude (overload) cycle amidst regular cyclic loading has been shown to increase fatigue life. This behavior is difficult to predict, as it depends on material yielding at the crack tip and also whether the overload follows a peak or valley of a stress cycle. Such a precise knowledge of loading conditions is unknown for practical structural engineering scenarios. Therefore, overload effects are not directly included in the crack growth models presented in this thesis. The curious reader is directed to Grandt's text [Grandt (2004)] for further reading.

Once a crack has reached a critical size, its growth will no longer remain stable and fatigue fracture will occur suddenly. An example of a fatigue failure surface is shown in Fig. 3.3, where crack striations indicate crack growth.

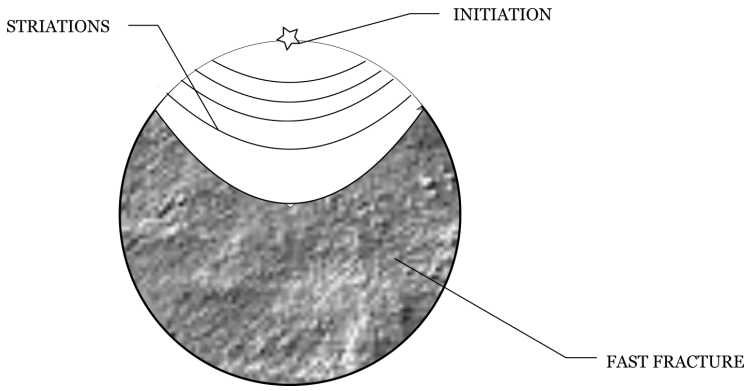

Figure 3.3: Schematic of typical fatigue fracture surface, showing striations and rapid fracture

3.1.2 Corrosion-Fatigue

Corrosion-fatigue is a particularly damaging form of fatigue that occurs in an aggressive environment or when corrosion flaws (e.g., corrosion pits) exist on the reinforcement surface. Speidel [Speidel (1974)] has shown that fatigue cracks grow faster in aggressive environments. Furthermore, the presence of local corrosion defects can act as both a stress concentration and a crack nucleation zone. The effect of an inital defect eliminates the fatigue crack formation phase and the stress concentration increases the mean stress at the flaw. Both effects can substantially reduce fatigue life.

3.2 Traditional Fatigue Analysis

3.2.1 S-N Analysis

The fatigue life of steel reinforcement is commonly evaluated using a stress-life (S-N) approach. The simplicity of the the S-N approach makes it an attractive tool to quickly estimate the number of fatigue cycles required to fail a specimen; the number of load cycles, N, before fatigue failure at a given alternating stress range, S, can be determined from experimental data for a specific material, crack orientation, and environment. S-N analysis does not distinguish between the crack formation phase and the crack growth phase. Various stress ranges are plotted against the corresponding number of cycles to failure to build a curve that can be easily used for design or analysis. A schematic of an S-N diagram is shown in Fig. 3.4, emphasizing the empirical nature of S-N curve fits. The figure shows that, for some metals, there appears to exist a stress range below which failure is not observed, no matter the number of applied load cycles. This stress range is called the infinite life threshold.

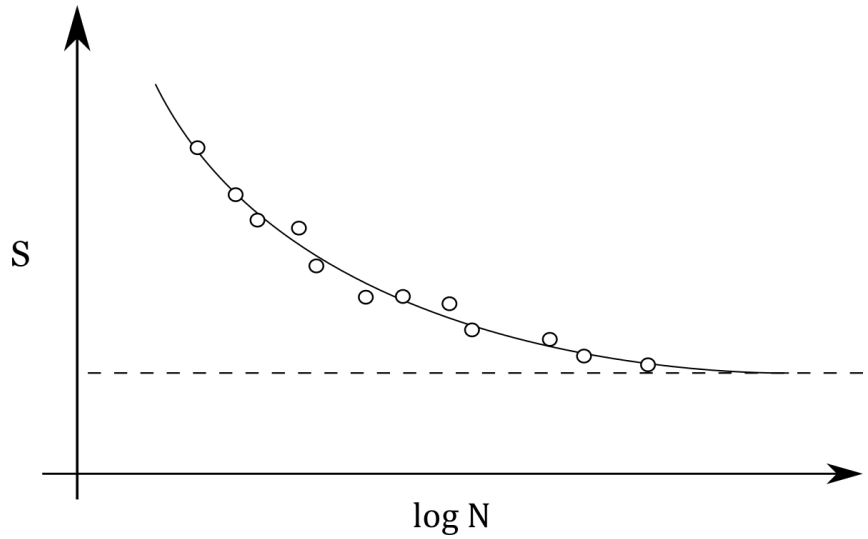

Figure 3.4: Schematic of S-N curve, showing the experimental nature of fatigue-life curves

Figure 3.4 shows that if a constant cyclic stress amplitude is known, the number of cycles to reinforcement failure can be easily determined from an S-N curve, specific to the material and geometry. However, in structural engineering applications, the amplitude of fatigue loads is often variable. The Palmgreen-Miner rule allows constant-amplitude S-N curves to be extended for variable-amplitude loading.

Palmgreen-Miner Rule In the Palmgreen-Miner rule, variable-amplitude cyclic loads are approximated as a series of constant-amplitude load blocks. Each load block contributes a percentage of damage to the specimen, which fails when the cumulative damage reaches unity. The damage, D, is defined by Eq. (3.1), where n_i is the number of load cycles in each block and N_i is the number of life cycles on the S-N curve corresponding to the i-th load block amplitude.

$$D = \sum \frac{n_i}{N_i} \leq 1 \tag{3.1}$$

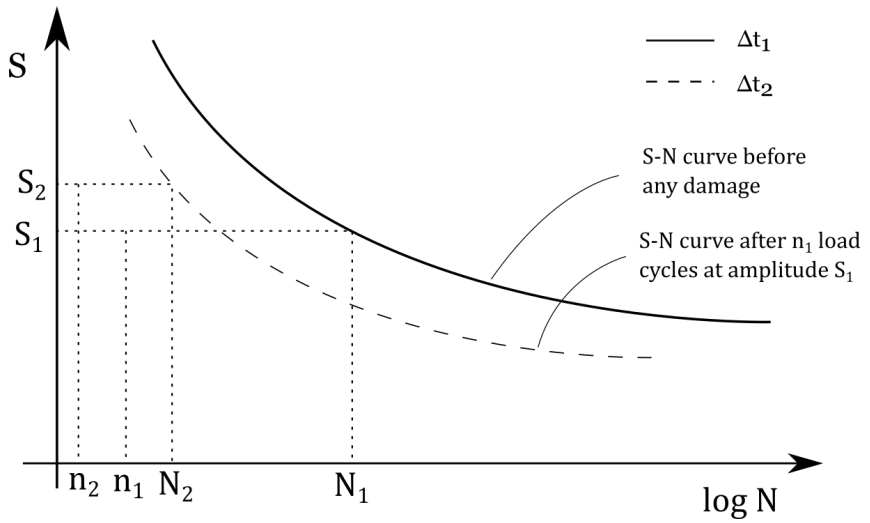

Figure 3.5: Palmgreen-Miner rule for damage accumulation, adapted from Morgese [Morgese et al. (2019)]

The Palmgreen-Miner rule assumes a linear damage accumulation where each load cycle is assumed to contribute the same damage. Though some researchers [Lee et al. (2005); Isojeh et al. (2019)] have proposed nonlinear damage accumulation rules, the Palmgreen-Miner rule is used throughout this work due to its simplicity.

3.2.2 Linear Elastic Fracture Mechanics (LEFM)

Linear elastic fracture mechanics (LEFM) describes the mechanics of crack growth, from initial flaw to fracture. The method can only predict the number of crack growth cycles before failure because it assumes the presence of an initial flaw. As a perfect specimen rarely exists, the LEFM method is extremely useful for the practical scenario in which a material has an initial flaw.

Early fatigue experiments [Paris and Erdogan (1963)] showed that crack growth is related to an elastic parameter that relates remote load, specimen geometry, and

crack size. This parameter, the stress intensity factor (K), generally takes the following form:

$$K = \sigma\sqrt{\pi a}\beta \tag{3.2}$$

where:

σ = remote stress applied to the specimen

a = crack size

β = geometry factor

The geometry factor, β, is determined from elasticity solutions for specific specimen and crack geometries. The solution for a solid bar subject to a uniform tension field with a semi-elliptical crack is given by Forman [Forman and Shivakumar (1986)]:

$$\beta = G[0.752 + 1.286F + 0.37Y^3] \tag{3.3}$$

where:

$G = 0.92\left(\frac{2}{\pi}\right)\sec F\left(\frac{\tan F}{F}\right)^{1/2}$

$F = \left(\frac{\pi}{2}\right)\left(\frac{a}{D}\right)$

$Y = 1 - \sin\beta$

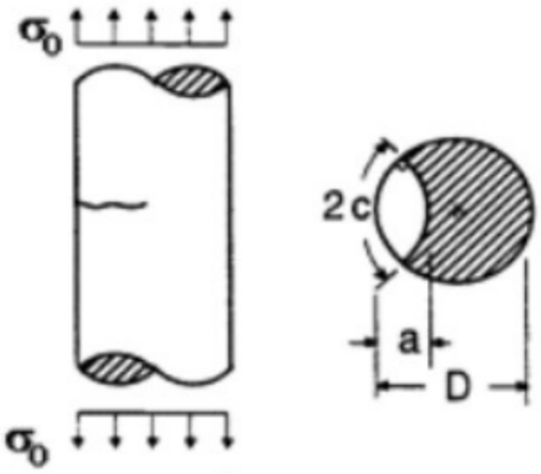

Figure 3.6: Semi-elliptical flaw with uniaxial tensile loading

The crack growth rate is plotted against the stress intensity factor range, ΔK, which describes the change in stress intensity due to cyclic loads:

$$\Delta K = \Delta\sigma\sqrt{\pi a}\beta \tag{3.4}$$

where:

$$\Delta\sigma = \sigma_{max} - \sigma_{min}$$

A schematic of a typical crack growth rate curve is shown in Fig. 3.7. The figure identifies three ranges of crack growth behavior. In the first range, fatigue cracks do not grow if a threshold value of ΔK is not exceeded. In the second range, the crack growth rate is log-log linear with ΔK. This linear relationship was first proposed by Paris [Paris and Erdogan (1963)], and is shown in Eq. (3.5). In the third range, the specimen will fail when the stress intensity factor exceeds the material's fracture toughness, K_c.

$$\frac{da}{dN} = C(\Delta K)^m \tag{3.5}$$

where:

C, m = experimentally calibrated parameters for specific material, specimen geometry and crack geometry

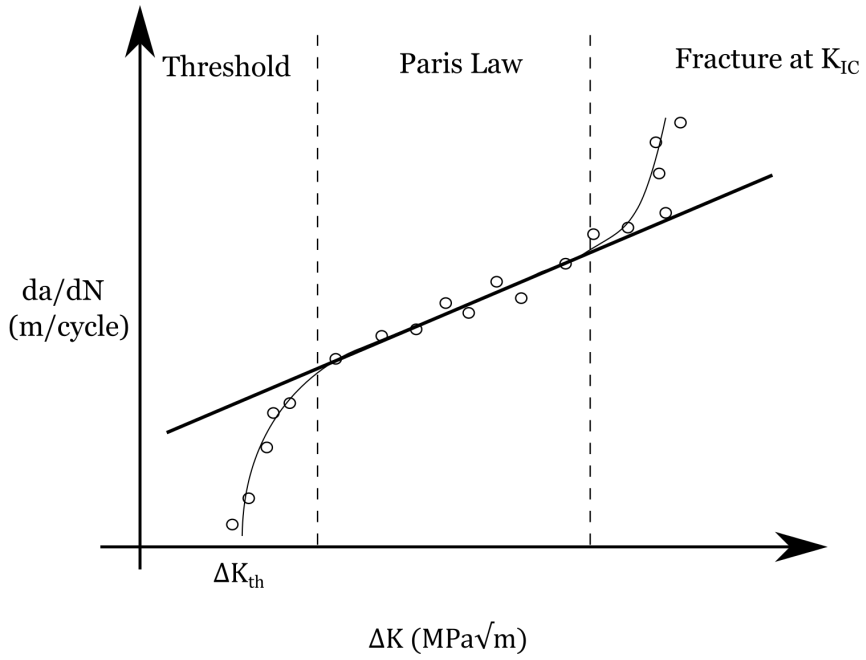

Figure 3.7: Crack growth rate for various stress intensity factor ranges

3.3 Simple Corrosion-Fatigue Analysis Schemes

This section extends the traditional S-N and LEFM analysis methods to incorporate corrosion. This extension is achieved with the help of experimental models developed by other researchers [Jiang et al. (2018); Sun et al. (2019)].

3.3.1 S-N-η Failure Surface

First, the S-N method is extended to include corrosion, based on experimental fatigue failure results for corroded bridge wires from Jiang [Jiang et al. (2018)]. Jiang's experiment suggests a failure surface that relates alternating stress amplitude, S,

corrosion level, η, and cycles to failure, N. The surface is described by Eqs. 3.6-3.7:

$$log_{10}N + (3.154 - 2.73\eta)log_{10}S = 13.929 - 11.09\eta.....S > 360MPa \tag{3.6}$$

$$log_{10}N + (19.2461 - 96.19\eta)log_{10}S = 55.174 - 250.67\eta...S < 360MPa \tag{3.7}$$

In Jiang's expression, fatigue life cycles, N, can be obtained if alternating stresses, S, and corrosion levels, η, are known. As for traditional S-N analysis, variable amplitude loading is captured by the Palmgreen-Miner rule, Eq. (3.1). A cross-sectional slice of Jiang's S-N-η surface at a given η_i level produces an $S_i - N_i$ life curve, where N_i is inserted into Eq. (3.1) to calculate damage accumulation.

A shortcoming of this approach is that the experimental fatigue-life prediction curve is extrapolated from limited test data and only makes sense for corrosion levels below 20%. Next, a fracture mechanics approach is presented that does not have this limitation.

3.3.2 Fatigue Crack Approach

Recall that the LEFM approach assumes the presence of an initial flaw. Experiments were performed by Sun et al. [Sun et al. (2019)] for corroded reinforcement to determine an Equivalent Initial Flaw Size (EIFS) based on the uniform corrosion level from the experiments. This experimental data is not restricted to a low range of corrosion values as was the case for the experimental S-N-η surface.

$$a_{EIFS} = 0.00372\eta^2 + 0.0565\eta - 0.0116 \tag{3.8}$$

where:

a_{EIFS} = initial flaw size, calibrated from fatigue tests on corroded reinforcement

The EIFS can be thought of as the statistical cavity (i.e., pitting corrosion) that would need to exist for correct calibration of the fatigue life test data of a corroded specimen using the LEFM concepts outlined in the preceding paragraphs for the assumed crack geometry. Once the EIFS is known, the stress intensity factor is calculated according to the expression in Eq. (3.2). As loads evolve, the crack size is updated from an experimentally determined, material specific crack growth law. Jiang et al. [Jiang et al. (2018)] has experimentally determined the crack growth rate law for corroded high-strength wires, a reproduction of which is shown in Fig. 3.8. The figure plots the crack growth rate against the stress intensity range, ΔK. Jiang reports a stress-intensity threshold, K_{th}, of 3.2 $MPa\ m^{1/2}$ and a fracture toughness of 65.7 $MPa\ m^{1/2}$.

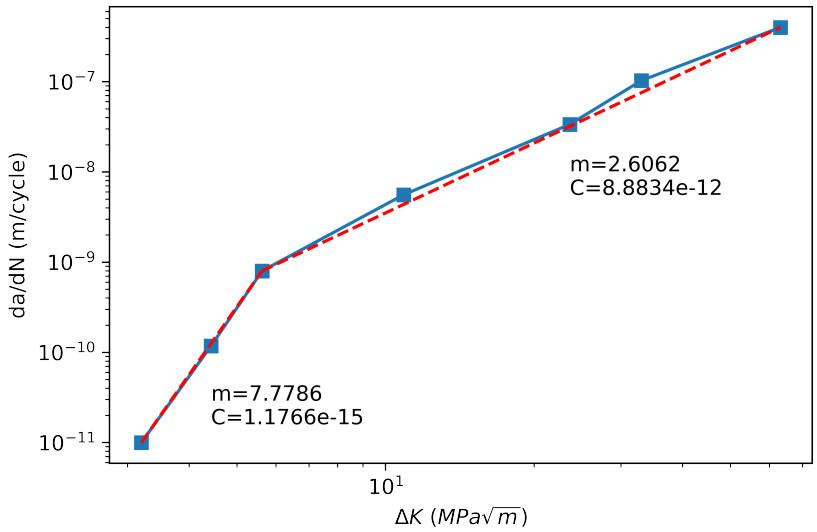

Figure 3.8: Segmental Paris Law parameters from Jiang's experimental crack growth experiment, that relate the crack growth rate, da/dN, to the stress intensity range, ΔK

Jiang's results are nearly log-log bilinear, so a segmental Paris Law for fatigue crack growth, Eq. (3.9), is used to update the crack sizes, where the Paris power law parameters are shown in Fig. 3.8. For any time, t_i, the crack growth rate, $(\frac{da}{dN})_i$ is determined from the stress intensity range, ΔK_i.

$$\left(\frac{da}{dN}\right)_i = C(\Delta K_i)^m \tag{3.9}$$

For any time increment, Δt_i, if the rate of corrosion pit growth exceeds the rate of crack growth from Eq. (3.9), the statistically calculated cavity's growth annihilates any fatigue crack growth. Thus, the crack growth is taken as the larger of $\frac{da_{EIFS}}{dN}$ and $\left(\frac{da}{dN}\right)_i$.

CHAPTER 4

TORSION OF BEAM MEMBERS

Torsional is commonly avoided in design; however, the effects of torsion cannot always be neglected. For instance, torsion may govern the behavior of eccentrically-loaded or curved members.

Current torsion design methods belong to the family of skew-bending theories. These models only consider equilibrium conditions at the beam's cracked state. Equilibrium is written from an assumed cracked configuration in which both longitudinal and transverse reinforcement have yielded. Based on experimental testing, the cracked configuration is commonly assumed to form a skewed surface in which a diagonal compression hinge forms on one beam face and tension cracks form on the other three faces. Different failure surfaces may exist depending on the distribution of reinforcement and the ratio of applied torsion, moment, and shear, as shown in Fig. 4.1.

Skew-bending theories are used in design due to their simplicity. The equilibrium conditions are easily adapted into interaction diagrams between applied bending moments, shear, and torsion moments. Despite these advantages, the skew-bending models are somewhat limited by the assumption of a kinematic yield condition. As such, the models fail to predict reinforcement and concrete strains. Without a rational strain compatibility equation, the models cannot predict deformations, nor can they rationally verify the assumed failure modes.

Deflections may be of importance in the analysis of aging structures, so a tool is needed that captures the full load-deformation response of members subject to combined loads. Full 3-D finite element analysis is commonly performed by analysts,

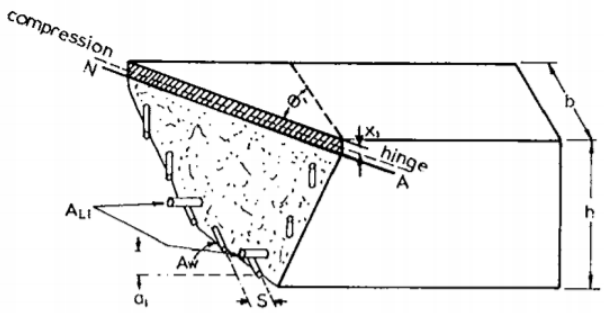

FIG. 14-4 FAILURE SURFACE MODE 1

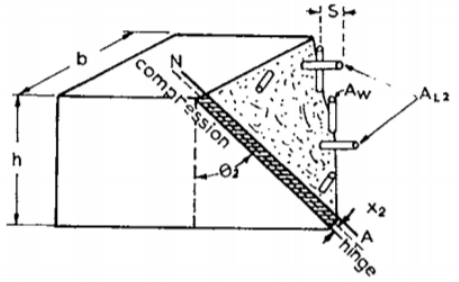

FIG. 14-5 FAILURE SURFACE MODE 2

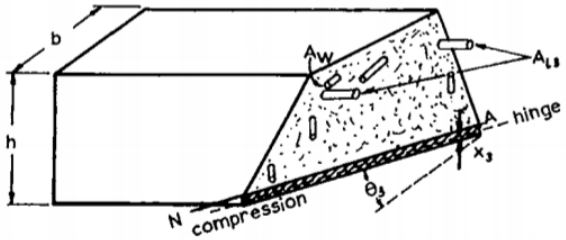

FIG. 14-6 FAILURE SURFACE MODE 3

Figure 4.1: Torsional failure modes observed during experimental testing, from [Collins et al. (1968)]

but advanced FEM software can be difficult to implement correctly. The gap between skew-bending models and 3D-FEM is filled by truss models, which can predict forces and deformations by combining a rational strain-compatibility condition with equilibrium expressions and constituitive laws. The remainder of this chapter builds the truss-model theory from the ground up, starting with elastic torsion theory.

4.1 Elastic Torsion Theory

This section introduces the basic torsion relationships and provides common analogies for visualizing torsion. The theory will then be extended to describe the elastic

load-deformation response for thin tubes, as well as multi-cell boxes.

4.1.1 Torsion of Circular Sections

The torsion response of circular shafts was first described by Navier, who assumed the following:

- plane sections remain plane during torsional deformation
- the cross-section does not change shape during torsional deformation

Navier showed that the shear strain of a differential element within a circular cross-section is proportional to the distance, r, from the longitudinal twist axis and the twist rate, ϕ, which describes the change in rotation angle per unit length.

$$\gamma = r\frac{d\theta}{dz} = r\phi \tag{4.1}$$

Equation (4.1) is combined with the shear constituitive relationship, which results in Eq. (4.2).

$$\tau = G\gamma = rG\phi \tag{4.2}$$

Equation (4.3) gives the elastic load-deformation equation for circular shafts, which follows from integration of shear stresses over the cross-sectional area.

$$T = GI_p\phi \tag{4.3}$$

where I_p is the polar moment of inertia.

4.1.2 St. Venant Torsion for Non-Circular Sections

Torsional deformation of non-circular sections is not free from warping deformation, as was the case for Navier torsion. St. Venant's torsion theory uses the following assumptions, which differ from those of Navier to reflect the warping condition:

- Warping of non-circular sections is constant along the member length.
- The cross-section being considered is far from the supports, where warping deformation would be restrained.
- The cross-section retains its shape throughout torsional deformation.

St. Venant continues to use Navier's second assumption, which is unaffected by the warping condition.

Semi-Inverse Solution Method In St. Venant's solution method, a form is assumed for the displacements but the warping displacement is left undetermined. Then, strains and stresses are obtained via elasticity relationships. An equilibrium expression is found from the stress expressions and boundary conditions are applied to determine the warping function, $\Psi(x, y)$.

Displacements take the following form, provided that the cross-section retains its shape throughout deformation and the twist rate is constant.

$$u = -yz\phi \tag{4.4}$$

$$v = xz\phi \tag{4.5}$$

$$w = \Psi(x, y)\phi \tag{4.6}$$

where:

ϕ is the angle of twist per unit length

Ψ is the warping function, and

u, v, and w are displacements in the x, y, and z directions, respectively.

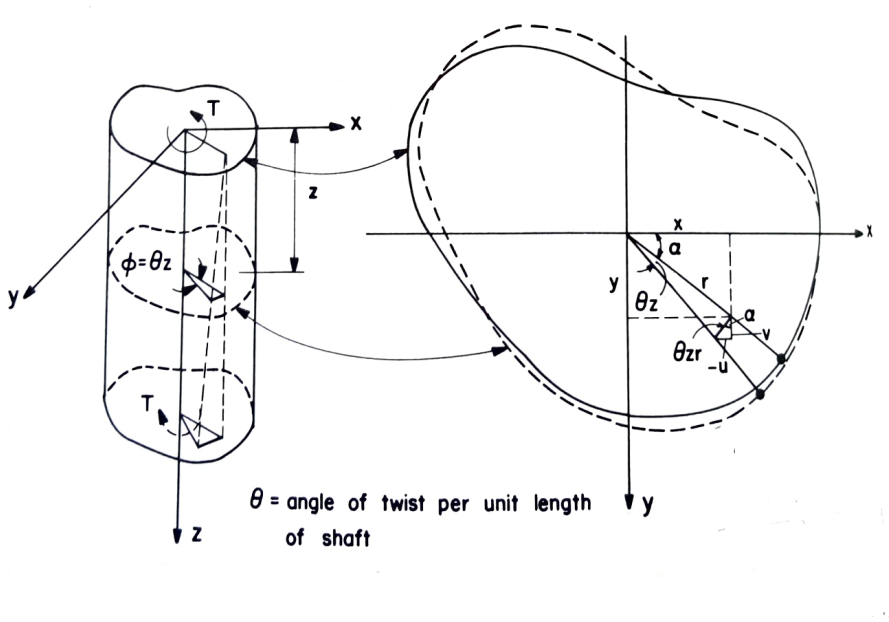

Figure 4.2: Torsional deformation, from [Hsu (1984)]

Element strains are obtained from the definition of the small-strain tensor, which involves gradients of the displacement vector, $\boldsymbol{u}$.

$$\boldsymbol{\epsilon} = \frac{1}{2}(\nabla \boldsymbol{u} + \nabla \boldsymbol{u}^T) = \frac{1}{2}\begin{bmatrix} 0 & 0 & \phi(\frac{\partial \Psi}{\partial x} - y) \\ 0 & 0 & \phi(\frac{\partial \Psi}{\partial y} + x) \\ \phi(\frac{\partial \Psi}{\partial x} - y) & \phi(\frac{\partial \Psi}{\partial y} + x) & 0 \end{bmatrix} \tag{4.7}$$

Element stresses are obtained from the constituitive law for an isotropic material:

$$\boldsymbol{\sigma} = 2G\boldsymbol{\epsilon} + \lambda tr(\boldsymbol{\epsilon})\mathbf{1} = G\begin{bmatrix} 0 & 0 & \phi(\frac{\partial \Psi}{\partial x} - y) \\ 0 & 0 & \phi(\frac{\partial \Psi}{\partial y} + x) \\ \phi(\frac{\partial \Psi}{\partial x} - y) & \phi(\frac{\partial \Psi}{\partial y} + x) & 0 \end{bmatrix} \tag{4.8}$$

Equation (4.8) demonstrates that only the shear stresses with a component in the longitudinal direction survive for a state of pure torsion. Shear stresses in the plane of the cross-section would deform the section, thus invalidating St. Venant's third assumption that the cross-section retains its shape during twisting.

In the absence of body forces, equilibrium is expressed as follows:

$$\nabla \cdot \boldsymbol{\sigma} = \mathbf{0} \tag{4.9}$$

Inserting the St. Venant torsional stresses from Eq. (4.8) into Eq. (4.9) results in a partial differential equation:

$$\frac{\partial \tau_{xz}}{\partial x} + \frac{\partial \tau_{yz}}{\partial y} = 0 \tag{4.10}$$

The Prandtl stress function, Φ, is introduced to facilitate the solution of the shear stresses at the boundaries of the problem domain. Φ is defined such that $\Phi_{,y} = \tau_{xz}$ and $\Phi_{,x} = -\tau_{yz}$. Substitution of the Prandtl stress function into Eq. (4.10) gives the equilibrium expression in the form of Laplace's equation.

$$\frac{\partial^2 \Phi}{\partial x^2} + \frac{\partial^2 \Phi}{\partial y^2} = \nabla^2 \Phi = -2G\phi \tag{4.11}$$

At traction free boundary surfaces, Eq. (4.11) results in $\frac{\partial \Phi}{\partial s} = 0$. For simplicity, Φ is often set to zero along the boundaries. The torsional resistance of the section is solved by integrating shear stresses on the longitudinal face and applying the divergence theorem:

$$T = 2 \int_A \Phi \, dA \tag{4.12}$$

The torsional stiffness that relates the applied torque with the rate of twist-deformation is shown in Eq. (4.13).

$$GJ = \frac{2}{\phi} \int_A \Phi \, dA \tag{4.13}$$

Membrane Analogy Visualization of the torsion problem is aided by the similarities with the 'membrane' problem, which describes the deflection, w, of a thin membrane subject to a uniform distributed load, q. Both the torsion problem and the membrane problem take the form of Laplace's equation.

Table 4.1: Analogy between torsion problem and membrane problem

TORSION	MEMBRANE
$\nabla^2\Phi = -2G\phi$	$\nabla^2 w = -\frac{q}{s}$
$\tau = \frac{\partial\Phi}{\partial n}$	slope$= \frac{\partial w}{\partial n}$
$\Phi = 0$ along boundary	$w = 0$ along boundary
$T = 2\int \Phi \, dA$	Volume$= \int w \, dA$

4.1.3 Thin Tube Theory

Approximate expressions for the torsional strength of thin-walled tubular members were developed by Bredt [Bredt (1896)], who utilized the same assumptions as St. Venant. For thin-walled sections, it is reasonably assumed that the shear flow, q, is constant around the perimeter, where shear flow is defined the product of shear stress and wall thickness, h:

$$q = \tau h \tag{4.14}$$

The circulatory shear stress that develops in the walls must equilibrate the externally applied torque. Equilibrium via integration of shear stresses shows that the torsional resistance of a section is proportional to the shear flow and the area, A_0, enclosed by the centerline of the tube's walls.

$$T = GJ\phi = q \oint r ds = 2\tau h A_0 \tag{4.15}$$

Compatibility requires that the line integral of warping around the perimeter of a cross-section must equal zero. The warping displacement for any differential element can be written as the sum of a twist deformation and a shear deformation. This compatibility relates shear strains and the torsional twist-rate as follows (see Appendix A):

$$\oint \gamma ds = 2\phi A_0 \tag{4.16}$$

Combining Eqs. (4.2), (4.15), and (4.16) leads to the following approximate expression for the torsion constant of a thin-walled tube with varying wall thickness, h.

$$J = \frac{4A_0^2}{\int \frac{ds}{h}} \tag{4.17}$$

For a single cell, the approximate thin-tube theory is compared to the exact St. Venant solution, in which Laplace's equation, Eq. (4.11), is solved for Φ and then J is determined from Eq. (4.13). Solution of Laplace's equation for a box-cell requires a boundary condition for both the outer and inner surface. The outer boundary condition is satisfied by $\Phi = 0$, which satisfies the global equilibrium condition that $\frac{\partial \phi}{\partial s} = 0$. The inner boundary can be solved (Appendix A) by applying the principle of minimum potential energy at the inner boundary surface, which enforces equilibrium locally, for a square cell with constant wall thickness:

$$\Phi_{inner} = \frac{(a-h)h}{2} G\phi \tag{4.18}$$

where:

a is the outer dimension of a square cell,

h is the constant wall thickness

ϕ is the twist rate per unit length of the member

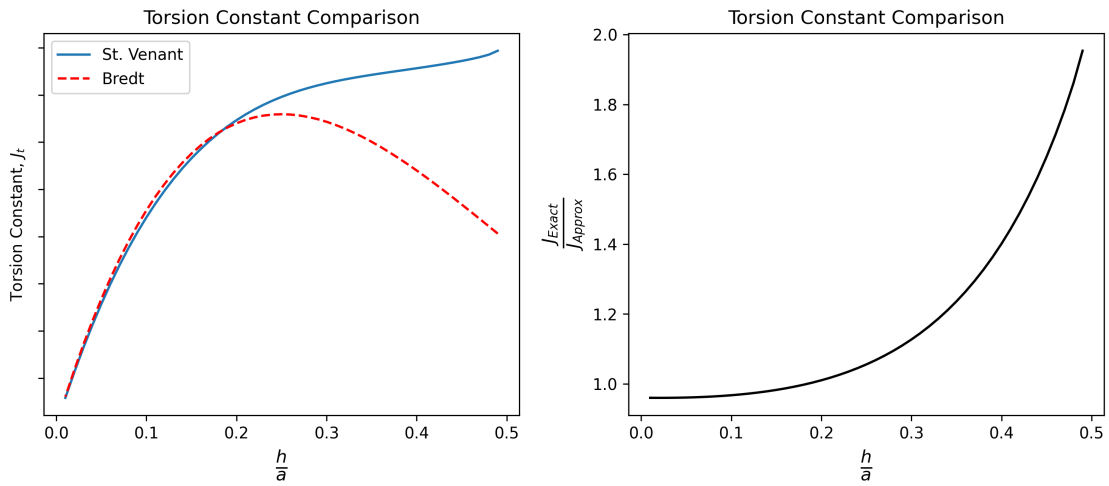

Figure 4.3: Comparison of torsion constant for approximate thin-tube theory with exact St. Venant solution

Comparison of Bredt's approximate theory with the exact solutions in Figure 4.3 shows that the approximate theory is accurate for wall thicknesses that do not exceed 15% of the cell's outermost dimension.

4.1.4 Torsion of Multiple-Cell Boxes

Often, bridge decks consist of multiple cells that twist together to resist torsional loads. The approximate thin tube theory (Section 4.1.3) for predicting strength and stiffness of a single cell can be adapted for multi-cell sections. Here, a classic relaxation approach [Benscoter (1946)] is reviewed, though a matrix approach may be more handy for computer processing in which n equations are solved simultaneously for an n-cell girder.

In the relaxation approach, a multi-cell box is initially treated as a collection of independent cells, each governed by Eqs. (4.14)–(4.17). All cells are assigned a unit

twist ($G\phi = 1$), resulting in a constant shear flow for each cell:

$$q_i = \frac{2A_{0i}}{\oint \left(\frac{ds}{t}\right)_i} \tag{4.19}$$

Once the shear flow in each isolated cell has been determined, adjacent cells are linked by summing their individual shear-flow contributions at the interior webs. This action completes the multi-cell assembly; however, simply adding the individual shear flow contributions does not produce shear flows that satisfy the twist compatibility requirement. Twist compatibility requires that all cells experience identical twist rates, where the twist rate is solve by rearranging Eq. (4.15).

$$G\phi_i = \frac{1}{2A_i} \oint \frac{q}{h} ds \tag{4.20}$$

To satisfy the compatibility requirement, shear flows are distributed between cells in an iterative process until all cells experience the same (typically unit) twist-rate. Once the shear-flow distribution is complete, the total cross-section torque can be determined:

$$T = \sum 2A_i q_i \tag{4.21}$$

To determine the shear flows for a different applied torsion, one can simply scale the shear flows by the ratio of applied torsion to unit twist torsion. The torsion constant is obtained as $J = \frac{T}{G\phi}$.

4.2 Torsion of Plain Concrete

The elastic theory developed in Section 4.1 under-predicts the cracking strength of plain concrete sections by approximately 50%, based on experimental testing [Hsu (1984)]. Plasticity based models may provide a better estimate of the cracking strength of plain concrete sections; however, given that concrete shear failure

initiates from principal tension stresses and since concrete does not exhibit tensile plasticity, the plasticity solution is unsatisfying.

Hsu's Skew Bending Theory Hsu [Hsu (1984)] developed a skew bending theory in response to the inadequacies of the elastic and plastic theories for torsional strength of plain concrete members. Hsu's skew-bending theory is one of a broader class of skew-bending models that predict failure loads from an assumed failure configuration. To develop his theory, Hsu captured the torsional failure mechanism of plain concrete members with a high-speed camera. The failure sequence is depicted in Fig. 4.4. The camera first detected a 45° inclined crack on the front face of the beam. The initial crack proceeded to widen and extend to the top and bottom faces before the concrete on the back face of the beam crushed. The failure seemed to exhibit bending failure characteristics, with tension cracks on one side of the beam and compression crushing on the other side of the beam. The applied torque can

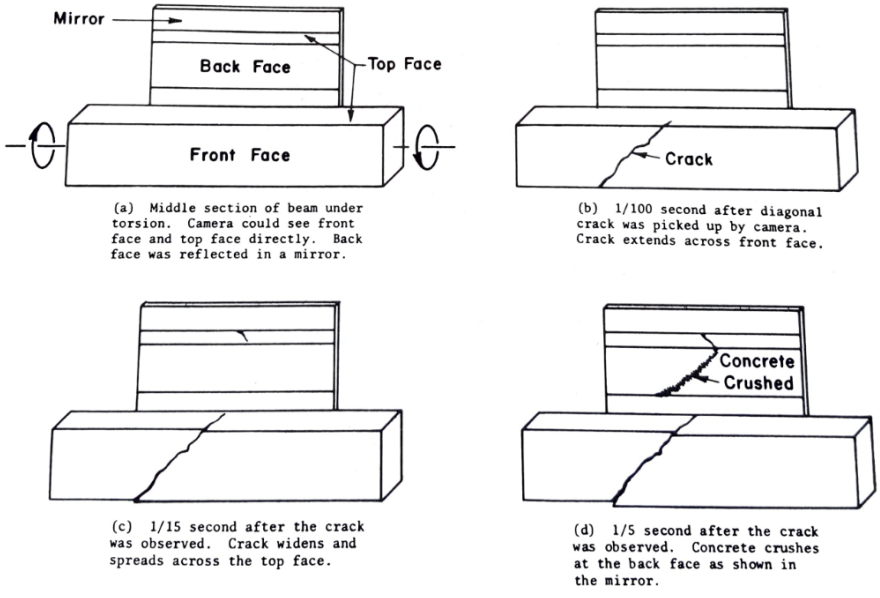

Figure 4.4: Progression of bending type failure mode captured by high speed cameras during torsion of plain concrete specimens, from [Hsu (1984)]

be written in components that are perpindicular and parallel to the failure surface, which is inclined at an angle, θ. The torque component parallel to the failure plane produces a bending moment about the skewed failure surface. Assuming a bending-type failure mechanism, the nominal strength can be predicted by the flexure formula, resulting in the torsional strength of plain concrete members as follows:

$$T_{np} = f_r \frac{x^2 y}{3} \csc 2\theta \tag{4.22}$$

where:

f_r = modulus of rupture

Though plain concrete is uncommon, Hsu's skew-bending theory provides insight into the torsional failure mechanism of concrete. Design codes for shear and torsion typically assign a portion of a member's resistance to a 'concrete contribution', which is often related to the plain concrete strength. Additionally, plain concrete failure modes inform the placement of reinforcement elements in the truss models for torsional strength of reinforced concrete members that are reviewed in Section 4.3.

4.3 Torsion of Reinforced and Prestressed Concrete

Plain concrete in torsion exhibits brittle failure shortly after the formation of diagonal shear cracks. Ductile behavior requires torsional reinforcement. A minimum reinforcement level is required to ensure that the steel can withstand the stress redistribution upon formation of concrete diagonal cracks. A maximum reinforcement level ensures that the reinforcement will yield before the concrete crushes. It should be noted that both longitudinal steel and stirrups resist torsional loads. Throughout the remainder of this work the term 'torsional reinforcement' is used in reference to

both transverse and longitudinal steel. The bending type failure observed by Hsu for plain concrete demonstrates clearly why longitudinal reinforcement is needed to resist torsional loads.

4.3.1 Torsional Strength

Rausch's Space Truss Analogy Rausch developed a space truss analogy to describe the mechanisms of torsion transfer in concrete members. The space truss analogy assumes the concrete core does not contribute to the torsional capacity of the section and it assumes an equal volume ratio between longitudinal steel and stirrups. The equal volume ratio is required for simultaneous yield of all torsional reinforcement. Concrete is represented by diagonal struts between helical cracks that are assumed to have cracked at a 45 degree inclination angle. Steel stirrups and longitudinal ties connect the concrete struts at pinned joint connections. All truss elements are located such that the torsional lever arm coincides with the stirrup centerline from the actual beam, enclosing an area, A_0. Concrete shear resistance and reinforcement dowel resistance are neglected.

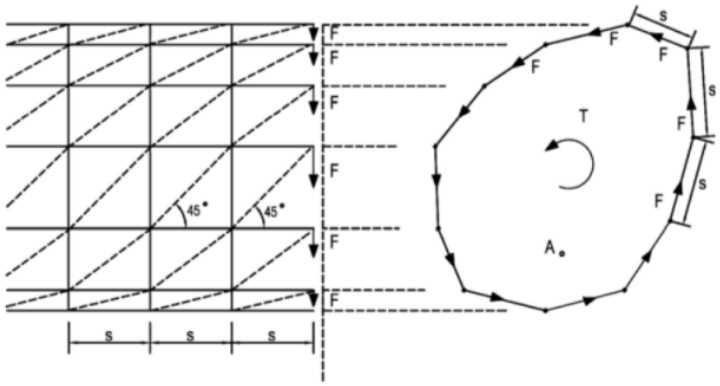

Figure 4.5: Schematic of Rausch space truss concept, from [Hsu (1984)]

Equilibrium of joint forces results in $X = Y = F = \frac{D}{\sqrt{2}}$, where X is the force in a longitudinal tie element, Y is the force in a transverse element, D is the force in a diagonal concrete strut, and F is the shear force at a joint. Global equilibrium requires the shear forces, F, to balance the external torque, T.

$$T_n = \frac{2A_0F}{s} \tag{4.23}$$

Substituting $F = Y = A_t f_{sy}$ gives Rausch's expression for the torsional strength of a reinforced section with equal volume ratios of longitudinal and transverse steel:

$$T_n = \frac{2A_0A_t f_{sy}}{s} \tag{4.24}$$

Rausch's torsion strength result depends on section geometry and reinforcement levels. Note the similarity between Rausch's result and the thin-tube result in Eq. (4.15); Rausch's $\frac{A_t f_{sy}}{s}$ term is analagous to the shear flow in a thin-walled tube. A comparison between Rausch's prediction and experimental results is shown in Fig. 4.6. The figure plots the torsional capacity of a section against the reinforcement factor, $\frac{A_t A_0 f_{sy}}{s}$.

Figure 4.6 indicates that Rausch's linear factor relating a section's torque resistance and reinforcement factor is higher than experimental observations. However, the scale factor of 2 derived by Rausch and Bredt occurs naturally from the line integral in Eq. (4.15). So, Rausch's error must lie elsewhere. Assuming Rausch's functional form is correct, Rausch's assumed area enclosed by the space truss, A_0, must contain error. The error results from the assumption that the space truss exists at the centerline of the stirrup reinforcement. Rausch essentially idealizes the rectangular beam as a thin-tube (hence the agreement with Bredt's theory), but fails to consider the effect of effective wall thickness values on the torsional capacity. This will be discussed more deeply in Section 4.5.

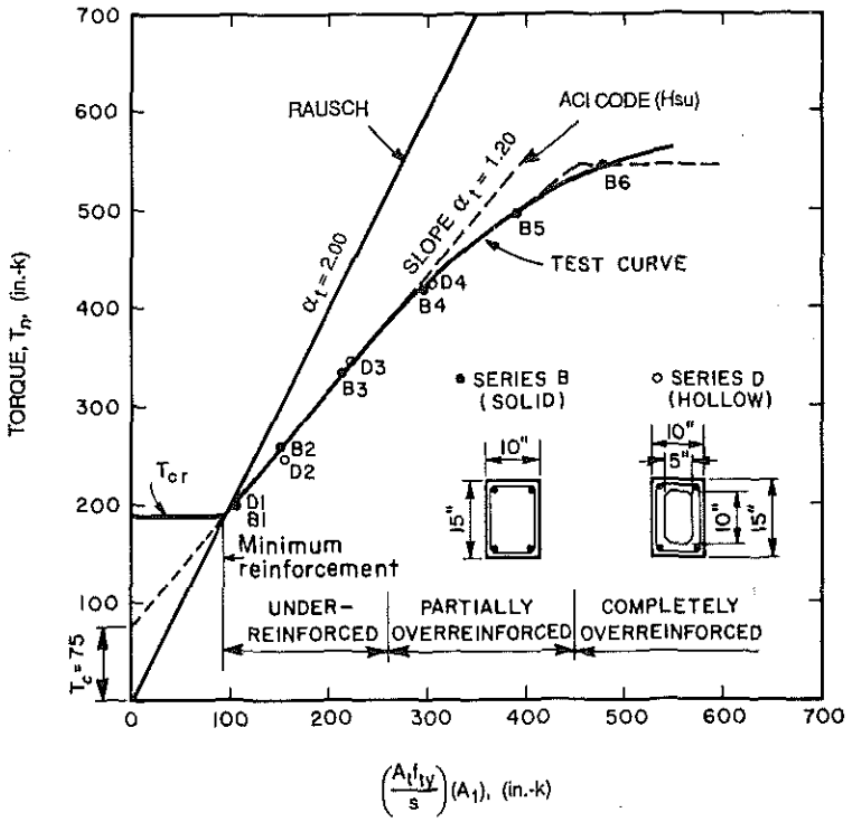

Figure 4.6: Comparison between Rausch's torsional strength prediction and experimental results, from [Hsu (1990)]

Figure 4.6 also shows that the truss model is very conservative for lightly reinforced sections. Rausch's longitudinal and transverse reinforcement elements are required to balance the outward thrust forces from the compressed concrete struts. Without the reinforcement elements, the truss model predicts zero torsional strength. This stands against observations of plain concrete exhibiting some torsional resistance—see Eq. (4.22). Rausch's equation was later modified by Cowan to include a concrete contribution term that was added to the nominal torsion strength. The concrete contribution to the torsion strength was originally postulated by Cowan as the nominal torsion strength for plain concrete using the elastic theory, T_e, given by Eq. (4.22). Testing [Hsu (1984)], however, showed that the concrete term is between

0 and T_e. Various theories have been proposed to explain the source of concrete shear/torsion resistance. Hsu [Hsu (1984)] proposed that considering shear deformation of the concrete compressive struts into the space frame approach produces accurate torsional strength predictions of reinforced concrete members. Collins and Mitchell [Collins and Mitchell (1991)], on the other hand, propose that residual post-cracking tensile strength of concrete correctly explains the phenomenon (see Section 4.4).

Though the truss analogy provides a conservative estimate of the torsional capacity of lightly-reinforced members, it does provide a clear picture of torsion load transfer mechanisms. Notably, the truss analogy predicts that longitudinal reinforcement is recruited just as heavily as the stirrup reinforcement in resisting torsional loads. The longitudinal reinforcement will, therefore, extend to accommodate the stress, and if the member is restrained from extension (as may occur in a building system or bridge) a beneficial self-prestressing effect may occur.

Effect of Prestressing on Concrete Torsional Strength As many concrete bridges are prestressed, it is convenient to understand the effect of prestressing on the strength of concrete members. For members prestressed along the neutral axis (i.e., no bending stress), a state of biaxial stress exists (shears from pure torsion and compressive axial from prestressing).

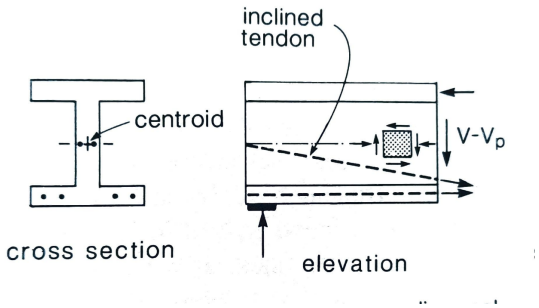

Figure 4.7: Biaxial stress state for prestressed members subject to shear or torsion loads, from [Collins and Mitchell (1991)]

For plain concrete, the increase in the cracking stress from prestressing is determined from a principal stress analysis [Collins and Mitchell (1991)]. The net effect of the prestressing is to increase the torsional strength of the beam by a prestressing factor γ_p:

$$\gamma_p = \sqrt{1 + \frac{f_{pc}}{f_{cr}}} \tag{4.25}$$

where:

f_{pc} = compressive stress in concrete due to prestressing

f_{cr} = concrete cracking stress

4.4 Development of the MCFT for Shear

As demonstrated in Section 4.1, pure torsional loading produces a stress state composed only of shear stresses; thus, shear and torsion are heavily linked. This section presents a brief aside into the development of a rational shear theory, the Modified Compression Field Theory (MCFT). The MCFT provides insight into shear mechanisms that will be helpful in predicting torsional responses. The theory also provides a foundation for response prediction to combined load scenarios.

Before the development of the MCFT, early shear models assumed a truss behavior that was analogous to Rausch's space truss for torsion. The shear truss models assumed shear was resisted by compressive forces in concrete struts inclined at 45 degrees and that stirrups developed tension forces to resist the concrete strut thrust. For lightly reinforced sections, the truss models produce conservative strength predictions because concrete tensile forces are not captured. Additionally, the crack inclination angle is commonly shallower than 45 degrees. This fact makes the truss models even more cautious. Plasticity methods allow designers to choose a value of θ, but this method is subject to arbitrary limits on θ and the concrete compressive strength, f_{2max}. In using this approach, the designer may not see a clear, rational methodology.

Development of the compression field theory (CFT)—an early implementation of the MCFT—eliminated the need for arbitrary design choices; the CFT uses a strain compatibility condition, Eq. (4.26), to determine the principal compressive stress angle. Unlike the previously discussed skew-bending theories that only predicted equilibrium based on a crack inclination angle, the CFT and MCFT can predict the full load-deformation response of a member. These theories are of a broader class of models called rotating angle models, in which the angle of principal compression is assumed to update orientation with changing stress states. Equation (4.26) can be derived (see Appendix A) by summing the shear distortions that arise from a linear superposition of three linearly-independent strains (ϵ_z, ϵ_t and ϵ_2). The inclination angle, θ, is the angle that minimizes the shear distortion [Hsu (1984)].

$$\tan^2\theta = \frac{\epsilon_z + \epsilon_2}{\epsilon_t + \epsilon_2} \tag{4.26}$$

In Eq. (4.26), θ is the angle of principal compression stresses, ϵ_z is the longitudinal strain, ϵ_t is the transverse strain, and ϵ_2 is the principal compressive strain. All

strains are taken as tension positive. Additional compatibility relationships are used in the CFT to determine the principal tensile strain and the web shear-strain:

$$\epsilon_1 = \epsilon_z + \epsilon_t - \epsilon_2 \tag{4.27}$$

$$\gamma_{yz} = 2(\epsilon_z - \epsilon_2)\cot\theta \tag{4.28}$$

Strain components are shown for a typical shear-panel in Fig. 4.8.

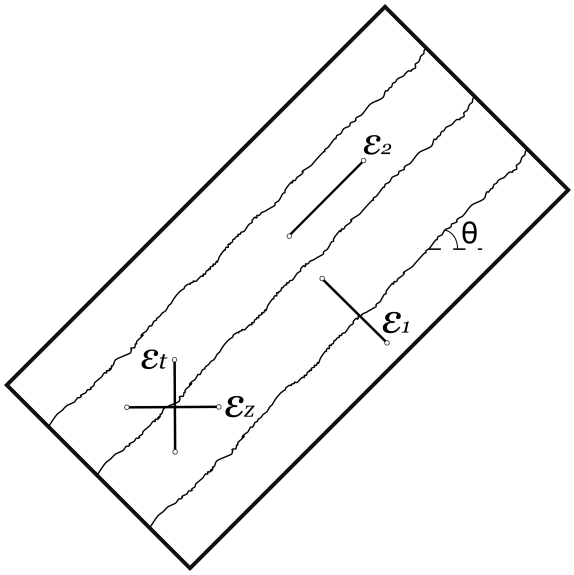

Figure 4.8: Average strains (across multiple cracks) in a cracked element

Shear panels were tested in the University of Toronto's panel tester [Vecchio and Collins (1986)] to develop the concrete constituitive laws for diagonally cracked concrete. The panel tester can subject a panel element to various biaxial stress states to replicate a pure-shear load condition, which is impossible to replicate in beam experiments. Vecchio and Collins' stress-strain relationship for diagonally cracked concrete, Eq. (4.29), captures the dependence of the peak compressive

strength on the principal tensile strain, ϵ_1.

$$f_2 = \frac{f'_c}{0.8 + 170\epsilon_1}\left[2\left(\frac{\epsilon_2}{\epsilon'_c}\right) - \left(\frac{\epsilon_2}{\epsilon'_c}\right)^2\right] \tag{4.29}$$

Diagonally cracked concrete experiences much higher tensile strains than traditional test cylinders, and the compression strength expression is reduced to reflect this. Hsu calls this effect the 'softening' of diagonally cracked concrete, as shown in Fig. 4.9.

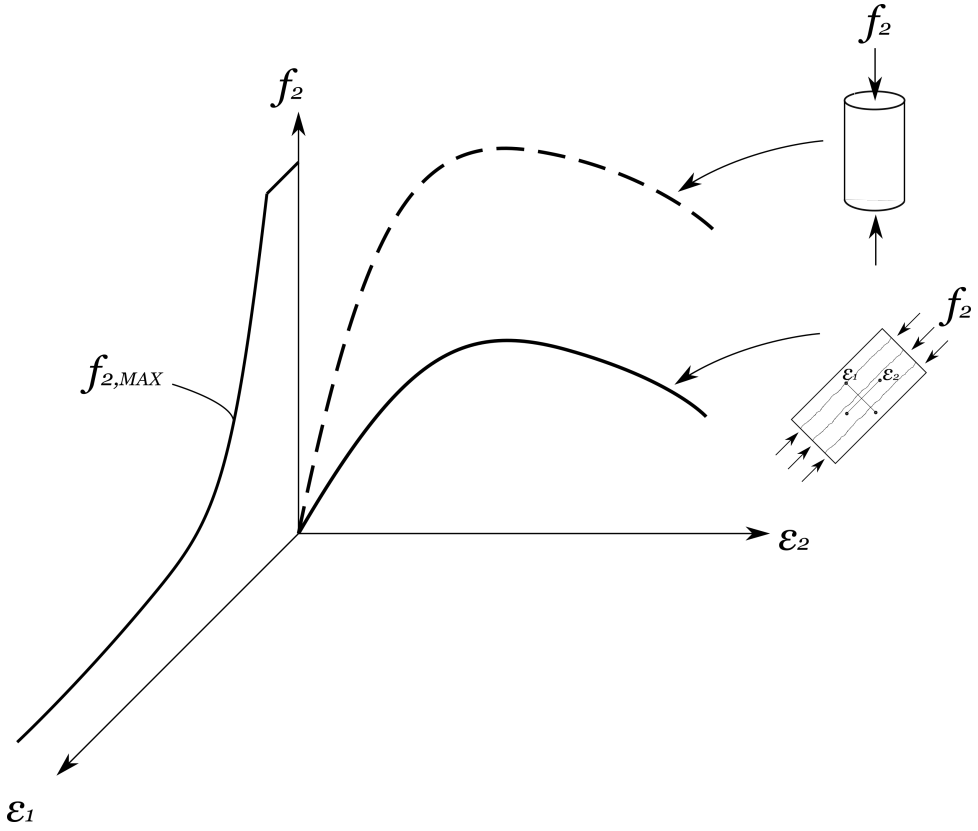

Figure 4.9: Stress-strain behavior for diagonally cracked concrete, adapted from [Vecchio and Collins (1986)]

In 1986, The CFT was extended to include the effect of concrete tensile stresses between cracks [Vecchio and Collins (1986)]. This modification led to the MCFT, which reduced the conservatism of the CFT formulation. The MCFT equilibrium equations for average stresses across multiple cracks are derived from Fig. 4.10.

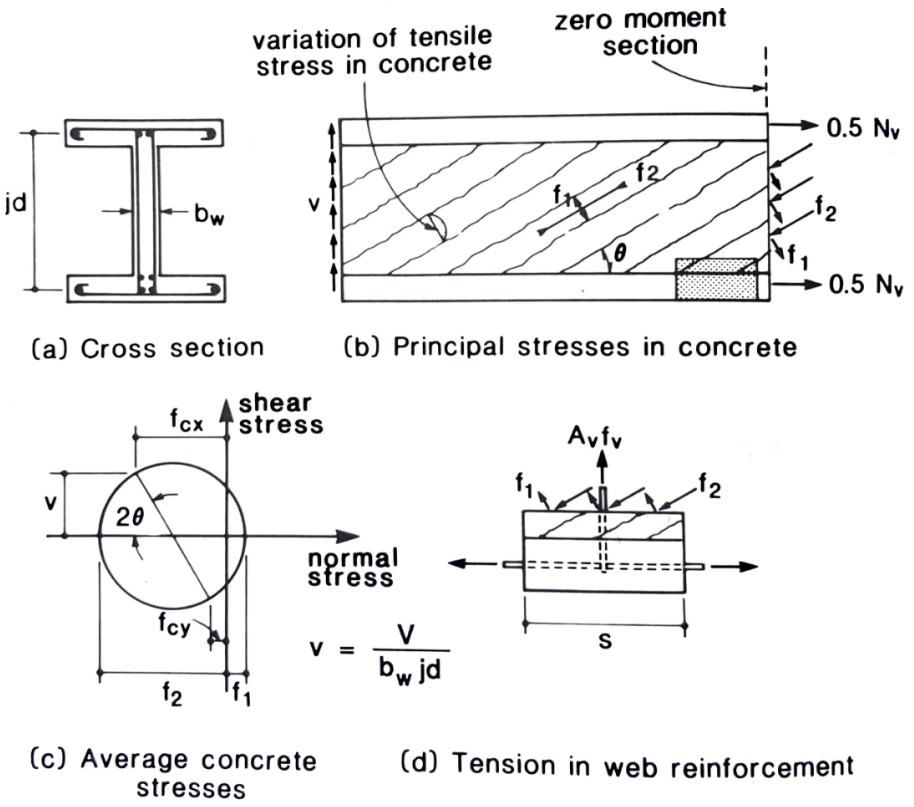

Figure 4.10: MCFT Equilibrium conditions for the case of pure shear loading, copied from [Collins and Mitchell (1991)]

Equations (4.30) and (4.31) capture transverse and longitudinal equilibrium for pure shear loading, where A_v, A_l, A_p are the areas of transverse steel, longitudinal bars, and prestressing tendons, respectively. Stirrups are spaced at a distance, s, and the web thickness is b_w.

$$A_v f_v = (f_2 sin^2\theta - f_1 cos^2\theta) b_w s \tag{4.30}$$

$$A_l f_l + A_p f_p = (f_2 cos^2\theta - f_1 sin^2\theta) b_w jd \tag{4.31}$$

The MCFT equilibrium equations include concrete tensile stresses. The stresses of the shear panel satisfy the Mohr's circle for stresses, from which Eq. (4.32) is derived.

$$f_2 = \frac{2v}{sin2\theta} - f_1 \tag{4.32}$$

where:

$$f_1 = \frac{0.33\sqrt{f'_c}}{1 + \sqrt{500\epsilon_1}} \tag{4.33}$$

The MCFT contains additional relationships, summarized in Table 4.2, that account for local variations between the cracks. A cracked member must be able to transfer shear forces across the cracks. Concrete stresses drop to zero at a crack, so local shear must be resisted by reinforcement stresses and aggregate interlock. Upon reinforcement yield, any additional shear must be transmitted by stresses, v_{ci}, along the crack interface. The shear transfer across crack interfaces depends on the crack width, w, and aggregate size, a. Calculation of the average concrete tensile stress between cracks, Eq. (4.34), must account for local crack conditions, in case interface shear or steel yield controls the shear capacity.

Table 4.2: Overview of MCFT crack conditions, from [Collins and Mitchell (1991)]

EQUILIBRIUM	COMPATIBILITY	CONSTITUITIVE
$f_1 = v_{c_i} \tan\theta + \frac{A_v}{sb_v}(f_{v_y} - f_v)$ (4.34)	$w = \frac{\epsilon_1}{\left(\frac{\sin\theta}{s_{mx}} + \frac{\cos\theta}{s_{mv}}\right)}$ (4.35)	$v_{c_i} = \frac{0.18\sqrt{f_c{}'}}{0.3 + \frac{24w}{a+16}}$ (4.36)

The MCFT equilibrium, compatibility and constituitive laws can be implemented into a response prediction scheme for pure shear loading of a 2D-membrane element. The following solution algorithm, called SHEAR, is presented by Mitchell and Collins [Collins and Mitchell (1991)]. The SHEAR program assumes that clamping stresses are negligible and that the shear stress remains constant throughout the depth of the shear web. The solution algorithm is shown graphically in the flowchart of Fig. 4.4.

1. Choose a value of the principal tensile strain, ϵ_1, at which to perform the analysis.

2. Assume a trial value for the inclination angle of the principal compressive stress, θ. High levels of prestressing force produce shallow angles and high clamping forces produce steep angles. Internal shear will increase with decreasing inclination angles.

3. Assume the stress in the stirrup reinforcement, f_v.

4. Calculate the concrete principal tensile stress, f_1. To ensure that the local equilibrium conditions at a crack are satisfied, f_1 is taken as the minimum of Eqs. (4.33) & (4.34).

5. Calculate the shear capacity, V. Combination of Eqs. (4.30) & (4.32) produces the following shear force expression, where V_p is the vertical component of the prestressing force:

$$V = f_1 b_w jd \cot\theta + \frac{A_v f_v}{s} jd \cot\theta + V_p \tag{4.37}$$

6. Calculate the concrete principal compressive stress, f_2 via Eq. (4.32), where shear stress, v is found as:

$$v = \frac{V - V_p}{b_w jd} \tag{4.38}$$

If θ is assumed too low in Step 2, the shear force may increase to a point at which equilibrium, Eq. (4.32), cannot be satisfied before f_2 exceeds $f_{2_{max}}$, where

$$f_{2_{max}} = \frac{f'c}{0.8 + 170\epsilon_1} \tag{4.39}$$

If $f_2 > f_{2_{max}}$ revise estimate of θ.

7. Calculate principal compressive strain, ϵ_2. Reorganization of Eq. (4.29) gives the smaller solution[1] (see Fig. 4.9) as:

$$\epsilon_2 = \epsilon_c{}' \left(1 - \sqrt{1 - \frac{f_2}{f_{2max}}}\right) \tag{4.40}$$

8. Calculate transverse strain, ϵ_t. Rearrange Eq. (4.26).

9. Calculate longitudinal strain, ϵ_x. Rearrange Eq. (4.27).

10. Check f_v assumption and return to Step 3. $f_v = E_s\epsilon_t \leq f_{v_y}$.

11. Check longitudinal equilibrium. Update θ and return to Step 2. Repeat until equilibrium is achieved. Use of tangent stiffness method with overshoot avoidance is suggested.

[1]This algorithm does not capture post-peak behavior

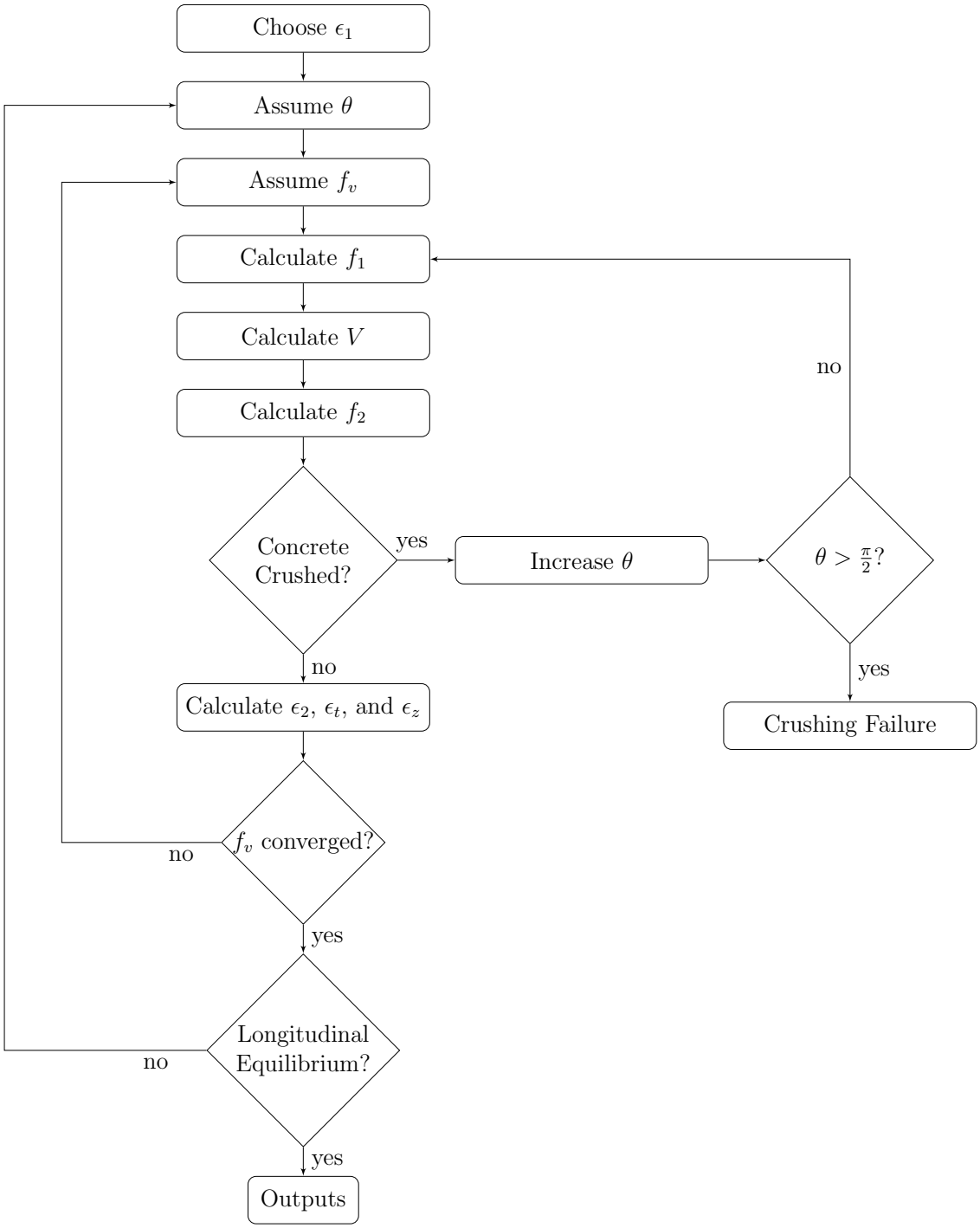

Figure 4.11: Flow chart for SHEAR program

4.5 MCFT Torsion Equations

The CFT compatibility equations, Eqs. (4.26)–(4.28), were derived (Appendix A) for a general deformed configuration; thus, the equations are not restricted to the description of shear behavior. Inclusion of additional compatibility equations and modification of the shear equilibrium equations, Eqs. (4.30)–(4.32), allows the MCFT to predict the load-deformation response to various load scenarios, including axial loads, shear loads, bending moments, and torsional moment. Upon inclusion of torsional moments, the problem becomes three-dimensional.

Idealizing a solid section as a thin tube allows the use of Section 4.1.3 to extend the MCFT equilibrium equations for pure torsional loading. In other words, the walls of a beam in torsion can be idealized as shear panels. A thin-walled section will develop circulating shear stresses to resist torsional loads. If the walls are thin, the shear flow can be assumed constant throughout the cross-section. Combining Eqs. (4.14) & (4.15) results in an expression that relates shear flow with applied torque:

$$q = \frac{T}{2A_0} \tag{4.41}$$

Even if the walls are not thin, the thin-tube formulation can still be used. Experiments have shown that hollow concrete sections and solid concrete sections exhibit similar torsional strengths. Concrete near the centroid of the section is not recruited as heavily as the outer layer of concrete because the dependence of shear strain on r. Thus, solid sections can be approximated as hollow sections with an 'effective' wall thickness, t_d, also called the shear flow zone. As briefly mentioned in Section 4.3.1, characterization of the centerline area, A_0, of the space-truss is critical for an accurate prediction of torsional strength. Rausch placed his space truss at the centerline of the stirrup reinforcement, which overestimated the area enclosed by

the shear flow zone centerline and resulted in unconservative torque predictions for high reinforcement ratios. One approach to reduce error in the prediction of A_0 has been proposed by Hsu [Hsu (1968)]. As seen in Fig. 4.6, Hsu decreased Rausch's scale factor of 2 – Eq. (4.24) – with a knockdown factor, α_t, that depends on the aspect ratio of the rectangular beam:

$$T_n = T_c + \frac{A_t f_{vy}}{s}(\alpha_t A_0) \tag{4.42}$$

where:

$$\alpha_t = 0.66 + 0.33\frac{h}{b} \leq 1.5 \tag{4.43}$$

Hsu [Hsu (1990)] gives an expression for the shear flow zone in terms of the principal strains and inclination angle as follows, where $\zeta = f_{2_{max}}/f_c^{'}$ is the softening coefficient for diagonally cracked concrete from Eq. (4.29).

$$t_d = \frac{A_0 \zeta^2}{p_0 \sin^2\theta \cos^2\theta} \tag{4.44}$$

Determination of the shear flow zone is iterative: The effective area, A_0, and the perimeter of the shear flow zone centerline, p_0, are functions of the shear zone thickness, t_d.

$$A_0 \approx A_c - \frac{t_d}{2}p_c \tag{4.45}$$

$$p_0 \approx p_c - 4t_d \tag{4.46}$$

where:

A_c = the concrete area

p_c = the perimeter of concrete

Equilibrium of a diagonal strut element provides a relationship between shear flow and principal stresses that is analagous to Eq. (4.32) from the MCFT pure shear equations.

$$f_2 = \frac{2q}{t_d \sin 2\theta} - f_1 \tag{4.47}$$

Noting the similarities with the shear problem, each face of a torsionally loaded beam can be treated as a shear-panel (Fig. 5.3), such that the equilibrium Eqs. (4.30)–(4.31) can be recycled. Substitution of Eqs. (4.41) & (4.47) into Eqs. (4.30) & (4.31) results in the following equilibrium expressions for pure torsion:

$$A_l f_l + A_p f_p = \frac{T p_0 \cot\theta}{2A_0} - f_1 p_0 t_d \tag{4.48}$$

$$\frac{A_t f_t}{s} = \frac{T \tan\theta}{2A_0} - f_1 t_d \tag{4.49}$$

Equations (4.47)–(4.49) represent the torsion analog to Eqs. (4.32)–(4.31). Note that Eq. (4.49) is derived for an individual wall panel, so A_t is the area of a single stirrup leg, whereas A_v – Eq. (4.30) – is the area of all vertical stirrup legs. An additional compatibility relationship must be introduced to capture the deformation response of diagonal struts in a twisting box section. Concrete struts have been observed to experience both axial and bending stresses during torsional deformation. For a St. Venant torsional member experiencing a constant twist rate, the strut curvature, ψ_d, can be derived as:

$$\psi_d = \phi \sin 2\theta \tag{4.50}$$

where ϕ is obtained from the warping compatibility condition described in Eq. (4.16). The subscript 'd' signifies that the curvature is oriented in the direction of the diagonal strut.

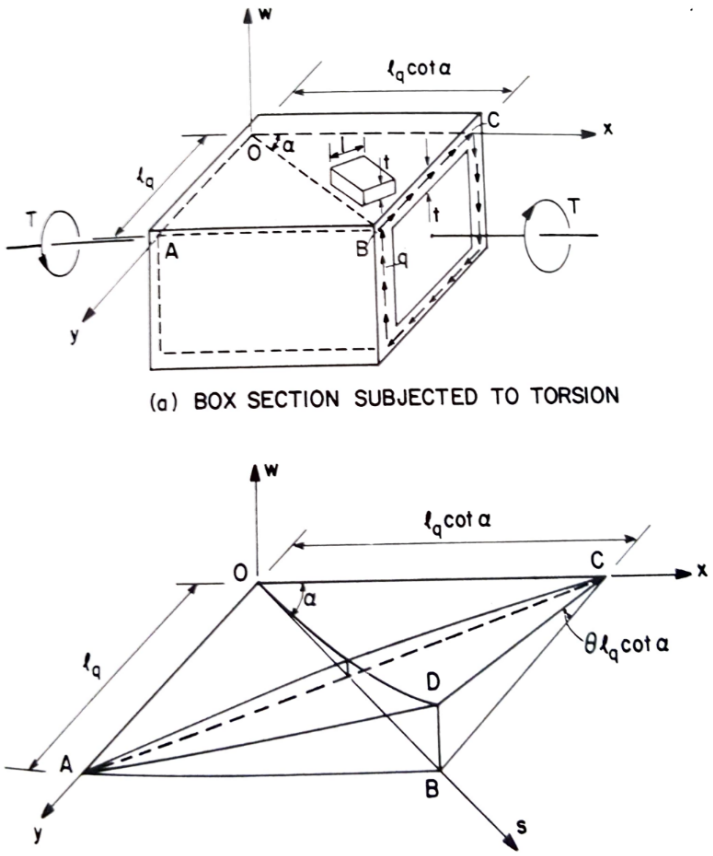

Figure 4.12: Curvature of diagonal concrete strut during twist deformation, from [Hsu (1984)]

Curvature of the concrete strut will produce tensile bending strains on the inside strut face that are aligned with ϵ_2. If, upon superposition of the tensile bending strains with the compressive strains in the concrete strut (ϵ_2), the inside strut face experiences net tension, it will become ineffective as a compression strut. Thus, t_d in Eqs. (4.47)–(4.49) should only consider the thickness of concrete that remains in compression.

Spalling of Concrete Cover If spalling of concrete cover occurs during torsional deformation, the shear flow zone, t_d and torsional capacity will be reduced. Tensile stresses form at the corners of a beam in torsion, where the compressive

stresses change direction. Spalling occurs when the concrete can not resist the tensile stresses. Rahal [Rahal and Collins (1995)] has proposed a spalling criterion, based on experimental data. He proposed that spalling occurs when:

$$K_2 = 0.027 + 0.0135\sqrt{\frac{T}{Vb}} < 0.056 \tag{4.51}$$

where K_2 can be calculated for a reinforced concrete member as:

$$K_2 = \frac{K_1 \int f_2 dz}{\sqrt{f_c{}' b_v}} \tag{4.52}$$

and

$$K_1 = \frac{\Sigma d_{bx} s + d_{bt} p_t}{p_t s} \tag{4.53}$$

The K_1 term is a measure of the amount of reinforcement at the interface of the concrete cover and the reinforcing cage. More boundary reinforcement produces a splitting plane and increases the susceptibility to cover spalling. Rahal has also suggested [Rahal and Collins (1996)] a separate spalling criterion, though only for the determination of spalling at ultimate loads. The cover spalls if:

$$\text{cover} > 0.3\frac{A_0}{p_0} \tag{4.54}$$

The solution algorithm for members subject to pure torsional loads is similar to the SHEAR algorithm, but curvature of the concrete struts and concrete spalling must also be accounted for. The SHEAR algorithm has been modified by the author to account for pure torsional loading in a program called TWIST (Fig. 4.5), as follows:

1. Choose a value of the principal tensile strain, ϵ_1, at which to perform the analysis.

2. Assume a trial value for the inclination angle of the principal compressive stress, θ.

3. Assume a value for the shear flow zone, t_d. At higher twist values, the effective wall thickness may be reduced by cover spalling, Eqs. (4.51)–(4.53), or flexure of the inside strut face, Eq. (4.50).

4. Assume the stress in the stirrup reinforcement, f_t. The subscript $_t$ distinguishes the torsion case from the shear case.

5. Calculate torsion capacity, T, and shear flow, q, Eq. (4.41). Torsion capacity is found by rearranging Eq. (4.49).

6. Calculate the principal tensile stress, f_1. As in SHEAR, f_1 must account for equilibrium at a crack. Equation (4.34) is reworked for pure torsion:

$$f_1 = v_{c_i} \tan\theta + \frac{A_t}{s t_d}(f_{t_y} - f_t) \tag{4.55}$$

f_1 is now taken as the minimum of Eqs. (4.33) & (4.55).

7. Calculate the principal compressive stress, f_2, Eq. (4.47).

8. Check cover spalling. Cover has spalled if K_2 from Eq. (4.52) exceeds the spalling criterion in Eq. (4.51). If spalled, return to Step 3 and update t_d.

9. Calculate principal compressive strain, ϵ_2. Rearrange Eq. (4.29).

10. Calculate transverse strain, ϵ_t. Rearrange Eq. (4.26).

11. Calculate longitudinal strain, ϵ_z. Rearrange Eq. (4.27).

12. Calculate shear strain, γ_{iz}. Equation (4.28) works for both vertical and horizontal wall panels.

13. Calculate the twist-rate. Recall that twist rate, ϕ, and shear strain, γ, are related via the warping compatibility condition from the thin-tube theory, Eq. (4.16). Rearranging gives $\phi = \frac{\gamma p_0}{2A_0}$.

14. Calculate the curvature of the compression struts due to torsional deformation, Eq. (4.50).

15. Check f_t assumption and return to Step 4. $f_t = E_s\epsilon_t \leq f_{t_y}$.

16. Check if inside strut face has gone into tension. If so, update t_d, with the assumption that ϵ_2 from Step 9 acts at the center of the effective strut width. $t_d{}' = \frac{t_d}{2} - \frac{\epsilon_2}{\psi} \leq t_d$.

17. Check longitudinal equilibrium, Eq. (4.48). If required, update θ and return to Step 2.

Verification of the TWIST algorithm can be found in Appendix B.

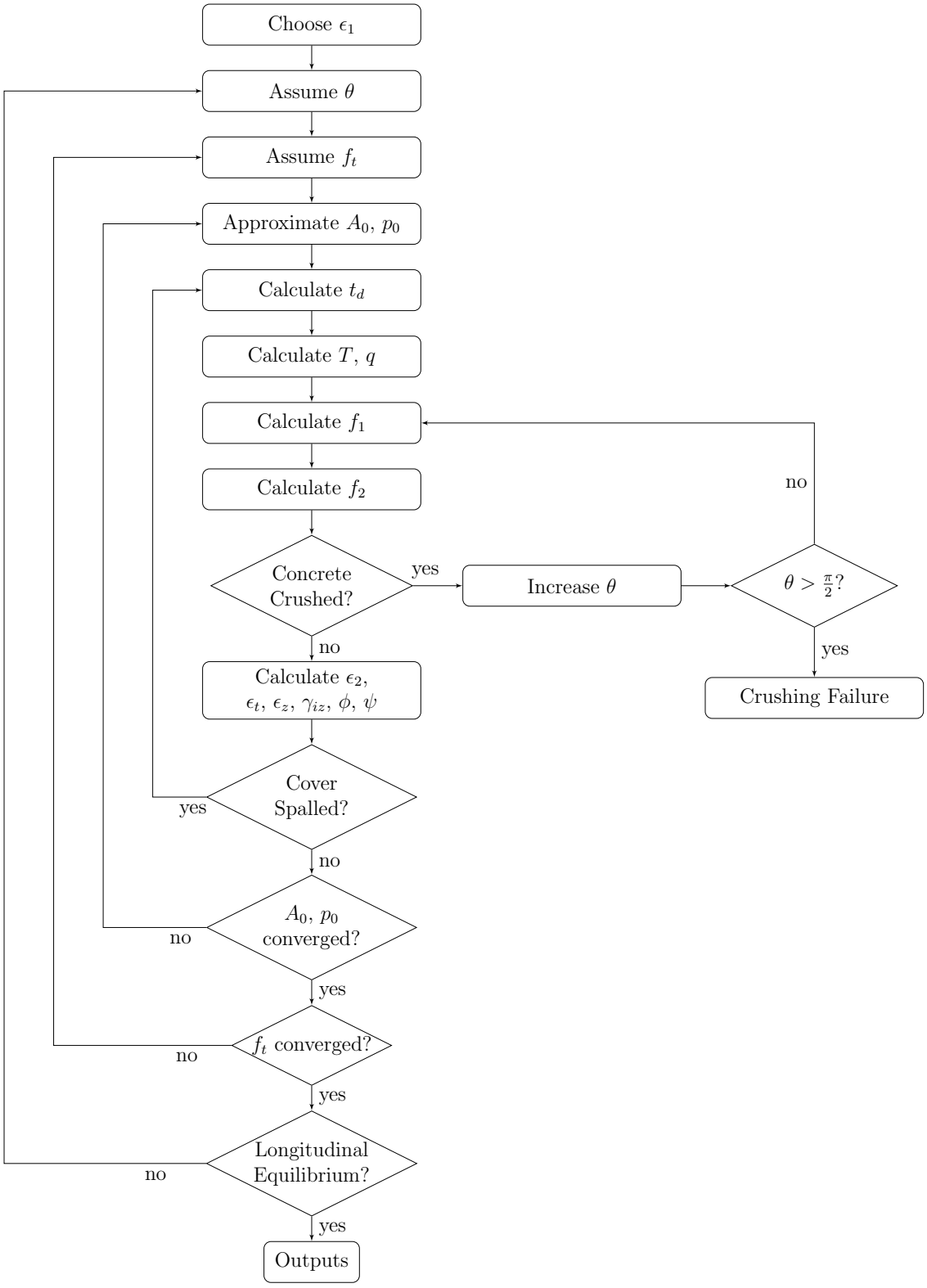

Figure 4.13: Flow chart for TWIST program

CHAPTER 5

COMBINED LOAD ANALYSIS OF BEAMS

5.1 MCFT Combined Load Equations

Sections 4.4 & 4.5 developed the equilibrium, compatibility, and constituitive laws of the MCFT, which were helpful in predicting a panel's response to pure shear loading. The shear equations were then modified to account for torsion. While the MCFT was an important development for the analysis of shear critical structures, pure shear or pure torsional loading rarely exists. A more common as-built condition is a combined load scenario. The following paragraphs discuss the extension of the MCFT for combined load analysis.

Shear and Axial Equation (4.31) shows longitudinal equilibrium of a shear panel for the case of zero applied axial load, but can be rearranged if axial load is applied. No further modifications of the MCFT shear equations are needed to capture the interaction of applied axial load and shear.

$$N = (f_2 \cos^2\theta - f_1 \sin^2\theta) b_w jd - (A_{sx} f_l + A_{px} f_p) \tag{5.1}$$

Positive axial load increases the longitudinal strain, ϵ_z, and increases the inclination angle, θ. Thus, the effect of a tensile axial load is to reduce shear capacity. Conversely, compressive axial load, such as would arise from prestressing, will increase the shear strength of a beam by a factor of $\sqrt{1 + \frac{f_{pc}}{f_{cr}}}$. This is identical to the torsional strength modification factor due to prestressing in Eq. (4.25).

Shear, Axial, and Torsion Introduction of torsional loads makes the problem three-dimensional. The combination of shear and torque loads produces shear

stresses that may differ from one wall panel to the next. Torsional shear flow—Eq. (4.41)—and shear stresses from applied shear forces—Eq. 4.38—will be additive in one side wall and opposing in the other side wall, where the circulatory torsional shear flows opposite the vertical shear. The top and bottom walls will experience only torsional shear flow. Shear stress magnitudes in each wall panel (see Fig. 5.3 for panel labels) are given in Eq. (5.2).

$$\hat{v} = \begin{cases} v + \dfrac{q}{t_d} & \text{Panel 1} \\ v - \dfrac{q}{t_d} & \text{Panel 3} \\ \dfrac{q}{t_d} & \text{Panels 2, 4} \end{cases} \tag{5.2}$$

The difference in wall shear stresses produces different stress and strains distributions in each wall. Equation (5.2) is used to develop the combined shear-torsion analog to Eqs. (4.32) (pure shear) and (4.47) (pure torsion).

$$f_{2_i} = \frac{2\hat{v}_i}{\sin 2\theta_i} - f_{1_i} \tag{5.3}$$

The torsion equilibrium equations, Eqs. (4.48) & (4.49) were derived for a single wall panel (the behavior of all panels is the same for the pure torsion case if constant wall thickness is assumed) and are conveniently adapted for combined shear-torsion, where each wall panel must be considered separately. It is useful to substitute f_{2_i} from Eq. (5.3) into each equilibrium equation. The resulting two equations describe longitudinal and transverse equilibrium of wall panels for the case of combined shear, torsion, and axial load.

$$\frac{A_t f_{t_i}}{s} = t_{d_i}(\hat{v}_i \tan\theta_i - f_{1_i}) \tag{5.4}$$

$$N = \left(\sum_{i=1}^{4} (\hat{v}_i \cot\theta_i - f_{1_i}) t_{d_i} j d_i \right) - (A_l f_l + A_p f_p) \tag{5.5}$$

The principal compressive strain inclination angles for each of the four wall panels can be determined from equilibrium considerations, as will be discussed in step 19 of Section 5.3.

Compatibility conditions for combined shear-torsion require modification from the pure shear or pure torsion load scenarios. In pure torsional loading, a simple expression—Eq. (4.16)—was derived for the twist rate, ϕ, due to shear strains, γ, in the walls, assuming each wall panel of a box had the same thickness. A similar expression can be derived for combined shear and torsion, where the shear contribution from each panel must be considered separately.

$$\phi = \frac{(\gamma_1 + \gamma_3)d_0 + (\gamma_2 + \gamma_4)b_0}{2A_0} \tag{5.6}$$

The shear and torsional strength of a section can be determined from the shear and torsion equilibrium equations—Eqs. (5.3)-(5.5)—in conjunction with the CFT compatibility equations—Eqs. (4.26)-(4.28)—as well as the additional compatibility conditions for strut curvature—Eq. (4.50)—and section twist-rate—Eq. (5.6). The MCFT stress-strain relationship for softened concrete—Eq. (4.29)—remains relevant.

Shear, Axial, Moment, and Torsion Upon the introduction of a moment, the longitudinal strain is no longer constant across the beam's depth. If the strain distribution is known, moment equilibrium can be satisfied. In choosing the strain distribution, one must select a depth at which to evaluate ϵ_z, where ϵ_z is the longitudinal strain calculated for the case of shear, torsion, and axial loads. For sections with transverse reinforcement, significant shear stress distribution can occur such that the highly strained fibers redistribute shear stresses to the less strained fibers. The effect of shear redistribution is that ϵ_z can be evaluated at mid-depth for sec-

tions containing transverse reinforcement [Collins and Mitchell (1991)]. If plane sections are assumed to remain plane[1], the variation of strains through the beam depth is linear. The linear strain distribution will produce the following longitudinal constant curvature due to the top and bottom panels (panels 2 and 4 respectively):

$$\psi_{l,24} = \frac{\epsilon_{z_4} - \epsilon_{z_2}}{d} \tag{5.7}$$

Additionally, there is longitudinal curvature from the difference in longitudinal strains of the side panels (panels 1 and 3):

$$\psi_{l,13} = \frac{\epsilon_{z_1} - \epsilon_{z_3}}{b} \tag{5.8}$$

Variations in transverse strains of the wall panels also produce transverse curvatures, $\psi_{t,24}$, $\psi_{t,13}$.

Longitudinal and transverse curvatures have components in the direction of the diagonal ($_d$) compression struts that adds to the strut curvature from Eq. (4.50):

$$\psi_d = \begin{cases} \phi \sin 2\theta_1 - \psi_{l,13} \cos^2 \theta_1 - \psi_{t,13} \sin^2 \theta_1 & \text{Panel 1} \\ \phi \sin 2\theta_2 - \psi_{l,24} \cos^2 \theta_2 - \psi_{t,24} \sin^2 \theta_2 & \text{Panel 2} \\ \phi \sin 2\theta_3 + \psi_{l,13} \cos^2 \theta_3 + \psi_{t,13} \sin^2 \theta_3 & \text{Panel 3} \\ \phi \sin 2\theta_4 + \psi_{l,24} \cos^2 \theta_4 + \psi_{t,24} \sin^2 \theta_4 & \text{Panel 4} \end{cases} \tag{5.9}$$

Increasing moment decreases the shear and torsion capacity of a section due to increased longitudinal strain, ϵ_z, because large positive longitudinal strains increase the angle of the principal compressive stresses.

[1]The assumption of PSRP is unsatisfying if the torsional load ratio is high, since torsion induces cross-section warping for non-circular sections.

5.2 Combined Loading Analysis: Existing Truss Models

This section discusses various truss model theories that have been proposed for combined load analysis. Though the implementation of each model is slightly different, they can all be understood based on the theory presented in Section 5.1.

Rabbat and Collins' Variable Angle Space Truss Model An early method for prediction of combined load response was Rabbat and Collins' Variable Angle Space Truss Model (VASTM) [Rabbat and Collins (1978)]. The VASTM idealizes rectangular members as four concrete wall panels and four longitudinal chords, consisting of reinforcement encased in a concrete block. The real reinforcement is distributed into the four corners such that the area centroid of the idealized reinforcement is in the same location as that of the real reinforcement. The VASTM idealization is shown in Fig. 5.1

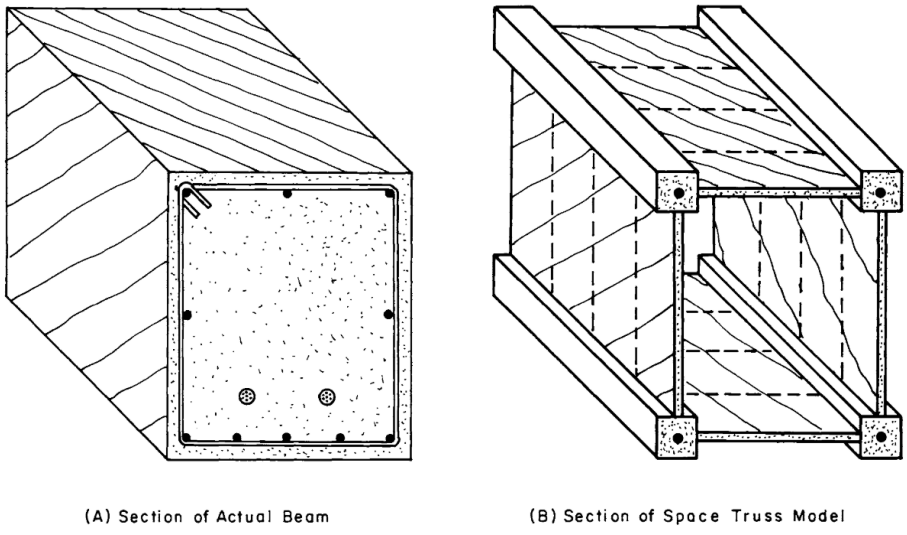

Figure 5.1: VASTM idealization of a cracked member subject to combined loads, taken from [Rabbat and Collins (1978)]

The cracked concrete wall panels are assumed to exhibit no tensile strength and the compression strength is taken as that of a standard compression cylinder. Applied

loads are resisted by axial tension or compression in the chords or by the development of uniform shear stresses in the wall panels, which develop cracks whose inclination depends on the amount of reinforcement and the applied loads.

Rahal's MCFT for Combined Shear and Torsion Nearly 20 years after publication of the VASTM, Rahal [Rahal and Collins (1995)] improved on the VASTM by considering concrete tensile strength, softened concrete constituitive laws, and an experimental cover spalling criterion. Rahal's model treats applied loads as circulating shear stresses in four concrete wall panels of varying thickness, which is determined from equivalent stress block analysis. Strain compatibility in each wall panel is determined from the CFT compatibility equations. Different longitudinal strains in each panel produce curvatures in the beam. The assumption that plane sections remain plane links the strains of the four wall panels.

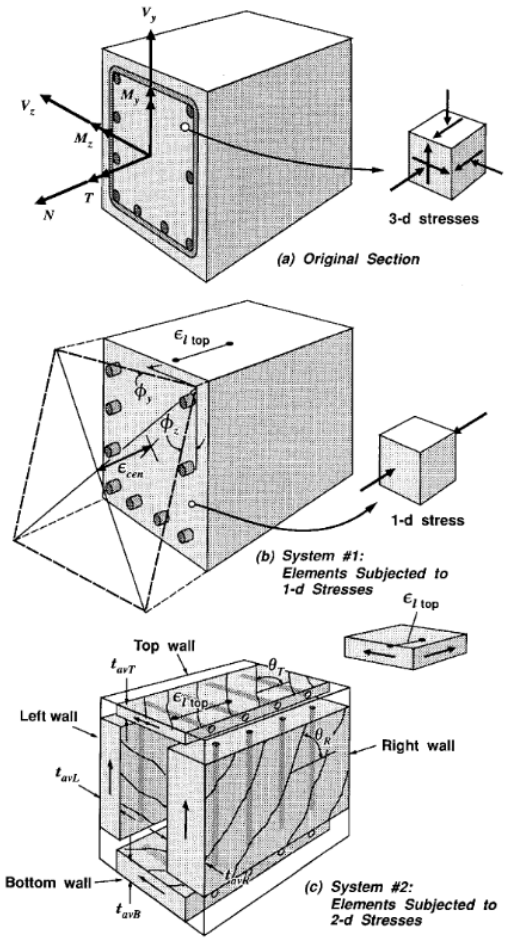

Figure 5.2: Rahal's idealization of a rectangular beam in combined loading as a space truss

As a result of the curvature induced in the struts from twist, Rahal assumes a linear torsional shear stress profile in the shear flow zone. The wall thicknesses are calculated based on constant curvature values from the PSRP assumtion. Rahal [Rahal and Collins (1995)] omits details about how he calculated twist to determine the torque-twist response of a member subject to combined loads.

Greene's CA-STM for Combined Shear, Torsion, and Bending Most recently, an approach has been presented by Greene [Greene and Belarbi (2009)] that

idealizes a rectangular beam as four wall panels, whose thicknesses are determined from shear flow zone calculations.

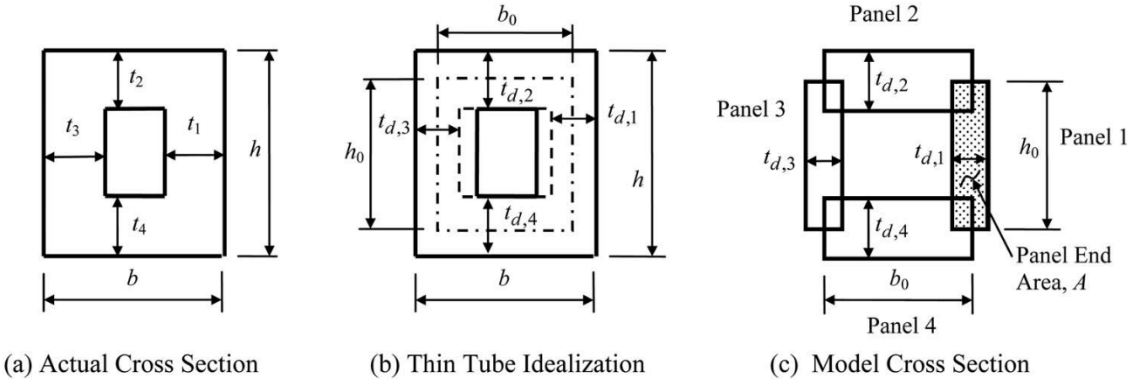

Figure 5.3: Greene's idealization of a combined load member as a series of shear panels

Plane sections are assumed to remain plane, as in Rahal's approach. Greene uses constituitive laws based on Hsu's Softened Truss Model (STM), but calibrated from experimental data for reinforced concrete under pure torsion [Greene and Belarbi (2009)]. Additionally, Greene developed a novel approach for the distribution of reinforcement between panels to better describe the response of asymmetrically reinforced members. Unlike Rahal, Greene presents a rational approach for the calculation of member twist, based on the shear strains in each of the wall panels.

5.3 Combined Shear-Torsion-Bending Algorithm

The models of Section 5.2 are all based on a truss model approach. A hybrid truss model for combined loads, based on the above models, is presented below to account for concrete tensile stresses via the MCFT equilibrium expressions. The proposed model for the analysis of torsion, shear and axial load, (TOR-SHEAR-N), borrows aspects from each of Rabbat's, Rahal's and Greene's theories. Like Rabbat's

VASTM, this model distributes reinforcement to exist at the center of panels or the corner of intersection panels. Proper reinforcement distribution eliminates the assumption that plane sections remain plane, which may be unsatisfying for high torque loads. The proposed model uses the MCFT equilibrium equations, as in Rahal's model. Finally, following Greene's lead, the proposed model includes an expression for the section twist-rate based on the shear strains in each panel. The proposed algorithm is provided in the following steps, which are summarized in Fig. 5.4.

1. Specify the load ratios, $\Delta = \frac{M}{M+Vb}$, $\delta = \frac{T}{T+Vb}$

2. Select a value for the twist rate, ϕ.

3. Approximate the area enclosed by the centerline of the shear flow zone and the perimeter of the shear flow zone, A_0 and p_0.

4. Guess inclination angles, θ_i in all four panels.

5. Guess principal tension strains, ϵ_{1_i}, in all four panels.

6. Calculate the strut thickness for each wall panel, t_{d_i}, using Eq. (4.44) [2].

7. Guess transverse reinforcement stress, f_{t_i}, in all four panels.

8. Calculate principal tensile stress in each panel, f_{1_i} as the minimum value from Eqs. 4.33 & 4.55.

9. Calculate V and v_i. Expressions analogous to 4.37 & 4.38 are shown here, assuming that vertical shear is only resisted by the side panels.

$$V = (v_1 t_{d_1} + v_3 t_{d_3}) d_0 \tag{5.10}$$

[2] As mentioned in Section 4.5, determination of the shear flow zone and effective torsion area is iterative. However, this iteration step has been removed by using Hsu's 'knockdown' factor of the enclosed area, $\alpha_t/2$. This choice allows t_{d_i} to be calculated directly, if A_0 in Eq. (4.44) is replaced by $\alpha_t A_0$ from 4.42

$$v_i = f_{1_i} \cot\theta_i + \frac{A_t f_{t_i}}{t_{d_i} s} \cot\theta_i \tag{5.11}$$

10. Calculate torsional shear flow, q, internal torsion, T. Once q is calculated, the internal torsion resistance is calculated from Eq. (4.41), replacing A_0 with A_1 from Eq. (4.42). The shear flow is solved for by combination and reorganization of Eqs. (4.41) & (5.10).

$$q = \frac{\delta(v_1 t_{d_1} + v_3 t_{d_3})}{2(1-\delta)} \tag{5.12}$$

11. Calculate the effective shear stress in each panel, $\hat{v}_i$. Upon calculation of v and q, the effective shear stress in each panel is found from Eq. (5.2).

12. Calculate the principal compressive stress in each panel, f_{2_i} from Eq. (5.3).

13. Calculate the principal compressive strain, ϵ_{2_i}, from Eq. (4.40).

14. Calculate the shear strain in each panel, γ_i, by rearranging Eq. (5.6). The ratio between shear strains in each panel is derived from CFT compatibility, Eq. (4.28).

$$\gamma_1 = \frac{2\phi A_0}{(1+\gamma_3/\gamma_1)\, d_0 + (\gamma_2/\gamma_1 + \gamma_4/\gamma_1)\, b_0} \tag{5.13}$$

where:

$$\frac{\gamma_j}{\gamma_i} = \frac{(\epsilon_{1_j} - \epsilon_{2_j})(f_{1_i} + f_{2_i})\hat{v}_j}{(\epsilon_{1_i} - \epsilon_{2_i})(f_{1_j} + f_{2_j})\hat{v}_i} \tag{5.14}$$

15. Calculate the longitudinal strain in each panel, ϵ_{z_i}, from Eq. (4.28).

16. Calculate the transverse strain in each panel, ϵ_{t_i} from Eq. (4.26).

17. Update f_t assumption, $f_{t_i} = E_s \epsilon_{t_i} \leq f_{t_y}$. Return to Step 7.

18. Update assumption of principal tensile strains, ϵ_{1_i}, from Eq. (4.27). Return to Step 6.

19. Update inclination angle in each panel, θ_i, from a check of equilibrium. Four equilibrium equations are needed, namely, equilibrium of bending moments, torsional moment, and longitudinal force. Note that vertical shear equilibrium is satisfied by the calculation in Step 9. Transverse shear equilibrium is trivially satisfied if the top and bottom panel thicknesses are identical.

Verification of the combined MCFT algorithm, TOR-SHEAR-N, is shown in Appendix C [3]

[3]Currently, the algorithm is only verified for combined torsion-shear-axial loads.

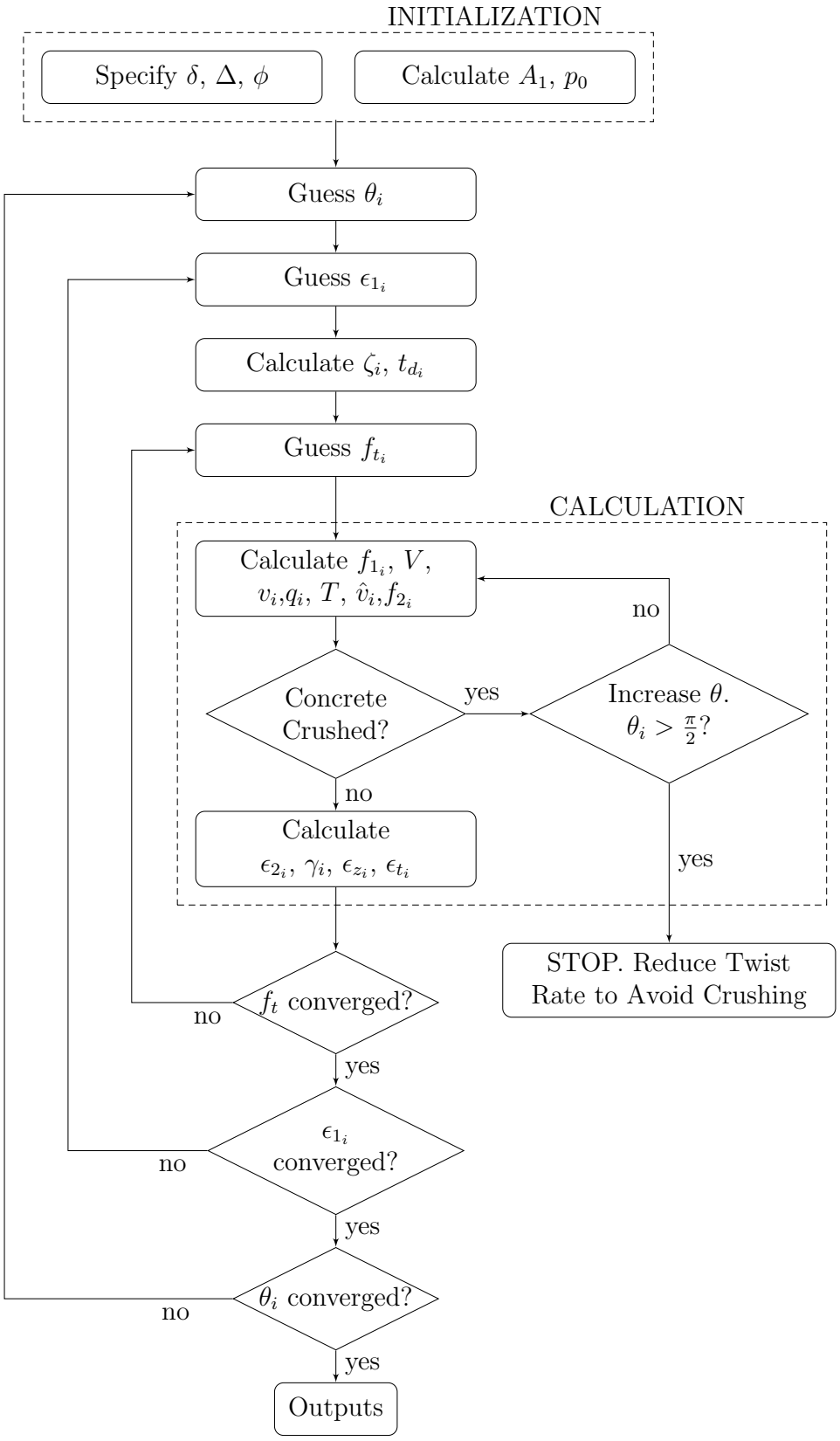

Figure 5.4: Flow chart for CA-MCFT program

5.4 MCFT Design Approach

The MCFT theory can be implemented into a simplified procedure (useful for both analysis and design) for combined loading, proposed by Collins and Mitchell [Collins and Mitchell (1991)]. The theory recasts actions as effective longitudinal strains, where the determination of longitudinal strains conservatively ignores the stiffness contribution of concrete. The longitudinal strain is conservatively taken as zero if a negative value is calculated from Eq. (5.15).

$$\epsilon_z = \frac{\frac{M_n}{jd} + 0.5N_n + 0.5N_v - A_{ps}f_{pe}}{E_sA_s + E_pA_p} \tag{5.15}$$

where:

M_n = applied moment

N_n = applied axial force

N_v = effective axial force (i.e., longitudinal component) from shear and torsion loads

$$N_v = \cot\theta\sqrt{(V_n - V_p)^2 + (\frac{T_n p_0}{2A_0})^2} \tag{5.16}$$

V_n = applied shear

V_p = vertical prestressing force component

f_{pe} = effective pre-stress in tendons after losses

Equation (5.15) assumes that the longitudinal strain occurs at the depth of tension reinforcement. Additionally, the equivalent tension force from shears and torques are assumed to add as the square root sum of squares. Simply adding the two longitudinal force contributions would be over conservative since the effects are additive in one side wall and counteractive in the other.

MCFT parameters, θ and β, are determined from the longitudinal strain, where θ is the principal compressive stress angle and β describes the concrete shear contribution as a function of the concrete tensile strain. From the Simplified Modified Compression Field Theory (SMCFT) [Bentz et al. (2006)]:

$$\theta = 29 + 7000\epsilon_z \tag{5.17}$$

$$\beta = \frac{0.4}{1 + 1500\epsilon_z} \tag{5.18}$$

Upon calculation of θ and β, the stirrup reinforcement can be designed from knowledge of the applied shear and torsion:

$$T_n = \frac{A_t f_y}{s} 2A_0 \cot\theta \tag{5.19}$$

$$V_n = \beta\sqrt{f_c'} b_w jd + \frac{A_v f_y}{s} jd \cot\theta + V_p \tag{5.20}$$

In designing the transverse reinforcement, it is assumed that the total required steel can be taken as the sum of the steel required to resist shear and torsion. Recalling that A_t is the steel area in a single leg, the total area of transverse steel is given (for a single-cell box) as:

$$A_{tot} = 2A_t + A_v \tag{5.21}$$

This simplified procedure can be implemented as an analysis tool for the calculation of ultimate torsion capacity of a section, assuming knowledge of all other loads and reinforcement layout. The analysis procedure is summarized in Fig. 5.5.

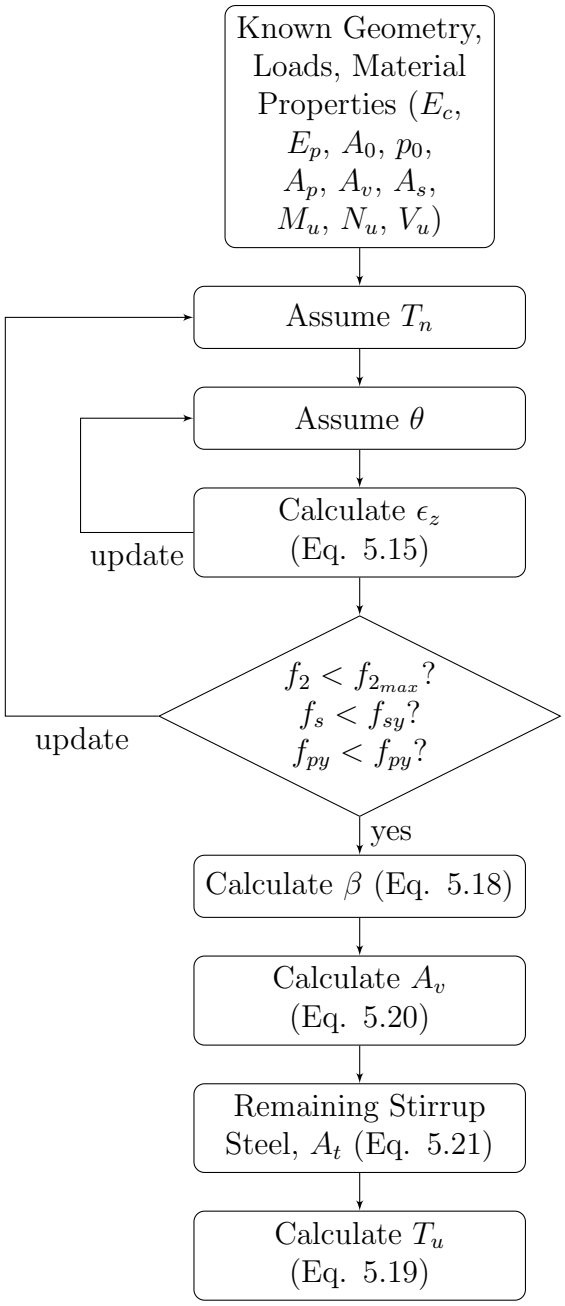

Figure 5.5: Flowchart for Approximate MCFT Combined Load Approach [Collins and Mitchell (1991); Bentz et al. (2006)]

CHAPTER 6

CASE STUDY: MORANDI BRIDGE

6.1 Background

On August 14, 2018, the Morandi bridge in Genoa, Italy partially collapsed after 51 years of service life, killing 43 people. The bridge, situated just a kilometer from the sea, crossed over a heavily industrialized area and the Polcevera river. At the time of collapse there were strong winds and traffic was light. Among the vehicles on the bridge was a truck carrying a steel coil. Had the coil fallen from the truck, the impact load may have affected the collapse sequence. Though the wind load and conceivable coil impact presented potential extreme load events, this chapter focuses on the ramifications of environmental deterioration, which had been a concern for the Morandi Bridge since shortly after construction when the designer remarked on Genoa's marine environment [Morandi (1979)]. The aggressive environment provided the right conditions for the progression of pitting corrosion, an insidious form of degradation that often leads to brittle behavior. In fact, video footage of the collapse [Hasenjager (2019)] reveals a sudden, brittle failure of the Morandi Bridge. Since the collapse, various investigations [Filetto and Lignana (2019); Rosati et al. (2018)] have highlighted advanced reinforcement deterioration in critical sections of the bridge cable-stays. The same post-collapse investigations revealed peculiar construction features that may have diverted large tensile stresses into concrete elements, creating corrosion pathways in the form of microcracks. The final part of this chapter considers the torsional behavior of the main deck to assess whether a potential stay failure would have caused collapse of the main deck, as occured on August 14. First, it is necessary to provide details of the bridge, including salient design features and observations from post-collapse investigations.

An aerial view of the Morandi Bridge is shown in Fig. 6.1, along with a schematic of the overall bridge layout.

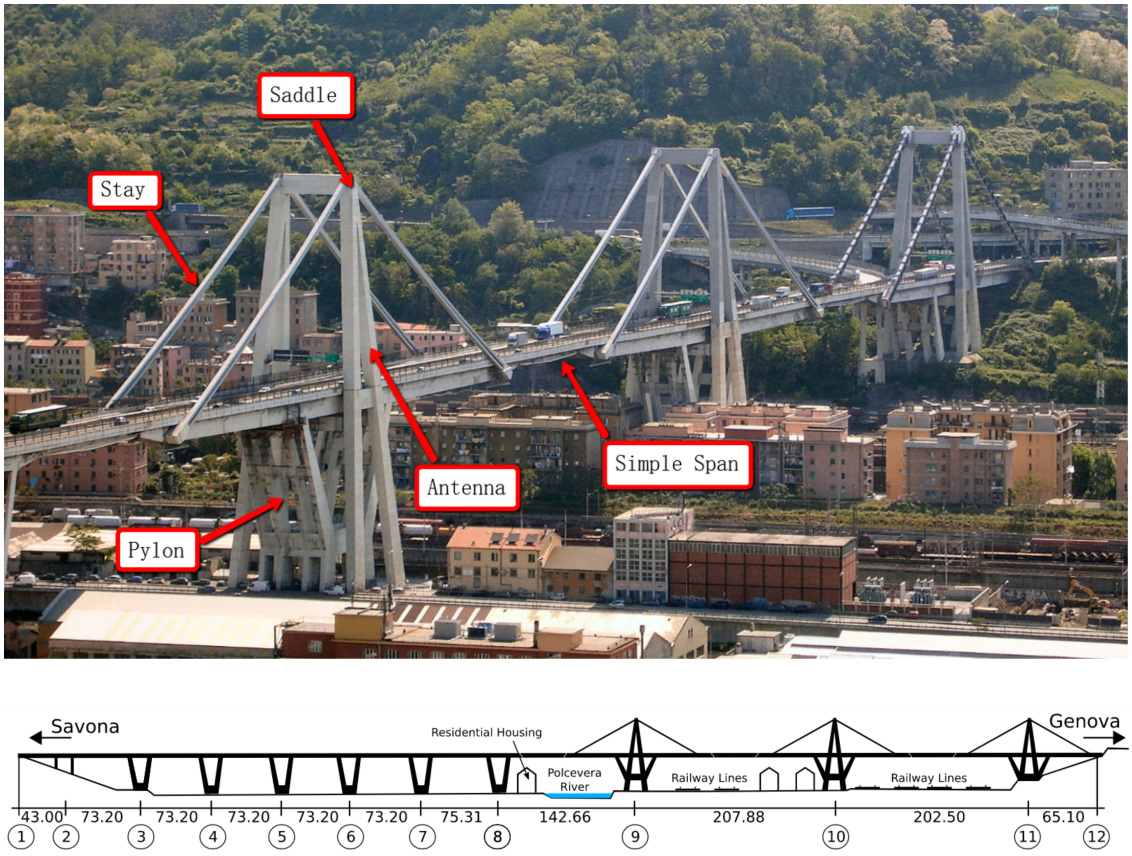

Figure 6.1: Aerial view of the Morandi Bridge balanced systems

6.1.1 Construction of Morandi Bridge Balanced Systems

The Genoa side of the Morandi bridge consisted of three *balanced systems*, numbered as systems 9, 10, and 11. Each balanced system included a five-span roadway that was supported in two locations by pylon supports and in two other locations by prestressed concrete stays. On each side of the *antenna*, a single cable-stay was connected from one deck connection point to the other by draping over a *saddle*

at the top of the antenna. Attention is only given to performance of the balanced systems in this document because failure occurred for balanced system 9.

Construction of Pier and Antenna Construction of the balanced systems began with the pylon and antenna structures. The four inclined pylon support members on either side of the centerline were topped with a transverse link beam. The reinforcement for the link beam is seen extending from the top of the inclined pylon members in Fig. 6.2. The figure also shows temporary metal truss members that were placed between pier supports to act as formwork for the main deck. The pier and the antenna were isolated from each other until the placement of the cable stays completed the structures.

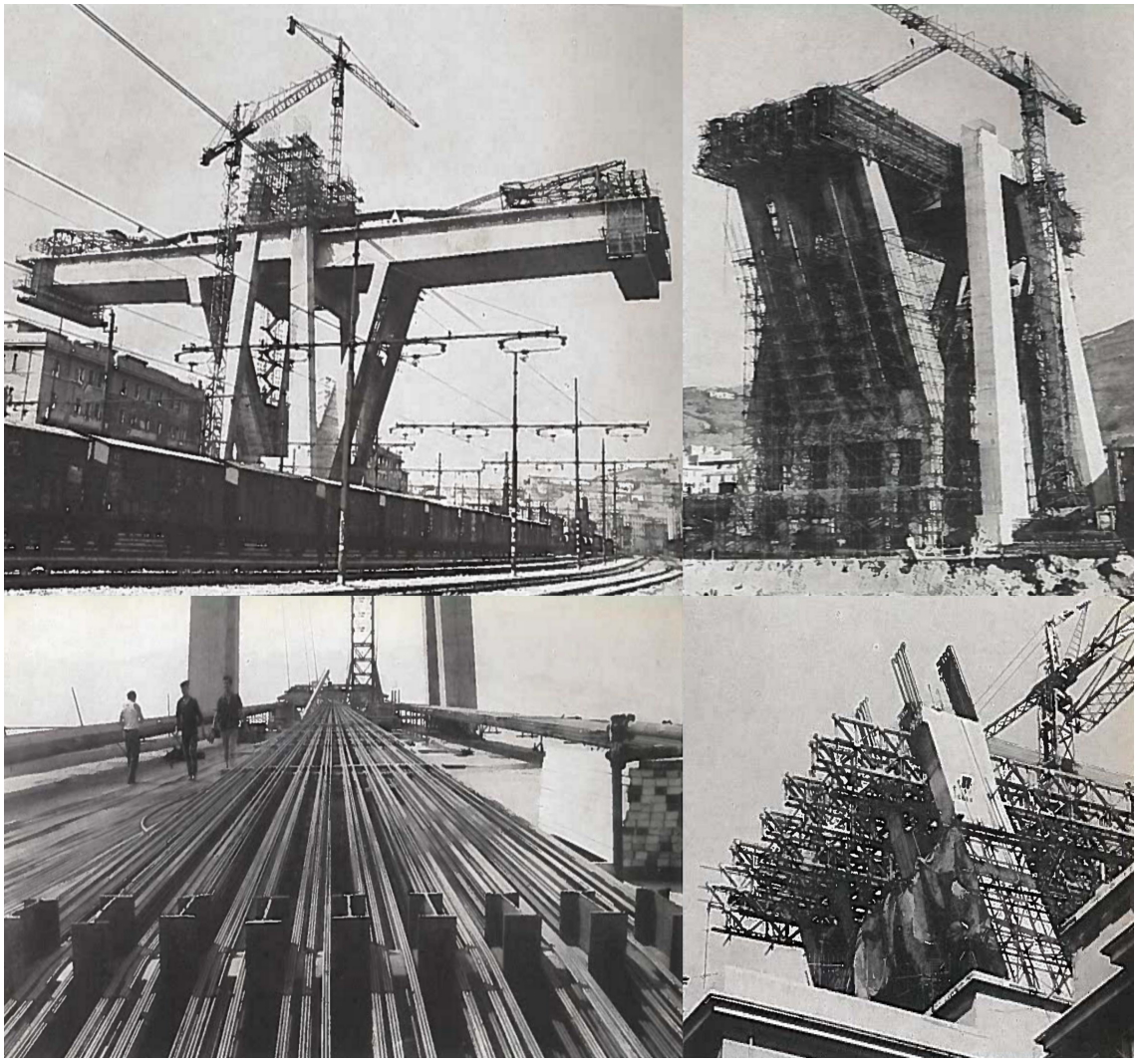

Figure 6.2: Construction of the pier, antenna, and main deck of the Morandi Bridge balanced system

Segmental Construction of Main Deck The main span between pier support and cable support was constructed in segmental fashion, each of the 11 segments (5-5.5m) being connected to the previous by a temporary system of external pre-stressing strands. The strands were called 'harps' by Morandi and can be seen in Fig. 6.2. The segments were constructed with the aid of a mobile metallic formwork, so as to avoid disturbance of the train traffic below the bridge. Negative moment

reinforcement (see Fig. 6.19) at the pier support was stressed to an intermediate stress of 880 MPa upon completion of the first cantilever segment.

Construction of Transverse Beam and Cantilever Segments The final segment of the span between pier and cable supports required casting of another transverse beam, which served as an anchorage for the cable stays. This main transverse beam was heavily reinforced with regular and prestressed reinforcement. The beam weight was supported by temporary (B-series) reinforcement, which draped over the antenna saddle. The transverse beam extended 1.5m beyond the width of the main deck to provide accessibility for stressing operations. After casting and hardening of the transverse beam, the tendon reinforcement within the beam was partially stressed to 490 MPa and the B-series reinforcement was removed. The final steel cables (C-series) that would form part of the cable-stay system were placed and lightly tensioned. Short cantilever spans (10m) were then cast in two segments on either side of the main deck. The temporary 'harp' reinforcement was removed and the negative tendon reinforcement above both transversal beams was stressed to a final stress of 1050-1100 MPa. In the cantilever span, the girder depth tapered from 4.5m to 2.2m at a solid ledge which received the simply-supported span.

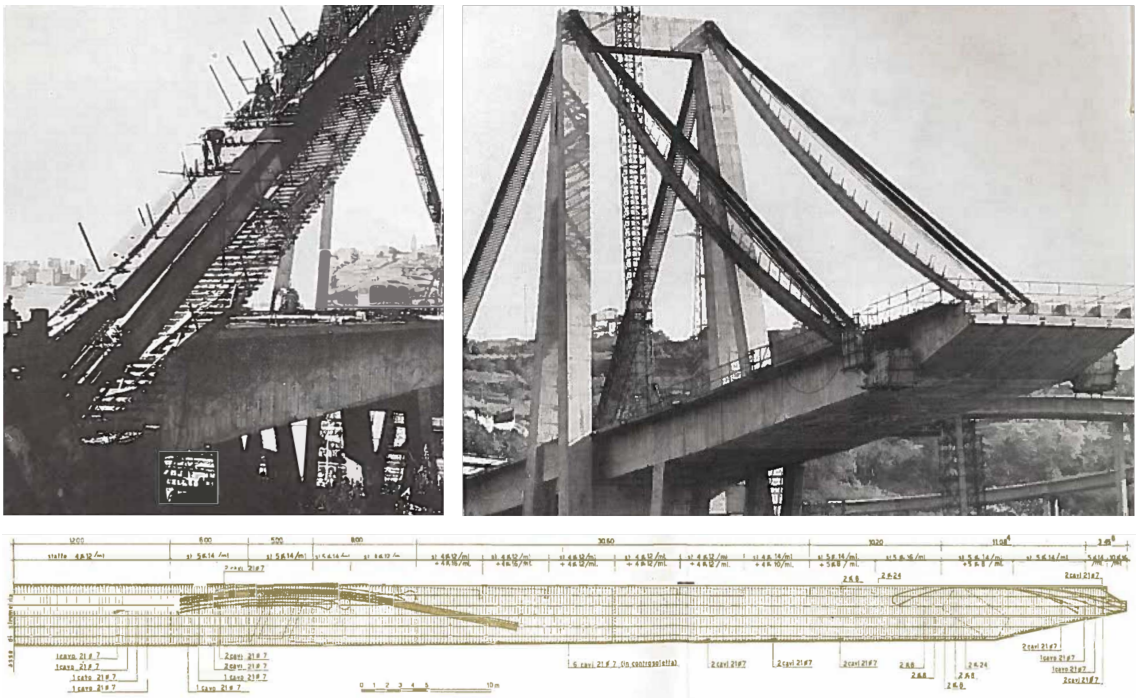

Figure 6.3: State of the Morandi Bridge after casting of the main transversal beam and removal of temporary 'harp' reinforcement

Construction of the Simply-Supported Spans and the Cable Stays After completion of the segmental deck, The reinforcement within the main transverse beam was tensioned to a final tension of 1140 MPa and the tension in the primary (C-series) cable tendons was increased to an intermediate stress of 380 MPa. These actions prepared the main deck to receive the weight of the simply-supported spans, shown in Fig. 6.1. After placement of the simply-supported spans, the stress in the primary tendons increased to 637 MPa. Next, a secondary set of cable-stay tendons (C1-series) was placed parallel to the primary C-series tendons. A concrete sheath was constructed to provide cover for the C-series and C1-series tendons. The sheath was built in 3 m segments starting at the deck level and continuing up to the antenna. A small 5 cm gap was provided between concrete segments to isolate each section from the casting of the others. The casting of short segments allowed the

cables to assume a natural catenary deflected shape while preventing any tension effects in the concrete. The small gaps were filled upon hardening of the existing segments and the secondary C1-series tendons were stressed to 686 MPa, at which point the stresses in the primary and secondary tendons matched. Finally, the system was 'homogenized' — in the designer's words — by the injection of grout into the tendon sleeves.

Throughout the construction process, Morandi monitored the main deck deflection and adjusted the stressing operations accordingly. At the end of the construction phase, cable stay deck attachment points had zero deflection.

6.1.2 Bridge Loads

Throughout the remainder of this chapter, reference will be made to 'internal reports', which are not currently published.

Permanent Loads Upon completion of construction, the primary cable-stay tendons experienced 686 MPa of construction loads, which included self-weight and paving loads for both the main deck and the simply-supported span. The schematic in Fig. 6.7 shows that the area of primary tendons is 32,700 mm^2. Each cable stay supported 22 MN of axial construction load. Additional permanent loads would be added to the bridge throughout its life, starting with the placement of roadway barriers in the 1990's. Three lines of barriers were placed on the bridge, each weighing 18 kN/m. The barriers provided an additional 1850 kN of axial load to each stay. Further permanent loads were added in 2010 when the roadway was widened. This action produced another 1000 kN of axial load to each stay. Note that after the

casting of the cable-stay sheath, the 'homogenized' stays acted compositely to resist the additional permanent loads.

Table 6.1: Additional axial loads in cable stays after completion of construction in 1967

Year	Construction Loads [kN]	Additional Permanent Load [kN]
1967-1990	22000	0
1990-2010	22000	1850
2010-2018	22000	2850

Moving Loads Various moving load scenarios are considered in the analyses of the Morandi Bridge in Sections 6.2-6.3. Moving loads are resisted by composite action of the cable stays. The traffic load scenarios are summarized here:

1. *Truck Overload Scenario*: Section 6.2 analyzes the effect of corrosion on the health of the cable stays. The analysis ignores the fatigue component of moving loads, instead treating moving loads as statically applied. Live load magnitudes are linearly interpolated between the design overloads in 1967 and 2018. The NTC-18 load scenario [Orgnoni (2019)] results in 3000 kN of axial load in one cable stay. Morgese [Morgese et al. (2019)] assumes an increase in truck weight of 450% in the 50-year life of the Morandi Bridge. Assuming this ratio holds between the overload scenarios, a 1967 overload would have produced 670 kN of axial load in a stay.

2. *Fatigue Load Scenario*: Section 6.2.2 investigates the effect of fatigue on the mechanical life of the cable-stay reinforcement. Cyclic load magnitudes are chosen as the standard design truck weights, linearly interpolated from 1967 to 2018, as assumed by Morgese [Morgese et al. (2019)].

3. *Actual Moving Loads During Collapse*: Section 6.3 considers the effect of a potential stay collapse on the torsional behavior of the main deck. For this analysis, it is best to use the known traffic loads present on the bridge at the time of collapse, shown in Fig. 6.4. Lighter car traffic has been assumed to be uniform (2 kN/m), while the truck positions have been extrapolated—internal reports—from collapse debris. Each truck is assumed to be fully loaded (440 kN). Figure 6.4 shows that two trucks would have been supported by the stays on either side of balanced system 9 at the time of collapse.

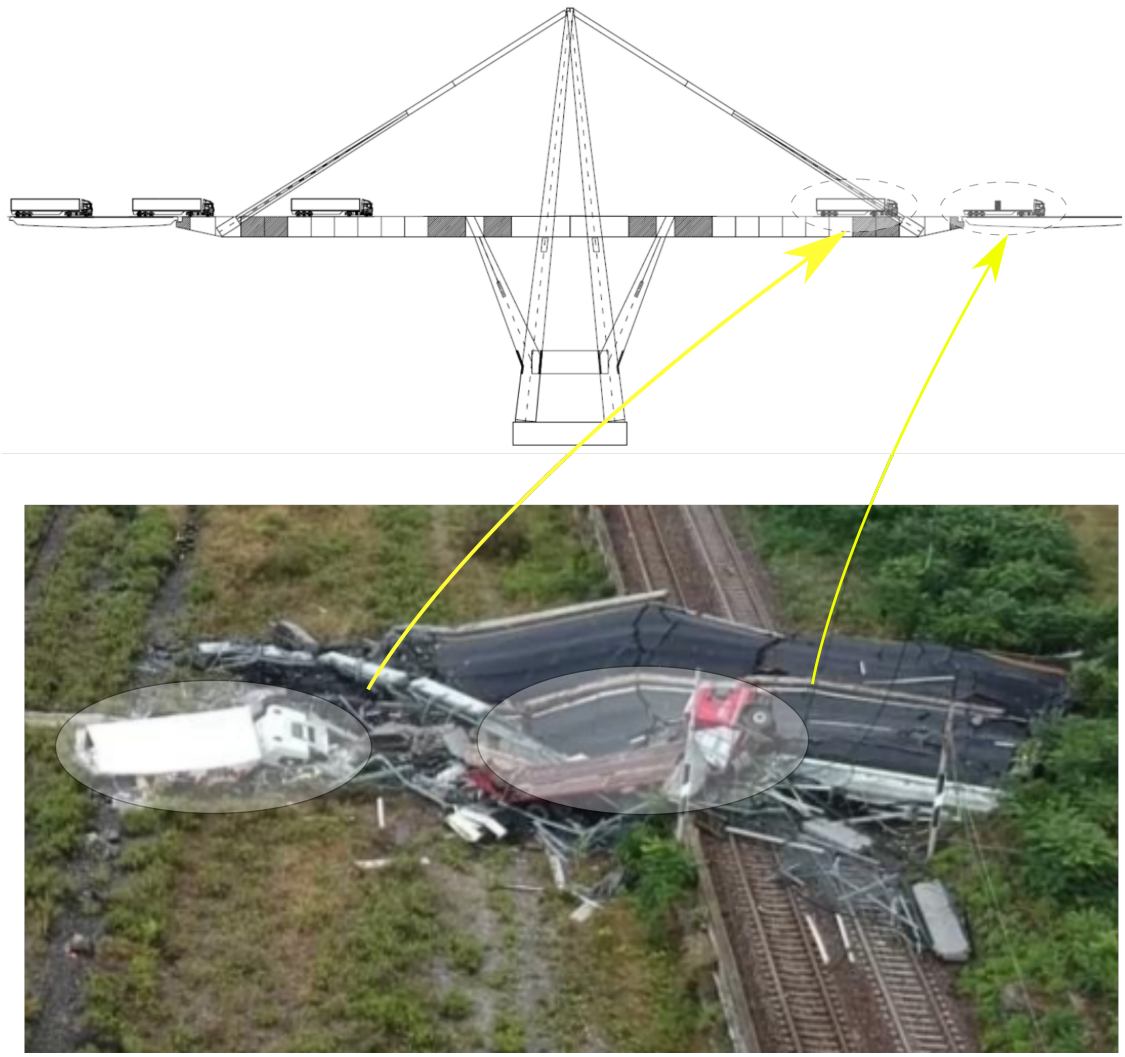

Figure 6.4: Hypothesized truck positions at time of Morandi Bridge collapse, based on collapse wreckage.

6.1.3 Post-Collapse Investigations

In analyzing the response of the Morandi Bridge to the load scenarios above, it is helpful to understand the changes wrought in the reinforced concrete elements of the Morandi Bridge throughout its 51 years in the harsh environment of Genoa.

Reported Corrosion Levels Much focus of post-collapse reports has been on the corrosion levels of the stay reinforcement. Filetto et al. [Filetto and Lignana (2019)] reported that half of the tendons were corroded. Of those, 22 percent exhibited section reductions between 50 and 70% while the remaining corroded tendons were deteriorated slightly less, between 30 and 50%. Invernizzi [Invernizzi et al. (2019)] used this data to assume an effective reinforcement area reduction of 35% due to tendon corrosion. Another testing regime was performed by EMPA [Rosati et al. (2018)] that visually graded the corrosion levels of 17 samples on a 5-point damage scale. Of the 17 samples, 14 were assigned a damage level of 4 or 5. Two of the wire samples (both visually graded 4) were shown to have lost between 25 and 40% of cross-section due to corrosion. It is noteworthy that the deformed bars were generally reported to have little or no corrosion.

Construction Flaws Some of the reported damage may be a consequence of the bridge construction phase. Morandi desired a metal sleeve to extend along the entire length of secondary tendons to isolate the tendons from the concrete cover during tensioning; yet, the collapse debris showed evidence of a *bonded region*, in which the tendon sleeves were missing. The region extended for approximately two meters on either side of the saddle. Figure 6.5 shows a dashed line, below which the reinforcement is seen to be discolored due to bond with the concrete. This bond would have transferred post-tensioning forces from the secondary cables to the concrete during the stressing operation.

Figure 6.5: Post-collapse observations: (Left) presence of large interior void; (Right) discovery of missing tendon sleeves near the antenna, from [Rosati et al. (2018)]

Even where the sleeve existed, there were issues. The tendon ducts were specified to be injected after the tensioning operation using a precompression system that Morandi had patented. His system is described by Calvi et al. [Calvi et al. (2019)], who show that adequate injection of the ducts was unlikely and the tendons outside the bonded region were effectively unbonded along their length. The lack of grout injection can reduce both corrosion and fatigue performance. Aggravating the situation further, a large void was uncovered from the ruins of the southeast cable stay. The void, shown in Fig. 6.5, could have provided a pathway for corrosive agents to travel unimpeded along the length of the stay.

Other damage may stem from the bridge's construction timeline rather than from poor craftsmanship. Construction timelines for each of the three balanced systems have been compiled in internal reports based on original photos. Balanced system 9 was the last of the three to be constructed and had a much quicker construction time than balanced systems 10 and 11. Internal reports suggest that the tendon stressing operations of balanced system 9 were performed with much less concrete

curing time than in the other two systems. Excessive shrinkage restraint tension stresses may have formed in the concrete sheath of balanced system 9.

Peculiar design features may have also played a role in reducing the net compressive stress in the concrete sheath. The curved saddle geometry produced tendon friction losses, which are characterized by a reduction in post-tensioning force due to curvature in a post-tensioned member [Leonhardt (1964)]. Assuming typical friction and wobble coefficients, friction losses in the Morandi bridge stays could have been as high as 30% in the antenna region, where the saddles's net angle differential approached 30°. Morandi did not consider friction losses in his calculations for tendon stressing forces, and he would have overestimated the compression force applied to the concrete by the secondary tendons.

Creep restraint, friction losses, and the absence of post-tensioning sleeves combined to reduce the initial concrete compressive state in the stay. Morandi foresaw the consequences of a stay failure and designed the tendons to have large capacity reserves; the tendons could have easily supported the static weight of the structure without support from the concrete sheath. But crucially, concrete was required as a corrosion barrier and even concrete microcracks could have reduced the efficacy of the concrete's environmental protection [Collins and Mitchell (1991)]. To make matters worse, concrete cracking in the saddle region could have diverted some fatigue inducing traffic loads to be carried by the steel reinforcement. Fractographic imagery from the EMPA forensic analysis [Rosati et al. (2018)] indicates a fatigue-type failure of some individual wires. Figure 6.6 shows the fracture surface of a wire sample taken from the ruins of the southeast cable stay. The surface shows a half-crescent crack and a jagged fracture surface. The half-crescent shape is indicative of fatigue crack growth [Grandt (2004)].

Figure 6.6: Fracture surface of a wire from the SE stay showing fatigue damage, from [Rosati et al. (2018)]

The evidence uncovered in post-collapse investigations tells a story of corroded tendons, concrete tensile stresses, partially restrained viscous effects, and fatigue damage. An accurate analysis of the Morandi bridge should include the interdependency of these phenomena. Analysis of the cable stays is performed in Section 6.2 using the analytical approaches outlined in previous chapters. The results are validated with a finite element model.

6.2 Collapse Analysis of Cable Stays

Previous researchers [Malomo et al. (2020)] have replicated the collapse sequence and debris pattern of the Morandi Bridge using the Applied Element Method. Their results are based on the assumption that failure of the SE stay initiated the collapse. This section will evaluate the feasability of such a stay failure, based on uncovered

knowledge from the post-collapse investigations. A schematic of the cable stay reinforcement is shown in Fig. 6.7.

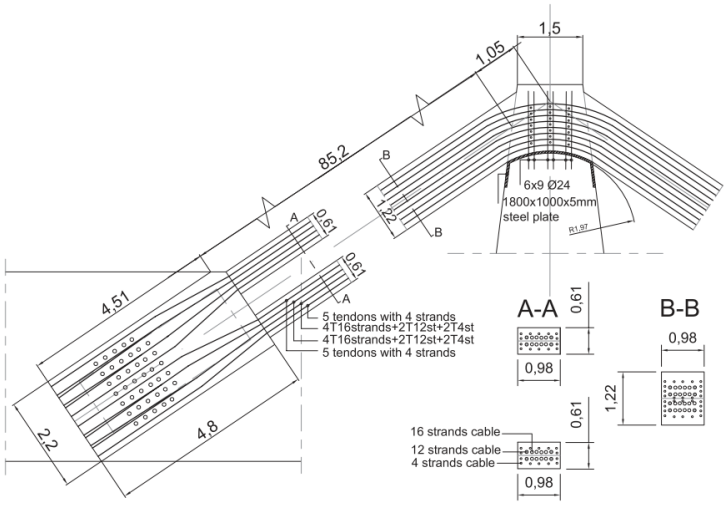

Figure 6.7: Details of Morandi Bridge cable-stay reinforcement

6.2.1 Static Analysis

Post-collapse reports showed strong evidence of corrosion in the stay reinforcement. This section aims to evaluate the effect of corrosion on the residual strength of the cable stay tendons throughout the lifetime of the Morandi Bridge. As discussed in Chapter 2, corrosion rates are highly sensitive; thus, a parametric study is undertaken in which the corrosion rate is varied. Some corrosion rates that correspond to similar corrosion levels to the reported values are shown in Table 6.2.

Table 6.2: Constant corrosion rates and corresponding corrosion area reductions

Corrosion Rate $[mm/yr]$	Primary Tendon Corrosion [%]	Secondary Tendon Corrosion [%]
0.035	13	22
0.05	20	35
0.07	25	42
0.08	30	50

The corrosion rate that replicates failure of the Morandi Bridge in 2018 (in the absence of exceptional loads) is termed the 'critical corrosion rate'. To evaluate the effects of corrosion levels on the cable-stay health, a 2D finite element model of the stays is built and analyzed. Then, the FEM results are verified with the approximate tools developed in Chapter 2. Both the numerical and analytical approaches assume an immediate corrosion onset, based on the results of a finite element model in Fig. 6.8 that suggest the formation of microcracks in the stay from the prestressing operation.

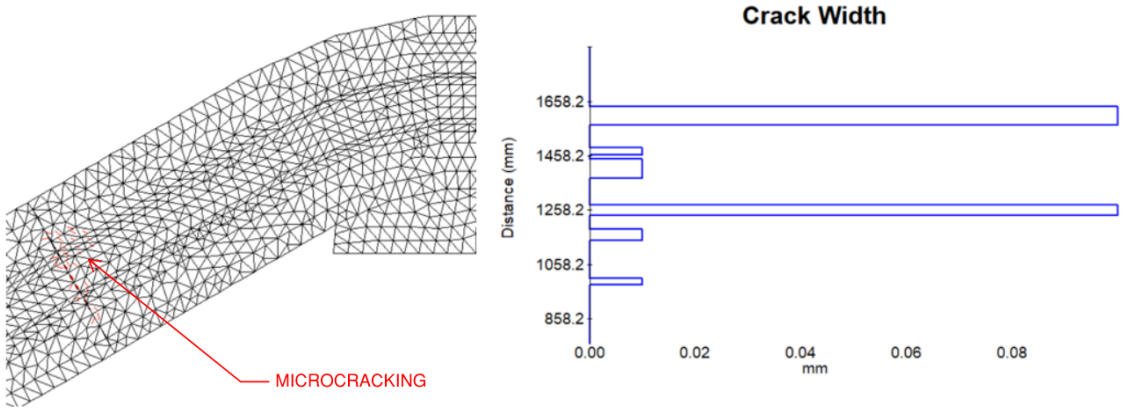

Figure 6.8: Microcracking in the Morandi Bridge cable stay after the tensioning operation

VecTor2 Model

The response of the Morandi Bridge cable stays to corrosion is analyzed by the VecTor2 software, a two-dimensional nonlinear finite element program for the analysis of reinforced concrete structures. Details of the finite element implementation can be found in the software manual [Wong et al. (2013)].

With inputs for specimen age and corrosion rate, VecTor2 implements models for both uniform and pitting corrosion. When uniform corrosion is modeled, VecTor2

also considers concrete cover cracking and bond reduction due to the formation of an expansive rust product. For pitting corrosion, VecTor2 calculates yield strength reduction, ultimate strength reduction and ultimate strain reduction according to Eqs. (2.3)-(2.5), using Du's experimental coefficients from Table 2.1.

VecTor2 also has sequential analysis tools that can capture a structure's temporal response to changing demand, concrete shrinkage, and increasing corrosion levels [Wong et al. (2013)]. The current implementation of the VecTor software uses a user-defined creep coefficient to soften the concrete modulus and update the concrete cracking strain, but does not calculate creep restraint due to composite action betweeen concrete and bonded reinforcement. Creep prestrains can be manually applied to concrete elements. For this analysis, a creep coefficient of 1 is used, calculated from the analytical procedure outlined in Chapter 2.

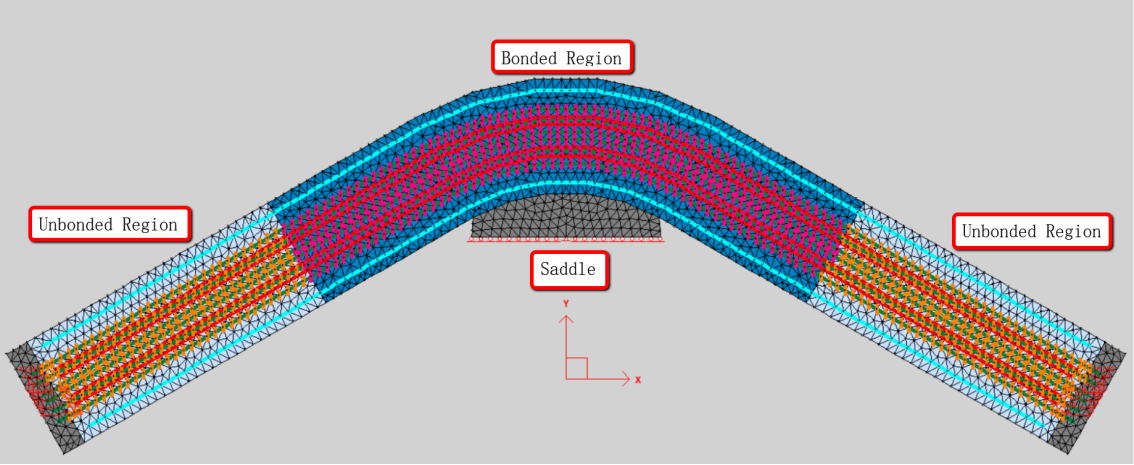

Figure 6.9: VecTor2 model of Morandi Bridge stay and antenna failure region

Admittedly, the cable stay is a three-dimensional member with slight through-thickness variation. However, preliminary analysis of both two and three-dimensional models (VecTor2 and VecTor3) showed no differences in phenomenological behavior.

So, for computational reasons, VecTor2 is used to model the critical section of the Morandi bridge cable stays.

The VecTor2 model, Fig.6.9, includes the susceptible *bonded region* and 2.5 additional meters extending into the *unbonded* region. The *saddle* is modeled to capture the interaction between the stays and the antenna. Stiff caps at the model's edges distribute high local stresses at the points of load application. Concrete is modeled with 4800 triangular elements. Deformed bars, A_d = 7540 mm^2, are modeled with truss elements and shear reinforcement is smeared. Primary cables, A_p=32700 mm^2, and secondary cables, A_s=10404 mm^2, are modeled with 1575 corroded reinforcing steel elements. The construction phase is implemented via a strain-offset in the primary cables (per the discussion from Section 6.1.1), demonstrated in Fig. 6.10.

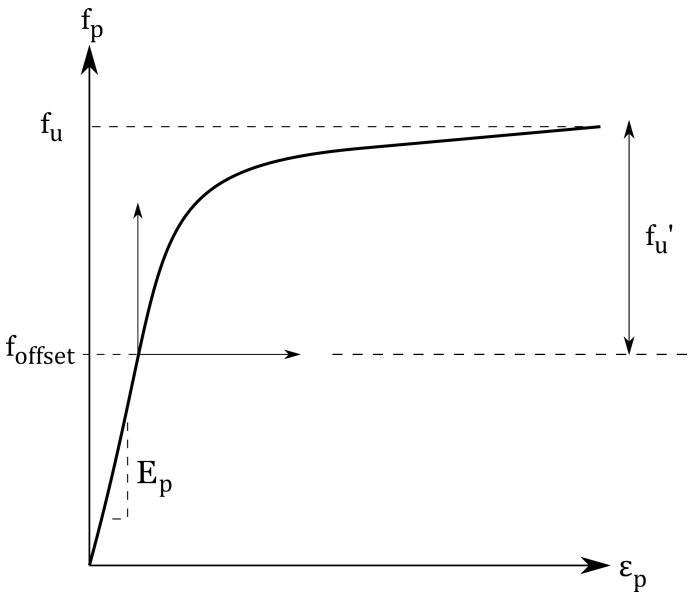

Figure 6.10: Strain offset of primary cable-stay tendons due to construction loads

Next, the secondary tendons are stressed by applying a prestrain of 3.5me. The post-collapse reports — [Filetto and Lignana (2019); Invernizzi et al. (2019); Rosati et al. (2018)] inform this phase, for which bond is modeled as link elements between

tendons and concrete in the *bonded region*. In the final phase — grouting and load application — the grout is assumed to be ineffectual based on the discussion by Calvi et al. [Calvi et al. (2019)]. Hence, the loads are directly applied to the model after the prestressing operation is performed.

All prestressing tendons are assumed to be corroded. Selected material models within VecTor2 are shown in Table 6.3.

Table 6.3: VecTor2 Material Models

Concrete Models			
Compression Pre-Peak	Hognestad	Confined Strength	Kupfer/Richart
Compression Post-Peak	Park Kent	Crack Slip	Walraven
Compression Softening	Vecchio 1992	Cracking Criterion	Mohr-Coulomb
Tension Stiffening	Collins-Mitchell 1987	Tension Softening	Bilinear
Reinforcement Models			
Concrete Bond	Eligehausen	Tendon Stress-Strain	Menegotto-Pinto

Results

Analysis results are presented in Fig. 6.11 for various corrosion rates. Each corrosion rate can be linked with corrosion levels from Table 6.2. Figure 6.11 plots primary and secondary tendon stresses throughout time, normalizing stress by the ultimate capacity, which varies according to Eq. (2.4) based on the corrosion level, η.

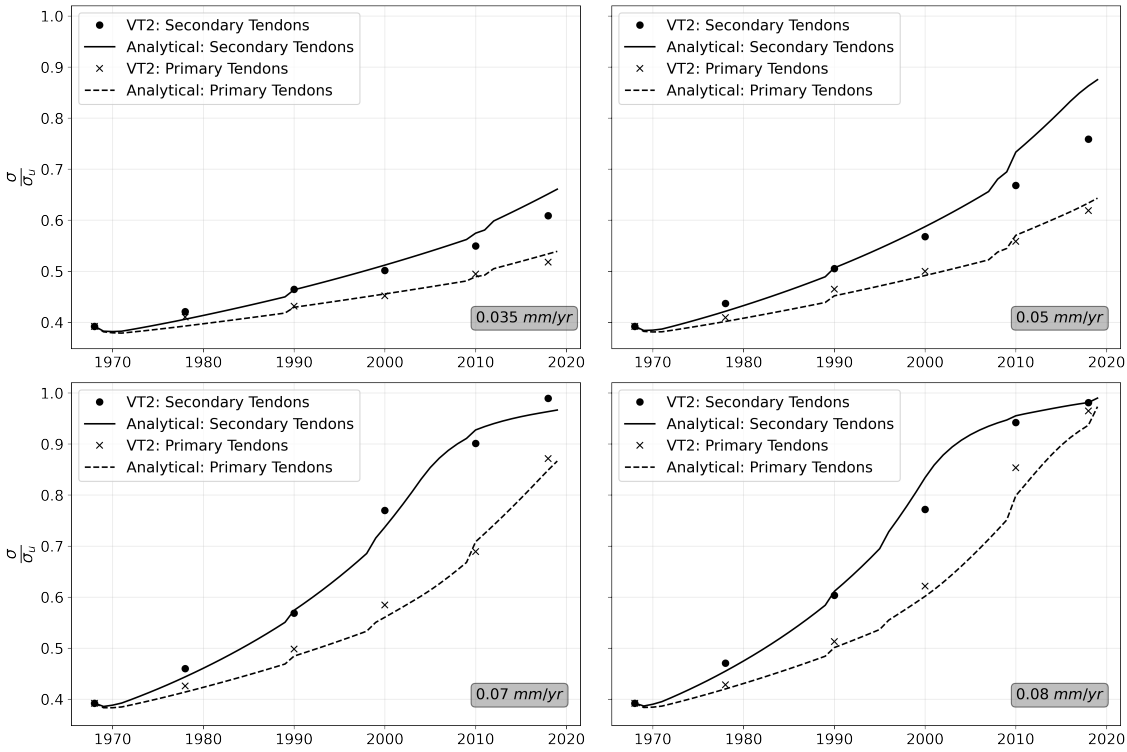

Figure 6.11: Comparison of tendon stresses between VecTor2 model and simple analytical scheme for various corrosion rates

For comparison, the VecTor2 results are overlayed on the analytical results. There is a convincing match between the two sets of results. Both models show higher damage in the secondary tendons than the primary tendons; corrosion — constant penetration rate — reduces the area faster in the smaller diameter secondary tendons which causes the mechanical properties to diminish more rapidly. It is also interesting to observe the effect of the additional permanent roadway loads in 1990 and 2010 (Table 6.1), which seem to affect the secondary tendons for low corrosion rates but the primary tendons for high corrosion rates. This can be explained by yielding of the secondary tendons by 2010, indicated by a flattening of the stress curve in Fig. 6.11 for high corrosion rates. After secondary tendon yielding, the primary tendons must absorb most of the additional loads. At the critical moment,

the secondary tendons have already yielded and the primary tendons exhibit reduced ductility from the effect of pitting corrosion, producing conditions that would result in a brittle failure, as was observed during the actual failure of the Morandi Bridge. Though the secondary tendons are predicted to have yielded before 2018, the ensuing deflection of the stay would have been minimal, given that the area of the secondary tendons was small relative to the primary tendons and the concrete exterior sheath.

Stresses from the VecTor2 model are generally lower than the analytical results after 2010. The most plausible explanation of these results is that the analytical method fails to capture the interaction between the bonded and unbonded concrete, and predicts concrete cracking to occur earlier than VecTor2 predicts. In the VecTor2 model, pretensioning loads are transmitted to the concrete in the bonded region, which would naturally extend to accommodate this load. However, extension of the bonded concrete is partially restrained by the adjacent unbonded concrete. This interaction compresses the unbonded concrete region. Thus, the onset of tensile cracking is delayed in the VecTor2 formulation. Despite minor differences between the numerical and analytical approach, the match between results is strong. Both methods predict failure of the cable stays in 2018 for the *critical corrosion rate* of 0.08 mm/yr, which corresponds to a 50% section loss of the secondary tendons and a 30% section loss of the primary tendons. It is reiterated that extreme loading events are not considered.

The sensitivities inherent in this analysis should be emphasized. The Du [Du et al. (2007)] model, Eqs. (2.3)-(2.5), for degradation of reinforcement mechanical properties is built into the VecTor2 results (Fig. 6.11). However, various alternatives exist [Morinaga (1996); Lee and Cho (2009); Cairns et al. (2005)] as shown in Table

2.1. Figure 6.12 explores the sensitivity of the critical corrosion levels to different pitting damage formulations. The reinforcement area reductions that are required to cause failure of the stay in 2018 are shown in the figure for five different damage formulations. The corrosion levels shown for Du's formulation correspond to the 0.08 mm/yr rate, which is plotted in Fig. 6.11. The formulation labeled *None* does not reduce the mechanical properties of reinforcement due to pitting corrosion. Though the tendon corrosion levels required for stay failure are much higher for the *None* formulation than the others, it should be noted that multiple researchers have proposed this formulation [Cairns et al. (2005)].

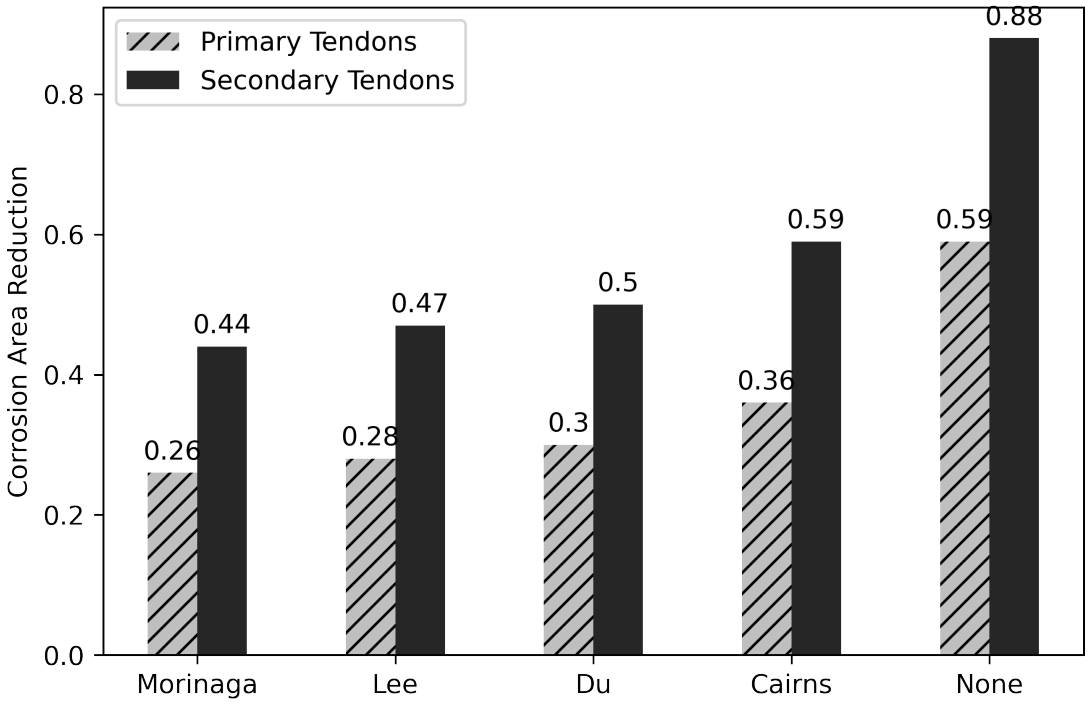

Figure 6.12: Comparison of pitting damage formulations on critical tendon corrosion levels required for stay failure in 2018

In general, the critical corrosion levels from the static analysis are higher than the reported (average) corrosion levels from post-collapse investigations, suggesting that

other factors may have been at play in the collapse of a stay.

6.2.2 Fatigue Analysis

Ignoring reinforcement fatigue damage in Section 6.2.1 may have been an over-simplification, given the presence of conditions that produced tension strains in the concrete sheath as well as fractographic imagery (Fig. 6.6) suggesting a fatigue-type tendon failure. Had the concrete sheath cracked, more cyclic traffic load would have been carried by the tendons and reinforcement fatigue cracks might have propagated. This section extends the previous results by coupling corrosion damage with fatigue loads from heavy truck traffic. The two fatigue methodologies of Chapter 3 are used in conjunction with experimental results from the literature to link corrosion levels with fatigue parameters. Once this connection has been made, the corrosion-fatigue life of the Morandi Bridge cables stays can be predicted. The FE software used in Section 6.2.1 is foregone because it does not couple the effects of corrosion and fatigue. Specifically, the VecTor suite does not consider that a corrosion pit may be the initiation site for a fatigue crack.

As implemented here, both analytical methods (S-N analysis and LEFM) rely on moving load analysis by Morgese [Morgese et al. (2019)], who assumed a linear increase in average truck loads from 120 kN in 1967 to 535 kN in 2018. The truck loads are based on traffic composition of various truck types. Morgese also presents data for the average daily truck traffic (ADTT) over the Morandi bridge for each year between 1967 and 2018. The ADT data is duplicated in Fig. 6.13.

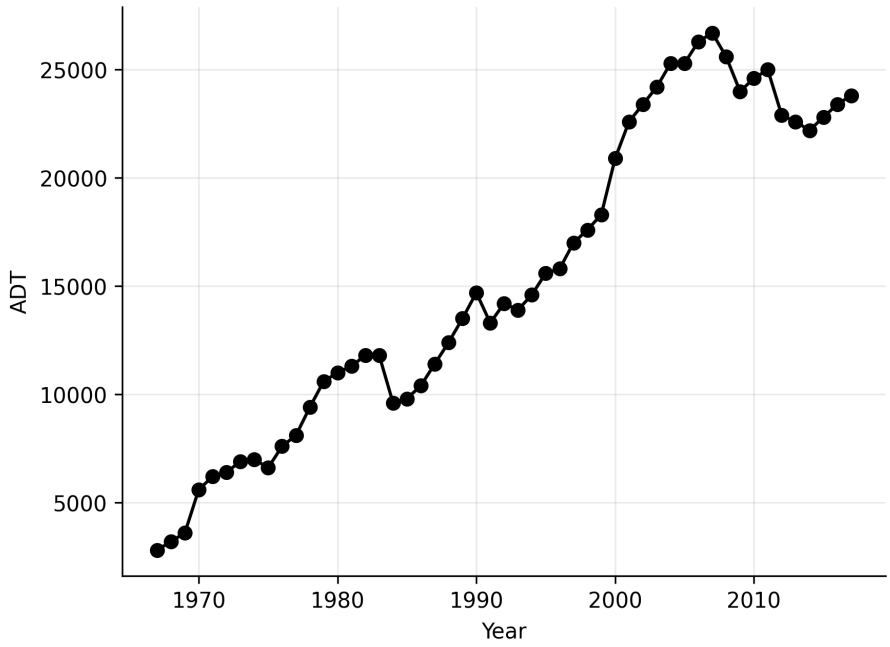

Figure 6.13: Average daily truck traffic throughout the life of the Morandi Bridge

Also common to both analytical models are the following assumptions about fatigue loads:

- The variable amplitude fatigue loading of the Morandi bridge can be estimated as blocks of constant amplitude loads, where each block lasts for a year.
- The full weight of a truck is borne by a single stay, which is inclined at 30° from the horizontal deck.
- The concrete sheath cracks upon application of truck loads and carries no tension at the crack.
- Uniform corrosion reduces the cross-section of tendons at a constant rate. Deformed bars are not corroded.
- Pitting corrosion causes stress concentration factors as proposed by Zhu et al. [Zhu et al. (2015)] for round pits.

$$\gamma_r = 1.045 + 0.000335t \tag{6.1}$$

Alternating stress values are calculated from the Morgese's loading information and the above assumptions. Sample alternating stresses on the tendons of a single stay are shown in Table 6.4 for a corrosion rate of 0.035 mm/yr.

Table 6.4: Alternating stresses in tendons throughout service life for a corrosion rate of 0.035 mm/yr

year	1968	1978	1988	1998	2008	2018
Alternating Stress [MPa]	4.95	8.57	12.40	16.45	20.71	25.18

Fatigue Predictions The corrosion-fatigue analyses are performed for increasing corrosion levels to study the effect of corrosion-fatigue on the tendon lifetimes. The critical corrosion rate that produces fatigue failure of the tendons in 2018 can be compared with the results from the static load analysis to determine the effect of fatigue on the deterioration of the cable stays. The critical corrosion rate for the S-N-η analysis is calculated as 0.03 mm/yr, which corresponds to 20% corrosion in the secondary tendons. The damage evolution results of the S-N-η analysis are shown for the critical corrosion rate as a semi-log plot in Fig. 6.14, which plots the variation of the tendons' damage parameter— Eq. (3.1) —in time. The tendons fail when the damage parameter exceeds 1.

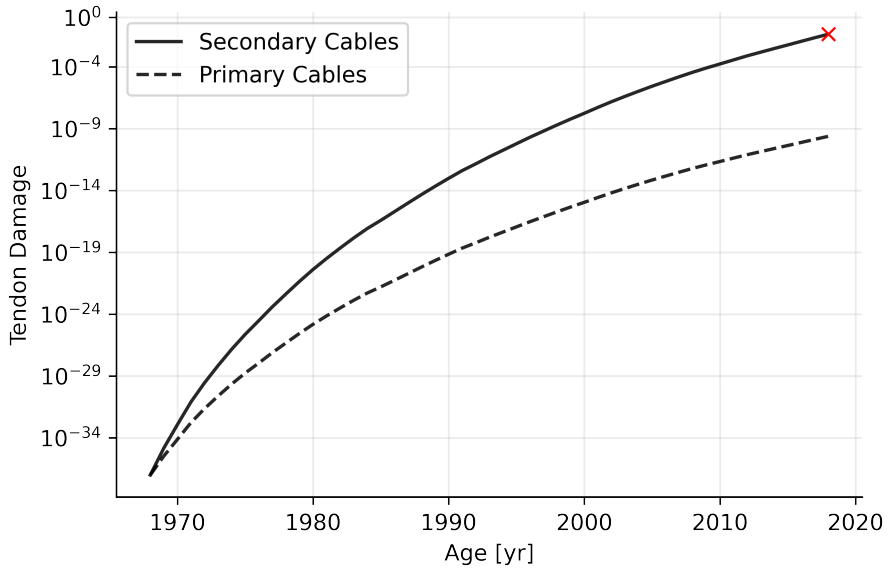

Figure 6.14: Predicted fatigue damage accumulation for Morandi Bridge stay tendons using the S-N method, conditioned for failure in 2018 in absence of extreme loads

Just as for static loads, the secondary tendons are predicted to accumulate damage more quickly than the primary tendons. Yet, it is clear from Fig. 6.14 that the additional roadway dead loads of 1990 and 2010 are not captured by the S-N-η approach, which only considers the effect of the cyclic live loads on the specimen fatigue life. Jiang's fatigue-life surfaces could be augmented to consider mean stress effects (i.e., permanent loads) [Forman et al. (1967)], but here it is sufficient to consider the static load results from Section 6.2.1. Figure 6.11 indicates that yielding of the secondary tendons is accompanied by rapid stress accumulation in the primary tendons. Additionally, Eq. (2.5) indicates a reduced plastic capacity of corroded reinforcement. Therefore, it is assumed here that failure of the secondary tendons precipitates failure of the entire stay. The sudden nature of the collapse [Hasenjager (2019)] supports this assumption.

The S-N-η approach does not lend itself well to a parametric study of the corro-

sion parameter because Jiang's experimental surface was limited to corrosion levels below 20%. However, the LEFM fatigue crack growth method is not limited by the same data. Rather, the fatigue crack growth method is capable of predicting the evolution of fatigue cracks for a wide range of corrosion levels. The crack sizes for *individual wires* are predicted based on the procedure outlined in Section 3.3.2. If the stress intensity at a time step, t_i, does not exceed the fracture toughness, the fatigue crack size, a_i, is updated via Eq. (3.9) to obtain the new, larger crack size, a_{i+1}. Alternating stresses and corrosion levels are calculated for the next time step. The stress intensity range, ΔK_{i+1}, is then calculated from Eq. (3.2), using the maximum of $a_{EIFS_{i+1}}$ and a_{i+1}. The process is repeated until the fracture toughness is exceeded, at which time the wire is predicted to fail. The procedure is shown graphically in Fig. 6.15.

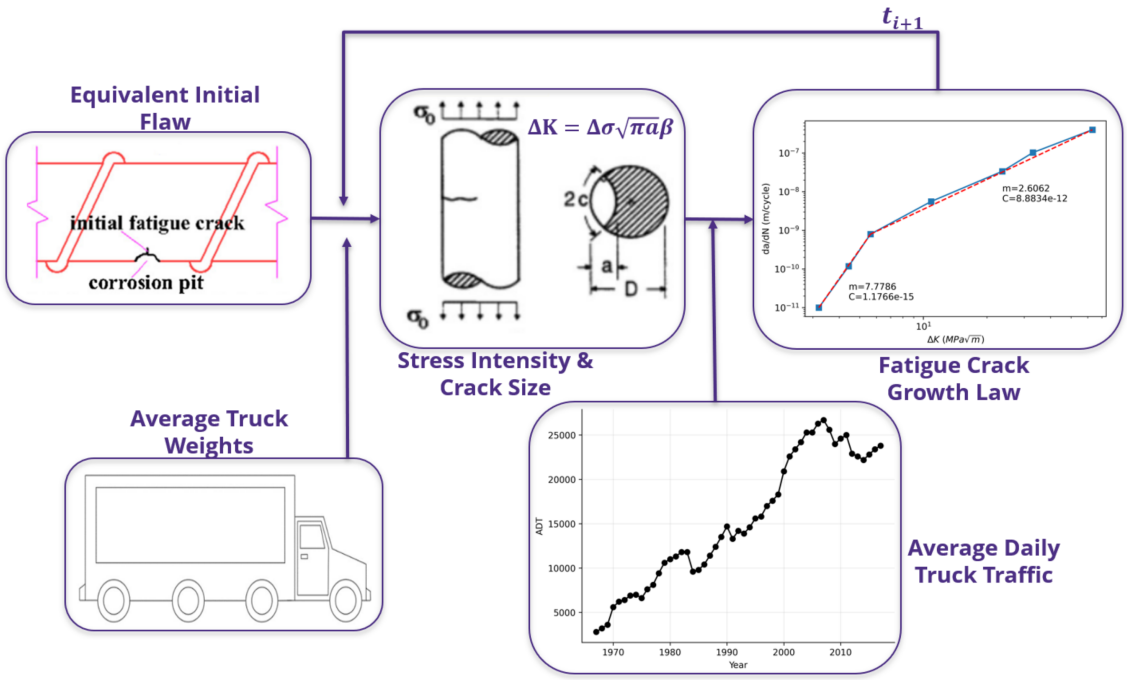

Figure 6.15: Analytical scheme for the prediction of damage in the Morandi Bridge tendons due to the combined effect of corrosion and fatigue

Calculated crack sizes are compared with the critical crack sizes that correspond to fatigue fracture. These two curves are overlayed in Fig. 6.16a for various corrosion rates. Tendon wire fatigue cracks are plotted as solid lines and critical crack sizes are plotted as dashed lines.

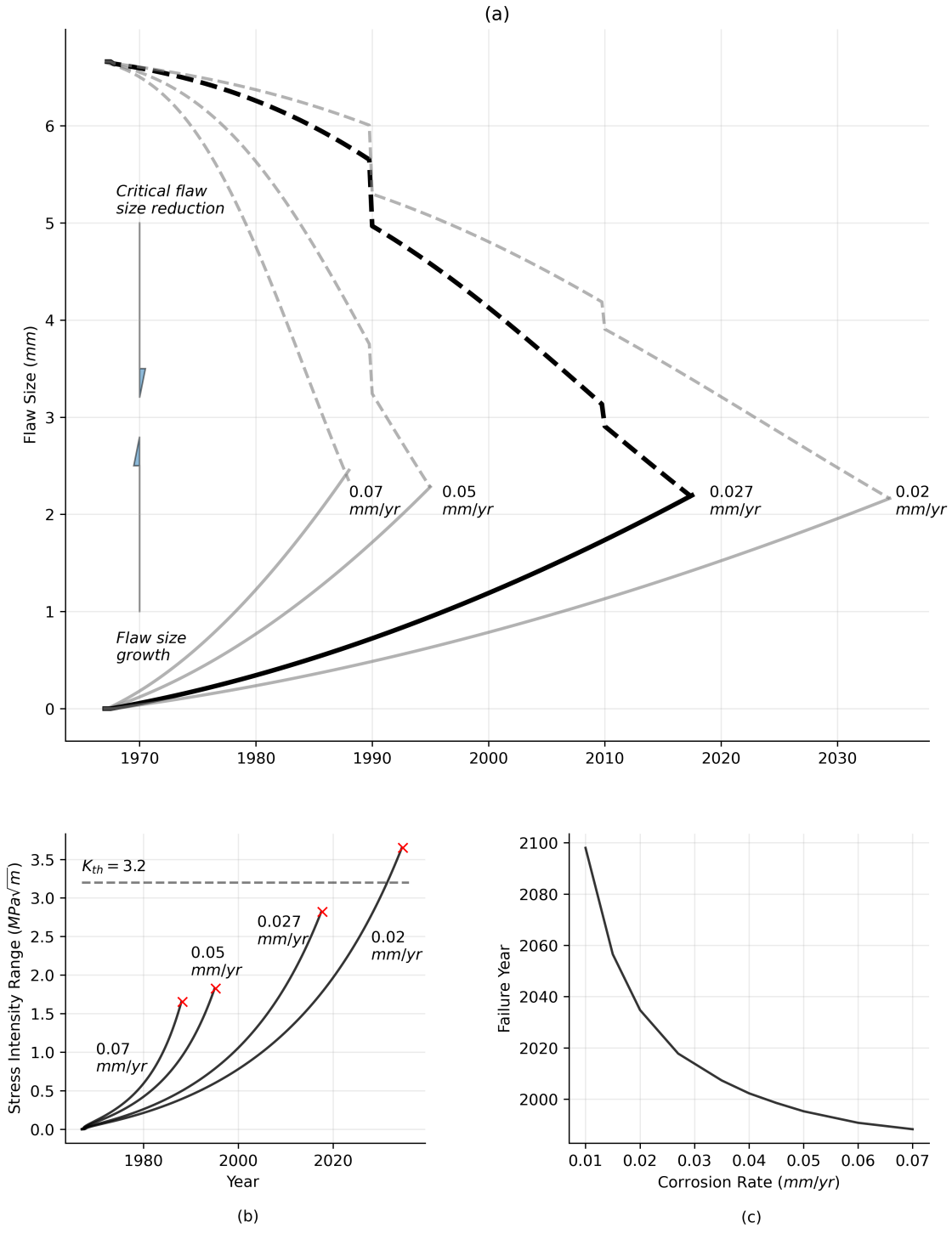

Figure 6.16: Predicted fatigue damage accumulation for Morandi Bridge stay tendons using the fracture mechanics method showing (a) fatigue flaw size growth (solid) and critical flaw size growth (dashed) for individual 7mm wires; (b) stress intensity ranges exist below the stress intensity threshold for most corrosion rates considered; (c) failure year prediction for various corrosion rates based on fatigue crack growth methodology

Notably, the critical flaw size curve accounts for the additional roadway loads of 1990 and 2010, as indicated by the sudden 'jumps' in Fig. 6.16. The intersection of the solid and dashed lines represents the instant the crack stops growing and the section ruptures. This condition corresponds to a fracture surface transition from smooth to jagged (see Fig. 6.6). The bold curve in Fig. 6.16a represents the critical corrosion rate of 0.027 mm/yr (19% corrosion in the secondary tendons) for which the wires would fail in 2018. However, it is important to consider the influence of corrosion levels on the crack growth results; the possibility existed for local variations in corrosion. For instance, the large void discussed in Section 6.1.3 could have favored highly localized corrosion rates. Additionally, the corrosion levels within any given tendon surely varied, given the different levels of exposure for the central wire and the outer wires. An example of this phenomenon is shown in Fig. 6.17, which shows the corrosion levels of a single tendon pulled from the remains of the Morandi Bridge cable stay. The results presented in Fig. 6.16a do not account for the variation of corrosion levels between wires, so the critical corrosion rate of 0.027 mm/yr should be extended with caution when discussing global collapse of the Morandi Bridge cable stay.

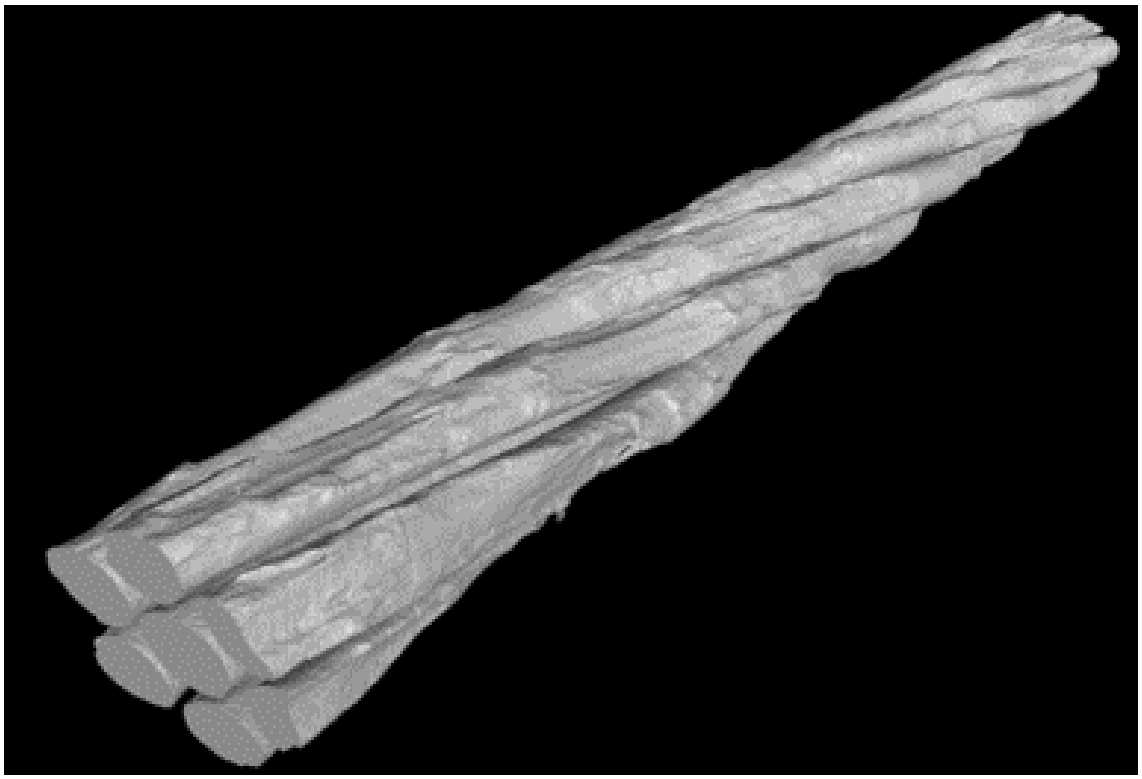

Figure 6.17: Scanned corrosion of a section of tendon from the Morandi Bridge cable stays, copied from [Rosati et al. (2018)]

Variation of the fatigue life with corrosion rate is shown in Fig. 6.16c, where the range of reported corrosion rates is shown. Highly corroded wires are predicted to fail as early as 1990 while mildly corroded wires would have had reserve capacity at the time of the Morandi Bridge collapse in 2018. A final key insight into fatigue of the wires is gleaned from Fig. 6.16b, which plots the stress intensity range evolution for various corrosion rates. The dashed horizontal line indicates the stress intensity threshold for crack growth. It is noteworthy that the threshold is not exceeded for most of the considered corrosion rates, signifying that the alternating stresses were not high enough to propagate fatigue cracks. All crack growth in Fig. 6.16a, then, comes from pitting cavity growth. This indicates that corrosion control is essential for fatigue damage mitigation.

In summary, the two corrosion-fatigue predictions are consistent in predicting a critical corrosion rate near 0.03 mm/yr for failure of the cable stay reinforcement, if extreme loads are neglected. These fatigue methods predict faster damage accumulation than the static method, which predicted failure of the stay in 2018 for a corrosion rate of 0.08 mm/yr. Although the cable stay crack patterns may have favored fatigue load concentrations on the stay reinforcement, a comparison of fatigue results (20% critical corrosion levels in the secondary tendons) with observed corrosion levels (25-40%) suggests that fatigue may have been less significant than assumed here.

6.3 Collapse Analysis of Main Deck

The results of Section 6.2 suggest possible failure of the cable stay tendons due to the combined effects of corrosion and fatigue. If this failure mechanism is to remain plausible within the context of August 14, it must be shown to cause collapse of the main deck, as observed in the actual collapse sequence [Hasenjager (2019)]. An analysis of the deck rubble [Malomo et al. (2020)] shows that the southwest shear-ledge corner of the main deck was partially buried in the ground, while the transversely opposite corner (northwest) was exposed, suggesting a torsional collapse mode. In this section, a 3D finite element model of the main deck is built and a torsion analysis is performed. The results are then verified with the simplified combined load analysis method of Chapter 5.

6.3.1 VecTor3 Model

Analysis of torsion requires a 3D model. VecTor3 (VT3), the three-dimensional counterpart to VecTor2, is used here.

Deck Modeling Assumptions The following assumptions are implemented into the FEM model of the main deck:

- Deck reinforcement is assumed to be free from corrosion damage.
- The complex stressing sequence of deck tendons, temporary 'harp' reinforcement, and permanent cable-stay tendons is ignored in the VT3 models. Instead, the effective tendon stresses at the end of the construction phase are implemented, due to path-independence of any linear superposition of elastic stress states. Viscoelastic effects produced by the harp reinforcement are ignored.
- The main deck (Fig. 6.18) is modeled as prismatic, ignoring the taper of the cantilever spans. This assumption simplifies the model build process by eliminating the need to model the shear ledge and transverse beam geometry. These two components were not critical sections, as suggested by Malomo et. al.'s collapse modeling [Malomo et al. (2020)]. Additionally, post-collapse investigations revealed intact transverse beams. Therefore, the shear-ledge region (1.67m) and transverse beam regions are modeled as rigid strips to prevent premature failure in the model.

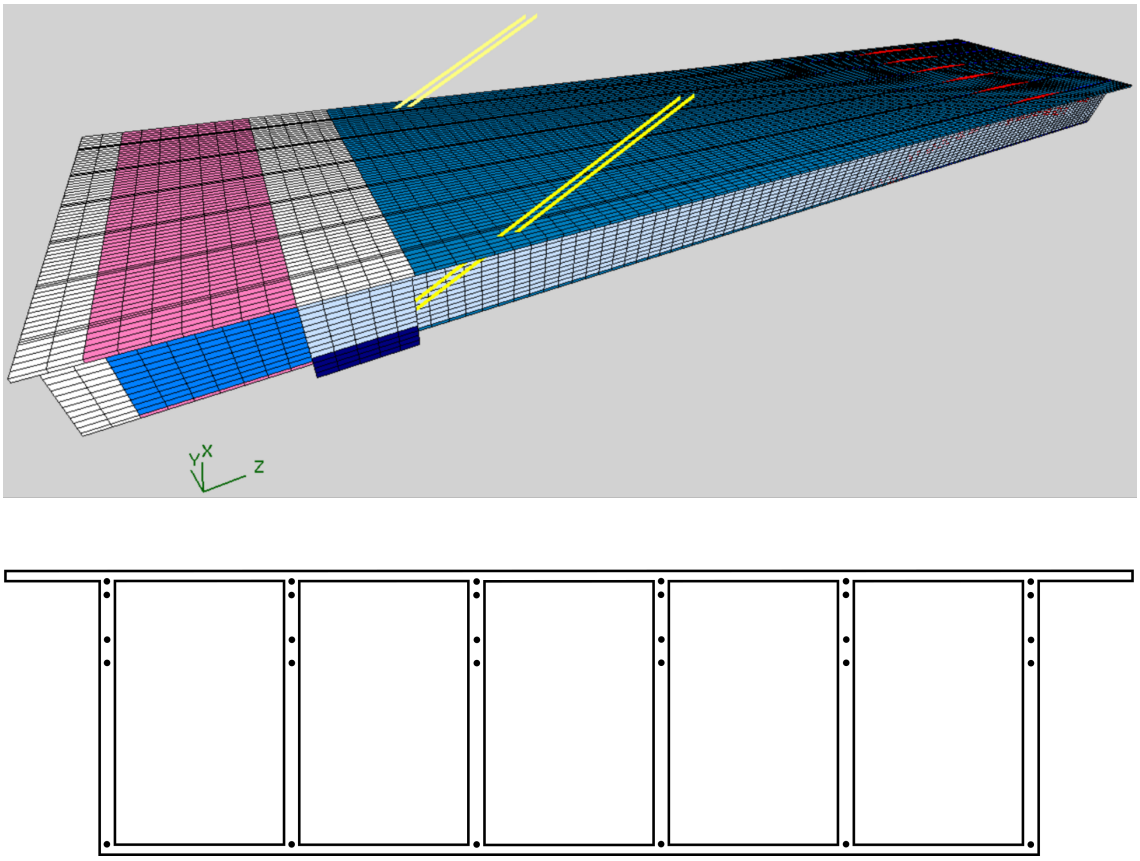

Figure 6.18: Idealization of the Morandi Bridge deck as prismatic

Deck Reinforcement The tendon layout in the main deck is shown in Fig. 6.19, as suggested in Orgnoni's thesis [Orgnoni (2019)].

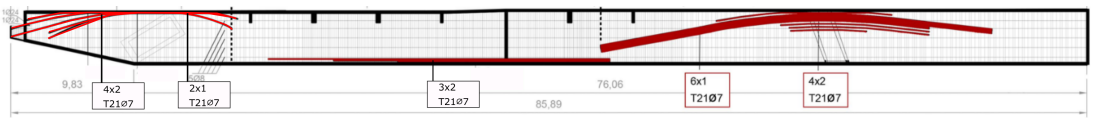

Figure 6.19: Layout of tendons in the main deck of the Morandi Bridge balanced systems

Boundary Conditions The connection between the deck and the stay is modeled with axial truss elements. These truss elements anchor into the abutting ends of the

main transverse beam, which are assigned high stiffness (dark blue in Fig. 6.18). Individual truss elements are modeled to represent the primary and secondary stay tendon groups, as well as the concrete cover. The pier support is modeled as a rigid pin. The line of symmetry in the middle of the main deck is modeled with a slider condition that restrains longitudinal displacement.

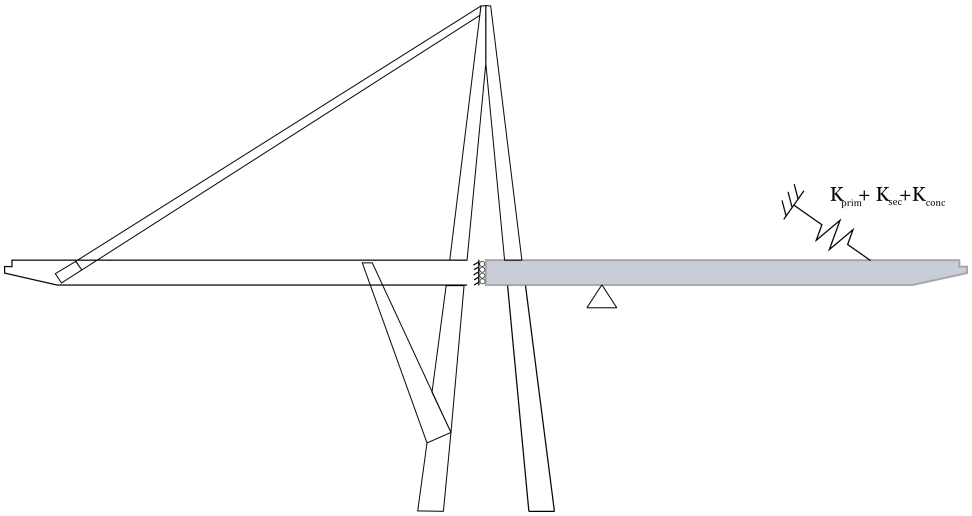

Figure 6.20: Schematic of deck boundary conditions, as modeled in VecTor3

Loads First, the construction phase is accounted for. Directly modeling this phase would require many assumptions (i.e., weight of transverse beams, effective force from stressed tendons in transverse beams, weight of simply-supported span). The modeling task is simplified by knowledge of the deck deflection and tendon stress condition upon completion of construction. Orgnoni [Orgnoni (2019)] clearly documents the tendon stressing stages and deck deflections throughout each step of construction. Since the control points were at +0 elevation after construction, the construction phase of the deck is implemented in VecTor3 by ignoring all construction loads and assigning strain-offsets (Fig. 6.10) to all tendon reinforcement according to Orgnoni's MidasCivil models. After modeling the construction phase, the secondary tendons and concrete cable elements are activated in the model. A

strain-offset is applied to the secondary tendons to simulate the precompression of the stay's concrete cover.

Service loads present at the time of collapse are now added to the model.

- Roadway barriers are modeled as nodal loads. A concentrated load of 975 kN is applied at the shear ledge from the contribution of the barriers from the simple-span.
- The loads from the roadway expansion of 2010 are modeled as nodal loads. From internal reports, the roadway loads provide 55% of the demand in the stays as the roadway barriers. This ratio is maintained here, with 540 kN of concentrated load at the shear ledge from the simple-span.
- Mobile traffic loads are applied based on Fig. 6.4.

Torsion Analysis Procedure The torsional response of the main deck due to the loss of a cable stay is simulated by gradually reducing the area of the SE stay elements. Such an analysis is performed for a set of models, each having a different effective tendon area in the SE stay. The torsional resistance and deck displacements from each model are then compiled into a torque-twist curve. This procedure is performed assuming that the surviving cable stay has uncorroded tendons; this is an unconservative scenario for which corrosion and fatigue do not damage the stay tendons.

Results The results are presented for the case of no corrosion damage in the remaining stay. Given the findings of the post-collapse investigations, this scenario is unlikely; however, the analysis allows the large-deformation torsional behavior of the deck to be investigated.

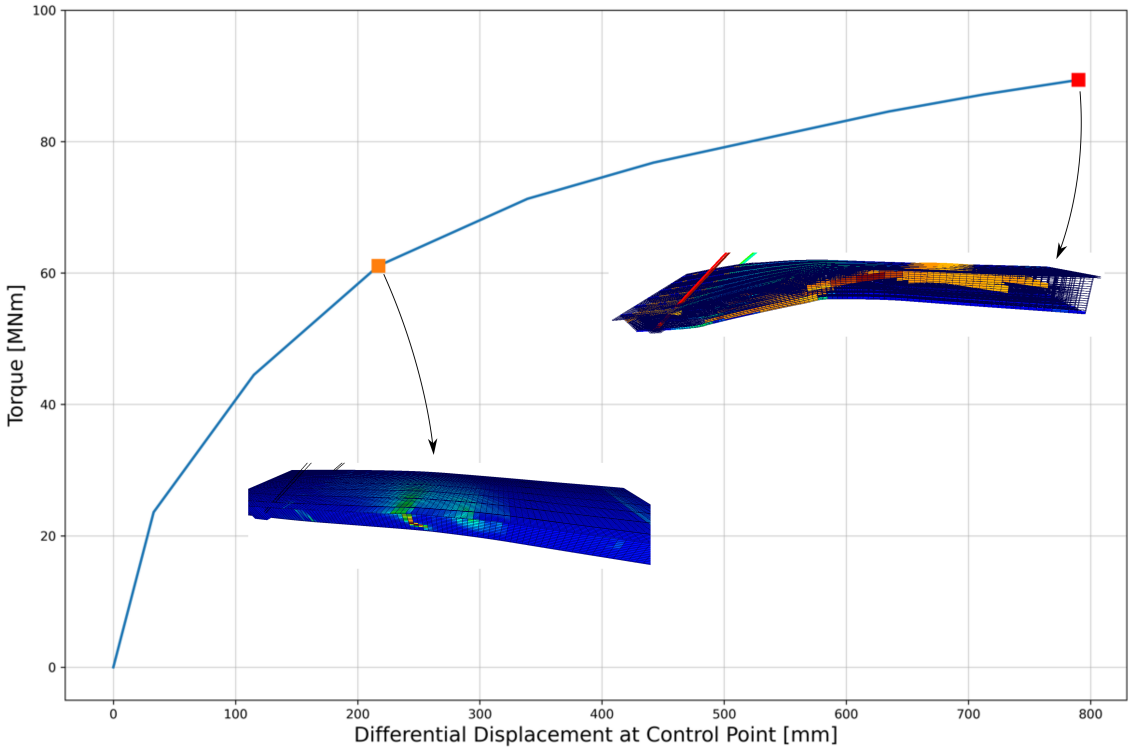

Figure 6.21: Torque-twist curve of Morandi Bridge deck

Upon 'releasing' the SE stay, the main deck torsional rigidity quickly softens and it is apparent that concrete damage accumulates in two regions, as shown in Fig. 6.22. Not coincidentally, both critical regions exist at the transitions from positive to negative tendon reinforcement (see Fig. 6.19 for tendon layout). In the transition region near the pier support there is only a 1m overlap between reinforcement, between which a highly disturbed local region appears. In the transition region near the stay support, tendon reinforcement is missing altogether.

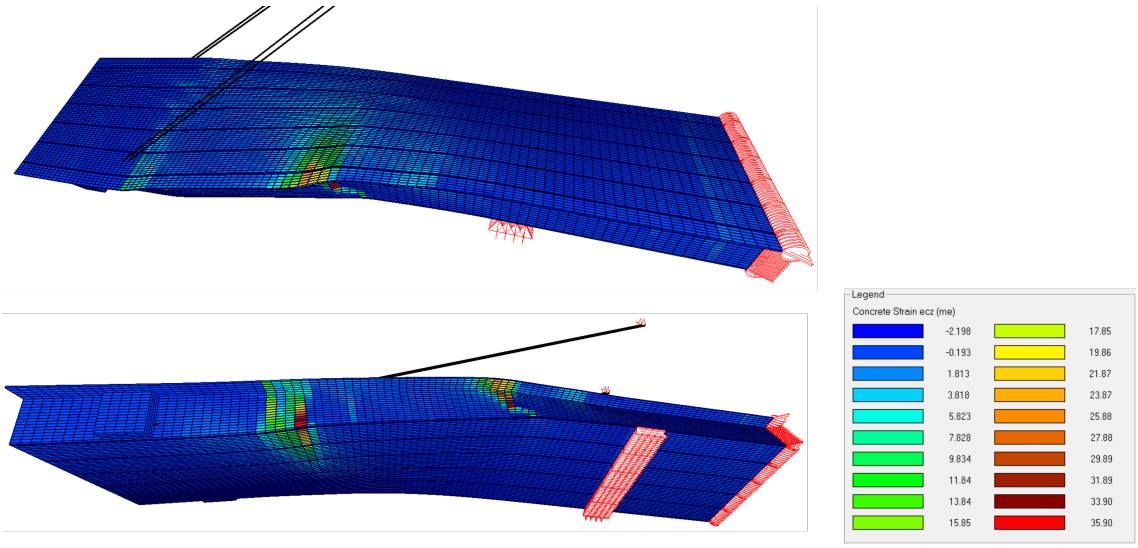

Figure 6.22: Longitudinal strains in main deck of Morandi Bridge upon loss of cable stay

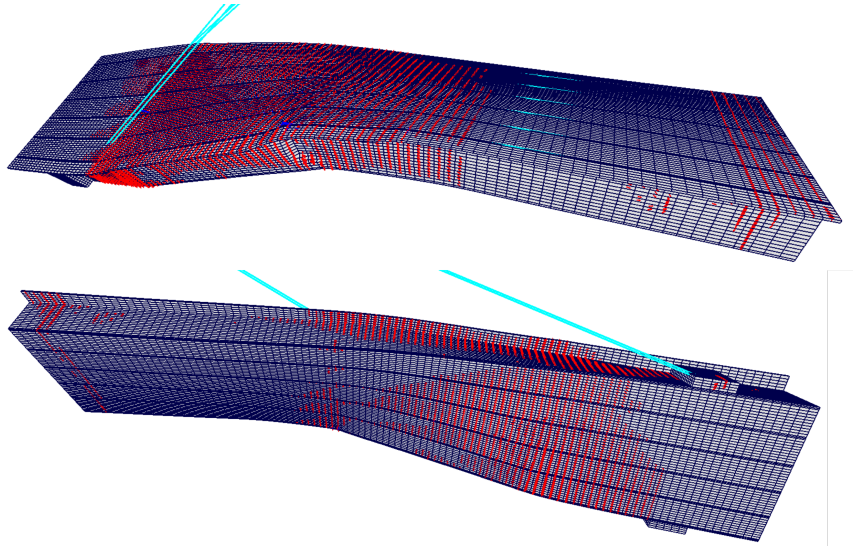

Figure 6.23: Crack pattern in main deck of Morandi Bridge upon loss of cable stay

The bridge design clearly relied on the horizontal component of the stay support to contribute a self-prestressing effect on the deck, which was 'essentially lacking longitudinal reinforcement', in the words of the designer. Unfortunately, the self-compressing reaction is lost once the SE stays fails. The balanced state of the

load-resisting system becomes compromised and tension forces dominate the stress-field of the deck, especially for the side-wall in which shear and torsional stresses align. The variation of tendon stresses through the deck width is visualized in Fig. 6.24, which shows the most extreme tendon stresses in the additive wall.

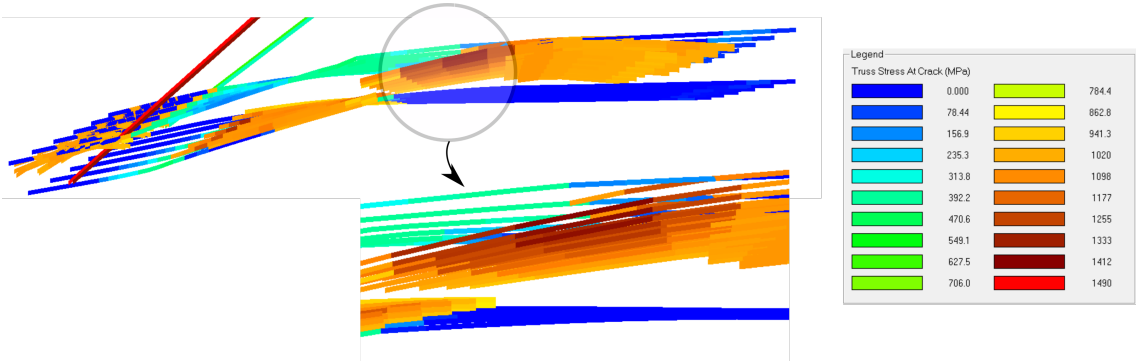

Figure 6.24: Tendon stresses at a crack in main deck of Morandi Bridge upon loss of a cable stay

At tendon yielding, the deck exhibits 90 MNm of torsional resistance. This capacity is well below the 175 MNm of torsional demand estimated by Calvi et al upon removal of one stay [Calvi et al. (2019)]. The demand calculations performed by Calvi et al. assume a constant twist rate, thereby producing a constant demand along the deck length (between stay support and pier support). An improved estimation for the torsional demand along the deck length is provided in Fig. 6.25. The non-constant torsion demand is calculated from a frame of linear beam elements, onto which the loading scenario of Section 6.1.2 is applied. Then the twist from the frame model is measured between adjacent cross-sections along the deck length, assuming that the torsional stiffness, GJ, linearly maps local twists to torques. Warping restraint is neglected near the pier support.

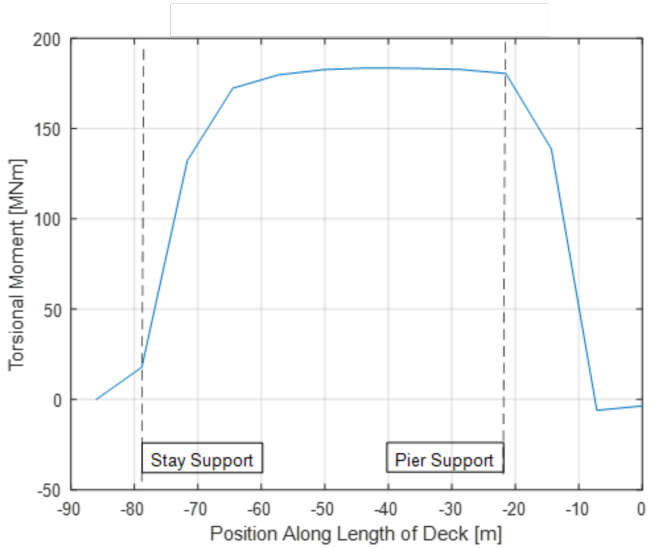

Figure 6.25: Torsion demand along length of Morandi Bridge deck upon loss of a cable stay

6.3.2 MCFT Combined Loading Tool

The 3D-FEM results from Section 6.3.1 provide the full load-displacement response for the Morandi Bridge main deck, assuming the loss of a cable stay. Stresses and strains for each elements are calculated and the full displaced shape is visualized. Such results are invaluable for the current analysis because the deck's deflected shape can be compared against the known collapse mode. However, setup of the 3D model is painstaking and computation times can be lengthy. If a detailed load-displacement response is not desired, a full finite-element implementation may be overkill. For example, the stay results suggest potential failure of the stay tendons from the combined action of corrosion and fatigue so here we may only need to check whether the deck's torsion capacity exceeds the torsion demand upon loss of a stay. If the demand exceeds the capacity, the deck will be predicted to fail and the stay failure proposed in Section 6.2 is validated as a likely failure mode.

The MCFT approaches for combined load analysis presented in Chapter 5 can be used to evaluate the torsion capacity of the Morandi Bridge deck. Since the deformation response is not required for this task, the simplest approach (modified MCFT tool) is used here.

Though simpler than the other truss models in Chapter 5, the MCFT simplified tool makes similar assumptions about the section geometry (Fig. 6.18), which is idealized as a single-cell box. Unlike the methods of Rabbat and Greene, the simplified tool does not redistribute the reinforcement throughout the section. Another conservative assumption is made by assuming the strain can be calculated at the level of tension reinforcement [Collins and Mitchell (1991)]. With this assumption, the strain in the tension reinforcement is calculated by recasting actions as effective strains, as shown in Eq. (5.15). Finally, the principal compressive strain directions are solved with the equations of Bentz's Simplified MCFT [Bentz et al. (2006)], which accurately approximate the CFT constituitive equations.

Using the simplified tool, the torsional capacity of the Morandi Bridge main deck is calculated at various points along the length. Each calculation point is chosen to correspond to a transition in the reinforcement layout. The calculations are performed using the moment and shear demands presented by Calvi et al. [Calvi et al. (2019)], copied in Fig. 6.26.

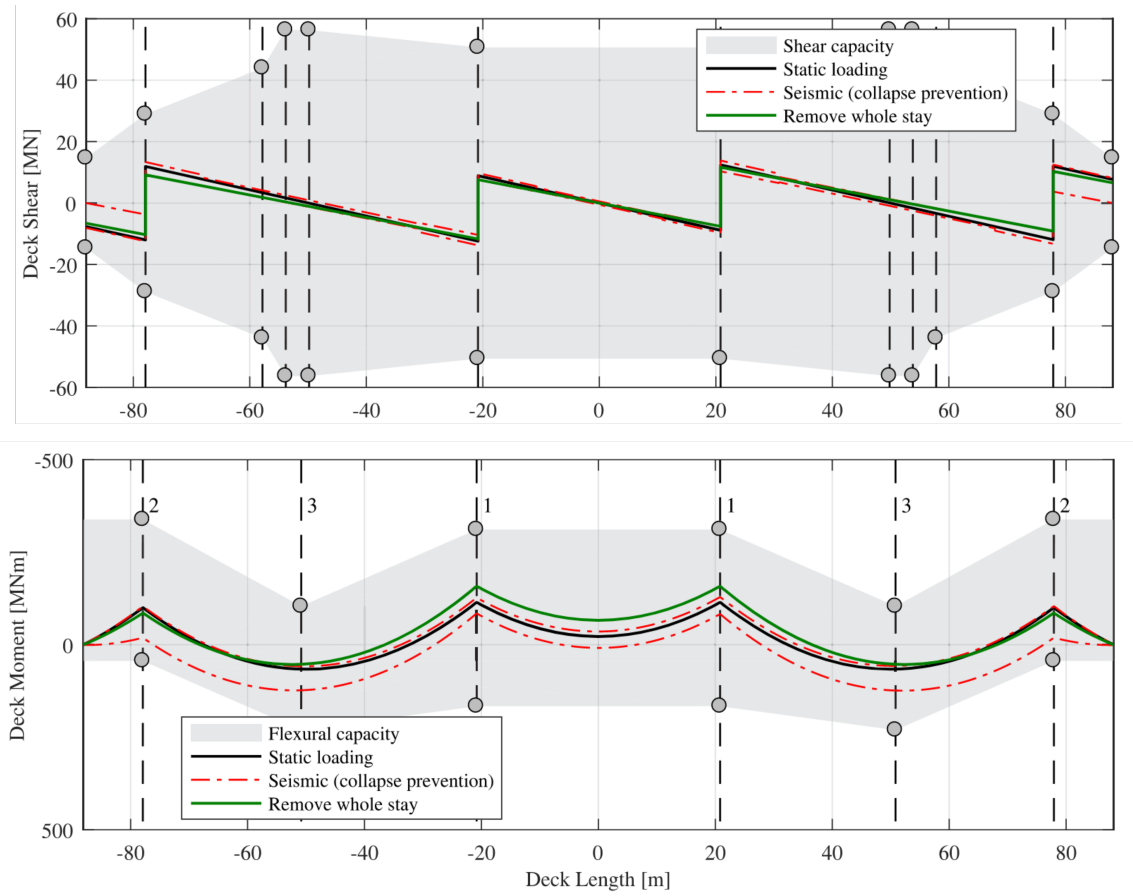

Figure 6.26: Shear and moment demand on Morandi Bridge deck upon loss of a stay, copied from [Calvi et al. (2019)]

Converged analysis results are presented in Fig. 6.27 for 10 locations on the south half of the main deck. The torsion demand (Fig. 6.25) is overlayed on the capacity results and the demand-capacity ratio (DCR) is plotted for each point. The deck is then predicted to fail at the point where the DCR most exceeds unity. Most of the cross-section (locations 2,3,5,6,7) is shown to have a DCR slightly exceeding one, while sections 4 and 8 display clear weaknesses, with a DCR of 1.5 and 2, respectively. These two sections correspond to the transitions between positive and negative moment reinforcement. Though the moment demand is small at both

sections 4 and 8, the tendon terminations provide an effective longitudinal force and moment at each section, which increases the longitudinal strain and reduces the torsion capacity.

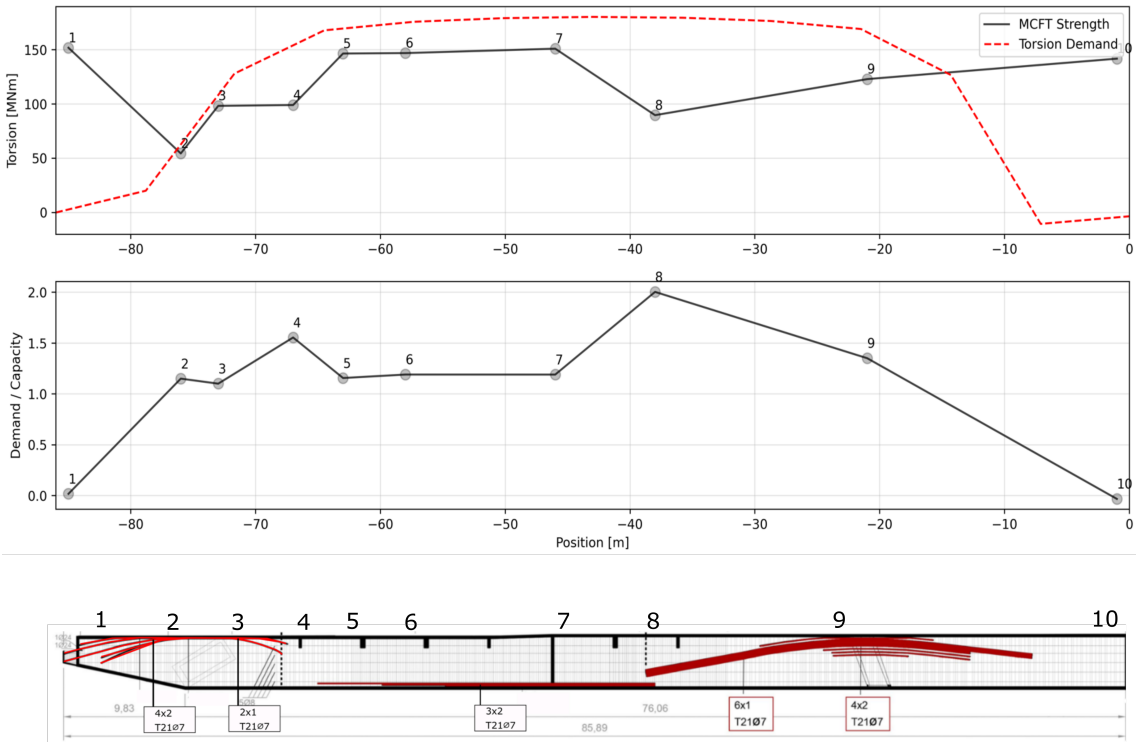

Figure 6.27: Torsion capacity and demand along length of Morandi Bridge deck

Comparing Fig. 6.27 with the VT3 results shows that the simplified tool predicts damage concentration in the same two regions as the VT3 model, with torsional failure initiating near the pier support in each model. Additionally, the simplified MCFT tool predicts a torsion capacity just below 100 MNm at section 8, which compares well with the peak torque of 90 MNm achieved in the VecTor3 model.

CHAPTER 7

CONCLUSIONS

7.1 Summary

Aging structures are at risk of environmental and fatigue damage, and they often exhibit minimal structural redundancy. This thesis reviewed simple analysis procedures for the evaluation of old structures, then performed a case study on the recently collapsed Morandi Bridge with the available tools. The following topics were addressed:

- Corrosion damage mechanisms were reviewed. A simple strain-based theory was presented that incorporated corrosion damage into traditional analysis of prestressed concrete members.
- Two traditional approaches for fatigue analysis were reviewed. Each was paired with experimental corrosion-fatigue data from the literature to develop approaches for combined corrosion-fatigue analysis.
- Truss model theory for the load-deformation response of beams subject to combined loads was reviewed. Compatibility equations from the Compression Field Theory were used in conjunction with equilibrium equations from the Modified Compression Field Theory. The truss model theory presented in this work is similar to the work done by others [Rahal and Collins (1995); Greene and Belarbi (2009); Rabbat and Collins (1978)] and was verified against various experiments from the literature for the case of combined shear and torsion. A simple model for the analysis of combined loads [Collins and Mitchell (1991)] was reviewed that captured the ultimate strength of a section subject to combined loads.

- A case study was presented in which the above tools were implemented. The corrosion and fatigue analysis tools were used to predict the cause of collapse for the Morandi Bridge. Then the combined loading tools predicted the torsional strength of the deck, showing that a cable stay failure would have precipitated torsional failure of the Morandi Bridge deck.

7.2 Conclusions and Recommendations

Some conclusions about the Morandi Bridge are summarized here. Gaps in the literature are also noted.

- The high sensitivity of corrosion levels to environmental conditions and the variability of corrosion levels throughout the Morandi Bridge cables stays made the precise prediction of corrosion evolution difficult. Corrosion damage for the Morandi Bridge was obtained assuming average corrosion levels throughout the stays, based on observed damage levels after the bridge collapse and assuming the linear progression of corrosion damage. In the absence of fatigue or extreme loads, the Morandi Bridge cable stays were predicted to have reserve capacity in 2018.
- The literature on corrosion of prestressed concrete members was found to be lacking, especially concerning the relationship between the corrosion ingress rate and concrete crack size.
- Fatigue load cycles on the Morandi Bridge cables stays due to truck traffic were predicted to fall below the stress intensity threshold required for fatigue crack growth of steel bridge wires. However, when corrosion pits were assumed to acts as fatigue crack nucleation sites, fatigue damage accumulated rapidly and a low corrosion rate was predicted to cause failure of the Morandi Bridge

cable stays by 2018. It was concluded that prevention of concrete cracking is of utmost importance, as even concrete microcracks may provide ingress of damaging corrosion agents.

- Given the above results, there is a need for corrosion-fatigue coupling in finite element procedures. Experimental results [Sun et al. (2019)] showed that corrosion pits can acts as fatigue crack initiation sites, reducing fatigue life. Current fatigue implementations do not consider this coupling. For complex stress states, such as existed in the cable stays of the Morandi Bridge, a finite element analysis may be most useful, where it is difficult to approximate the alternating stress in tendon reinforcement without excess conservatism.
- The torsional capacity of the Morandi Bridge deck was insufficient to withstand the torsional demand from the collapse of a cable stay. Analysis results from Collins' simple approach [Collins and Mitchell (1991)] were verified with a finite element model of the bridge deck.
- Current approximation procedures for the torsional response of bridge decks approximate multi-celled decks as a single cell, consisting of four shear panels. This idealization can lead to error in the predicted circulatory shear stress within the deck [Dowell and Johnson (2012)]. Fu et. al. [Fu and Tang (2001)] have extended Hsu's softened truss model theory to capture the shear stress within each cell of a multi-cell girder. More work must be done to extend the multi-cell theory to the more prevalent combined load scenario.
- Existing truss models for combined load analysis assume that plane sections remain plane. More work needs to be done to justify this assumption for sections subjected to large torques.

BIBLIOGRAPHY

Beeby, A. (1983). Cracking cover, and corrosion of reinforcement. *Concrete International: Design and Construction*, 5:35–40.

Benscoter, S. U. (1946). Numerical transformation procedures for shear-flow calculation. *Journal of the aeronautical sciences*, 13:438–443.

Bentz, E., Vecchio, F., and Collins, M. (2006). Simplified modified compression field theory for calculating shear strength of reinforced concrete elements. *ACI Structural Journal*, 103:614–624.

Bertolini, L., Elsener, B., Pedeferri, P., Redaelli, E., and Polder, R. (2013). *Corrosion of Steel in Concrete*. Wiley-VCH, Weinheim, Germany.

Bredt, R. (1896). Critical observations on elastic torsion (in german). *Z. Ver. Deut. Ingenieure*, 40:785.

Cairns, J., Plizzari, G., Du, Y., and Franzoni, C. (2005). Mechanical properties of corrosion-damaged reinforcement. *ACI Material Journal*, 102(4):256–264.

Calvi, G. M., Moratti, M., O'Reilly, G. J., Scattarreggia, N., Monteiro, R., Malomo, D., Calvi, P. M., and Pinho, R. (2019). Once upon a time in italy: The tale of the morandi bridge. *Structural Engineering International*, 29:198–217.

Collins, M. P. and Mitchell, D. (1991). *Prestressed Concrete Structures*. Prentice Hall, Englewood Cliffs, New Jersey.

Collins, M. P., Walsh, P., Archer, F., and Hall, A. (1968). Ultimate strength of reinforced concrete beams subjected to combined torsion and bending. *ACI Symposium Publication*, SP-18:379–402.

Dowell, R. K. and Johnson, T. P. (2012). Closed-form shear flow solution for box–girder bridges under torsion. *Engineering Structures*, 34:383–390.

Du, Y., Clark, L. A., and Chan, A. H. (2007). Impact of reinforcement corrosion on ductile behavior of reinforced concrete beams. *ACI Structural Journal*, 104(3):285–293.

Filetto, G. and Lignana, M. (2019). Ponte morandi, la perizia conferma: tiranti corrosi. `https://genova.repubblica.it/cronaca/2019/01/22/news/ponte_morandi_la_perizia_conferma_tiranti_corrosi-217157782/`. Accessed: 20-03-2021.

Forman, R., Kearney, V., and Engle, R. (1967). Numerical analysis of crack propagation in cyclic-loaded structures. *Journal of Basic Engineering*, 89:459–464.

Forman, R. and Shivakumar, V. (1986). Growth behavior of surface cracks in the circumferential plane of solid and hollow cylinders. *Fracture Mechanics*, 17:59–74.

Fu, C. C. and Tang, Y. (2001). Torsional analysis for prestressed concrete multiple cell box. *Journal of Engineering Mechanics*, 127:45–51.

Gerwick, B. and Mehta, P. (1982). Cracking-corrosion interaction in concrete exposed to marine environment. *Concrete International: Design and Construction*, 4:45–51.

Grandt, A. F. (2004). *Fundamentals of Structural Integrity: Damage Tolerant Design and Nondestructive Evaluation*. Wiley.

Greene, G. and Belarbi, A. (2009). Model for reinforced concrete members under torsion, bending, and shear. i: Theory. *Journal of Engineering Mechanics*, 135:970–977.

Habibi, S. (2017). Finite element modelling of corrosion damaged reinforced concrete structures. Master's thesis, University of Toronto.

Hasenjager, K. (2019). Morandi bridge: anaylsis of the ferrometal cctv video clip in six enhanced sequences. `http://www.retrofutur.org/retrofutur/app/main?DOCID=1000116371`. Accessed: 21-02-2021.

Helmerich, R. and Zunkel, A. (2014). Partial collapse of the berlin congress hall on may 21st, 1980. *Engineering Failure Analysis*, 43:107–119.

Hsu, T. T. C. (1968). Ultimate torque of reinforced rectangular beams. *Journal of the Structural Division*, 94:485–510.

Hsu, T. T. C. (1973). Post-cracking torsional rigidity of reinforced concrete sections. *ACI Journal*, 70:352–360.

Hsu, T. T. C. (1984). *Torsion of Reinforced Concrete*. Van Nostrand Reinhold, New York, NY.

Hsu, T. T. C. (1990). Shear flow zone in torsion. *Journal of Structural Engineering*, 116:3206–3226.

Hsu, T. T. C. and Mo, Y.-L. (2010). *Unified Theory of Concrete Structures*. John Wiley & Sons, Chichester, West Sussex, United Kingdom.

Invernizzi, S., Montagnoli, F., and Carpinteri, A. (2019). Fatigue assessment of the collapsed xxth century cable-stayed polcevera bridge in genoa. *Procedia Structural Integrity*, 18:237–244.

Isojeh, B., El-Zeghayar, M., and Vecchio, F. J. (2019). Numerical analysis of reinforced concrete and steel-fiber concrete elements under fatigue loading. *Journal of Structural Engineering*, 145:4019126.

Jang, B. (2018). Bridge rating with considerations for fatigue damage effect from truck overloads. Master's thesis, Illinois Institute of Technology.

Jiang, C., Wu, C., and Jiang, X. (2018). Experimental study on fatigue performance of corroded high-strength steel wires used in bridges. *Construction and Building Materials*, 51:681–690.

Klus, J. P. (1968). Ultimate strength of reinforced concrete beams in combined torsion and shear. *ACI Journal*, 65:210–216.

Lee, H.-S. and Cho, Y.-S. (2009). Evaluation of the mechanical properties of steel reinforcement embedded in concrete specimen as a function of the degree of reinforcement corrosion. *International Journal of Fracture*, 157:81–88.

Lee, Y.-L., Pan, J., Hathaway, R., and Barkey, M. (2005). *Fatigue Testing and Analysis: Theory and Practice*. Elsivier.

Leonhardt, F. (1964). *Prestressed Concrete: Design and Construction*. W. Ernst.

Li, F., Yuan, Y., and Li, C.-Q. (2011). Corrosion propagation of prestressing steel strands in concrete subject to chloride attack. *Construction and Building Materials*, 25:3878–3885.

Liu, Y. and Weyers, R. (1998). Modeling the dynamic corrosion process in chloride contaminated concrete structures. *Cement and Concrete Research*, 28:365–379.

Lou, P., Nassif, H., Su, D., and Truban, P. (2017). Impact of overweight trucks on the service life of bridge girders. *Transportation Research Record*, 2642:103–117.

Lu, Z., Yu, K., and Zhao, Y. (2008). Stochastic modeling of corrosion propagation for service life prediction of chloride contaminated rc structures. In *Proceedings*

of the International Symposium on Life-Cycle Civil Engineering, IALCCE, pages 195–201.

Malomo, D., Scattarreggia, N., Orgnoni, A., and Pinho, R. (2020). Numerical study on the collapse of the morandi bridge. *Journal of Performance of Constructed Facilities*, 34:1–14.

Mitchell, D. and Collins, M. P. (1974). Diagonal compression field theory - a rational model for structural concrete in pure torsion. *ACI Journal Proceedings*, 71:396–408.

Mohammadi, J. and Polepeddi, R. (2000). Bridge rating with consideration for fatigue damage from overloads. *Journal of Bridge Engineering*, 5:259–265.

Morandi, R. (1979). The long-term behaviour of viaducts subjected to heavy traffic and situated in an aggressive environment: The viaduct on the polcevera in genoa. *IABSE Reports of the Working Commission*, 32:170–180.

Morgese, M., Ansari, F., Domaneschi, M., and Cimellaro, G. P. (2019). Post-collapse analysis of morandi's polcevera viaduct in genoa italy. *Journal of Civil Structural Health Monitoring*.

Morinaga, S. (1996). *Remaining life of reinforced concrete structures after corrosion cracking*. E&FN Spon, New York City, NY.

Orgnoni, A. (2019). Revisione critica e modellazione della sequenza di costruzione del viadotto polcevera. Master's thesis, Universita di Pavia.

Paris, P. and Erdogan, F. (1963). A critical analysis of crack propagation laws. *Journal of Basic Engineering*, 85:528–534.

Rabbat, B. G. and Collins, M. P. (1978). A variable angle space truss model for structural concrete members subjected to complex loading. *ACI Symposium Publication*, 55.

Rahal, K. N. and Collins, M. P. (1995). Analysis of sections subjected to combined shear and torsion - a theoretical model. *ACI Structural Journal*, 92:459–469.

Rahal, K. N. and Collins, M. P. (1996). Simple model for predicting torsional strength of reinforced and prestressed concrete sections. *ACI Structural Journal*, 93:658–666.

Rosati, G., Losa, M., and Elsener, B. (2018). Perizia tecnica riguardante prove eseguite su pezzi di detriti del "ponte morandi" in genova (i).

Schupack, M. and Suarez, M. (1982). Some recent corrosion embrittlement failures of prestressing systems in the united states. *PCI Journal*, 27:38–55.

Sirage, M. and Gebreyouhannes, E. (2020). Spalling of concrete cover due to torsion: Examination of advanced theoretical models. In *fib Symposium 2020 Concrete Structures for Resilient Society*, pages 694–701.

Speidel, M. (1974). *Fatigue Crack Growth at High Temperatures*, pages 207–251. Elsivier Scientific, Amsterdam.

Stewart, M. G. and Al-Harthy, A. (2008). Pitting corrosion and structural reliability of corroding rc structures: Experimental data and probabilistic analysis. *Reliability Engineering and System Safety*, 93:373–382.

Sun, J., Ding, Z., and Huang, Q. (2019). Corrosion fatigue life prediction for steel bar in concrete based on fatigue crack propagation and equivalent initial flaw size. *Construction and Building Materials*, 195:208–217.

Vecchio, F. and Collins, M. (1986). The modified compression field theory for reinforced concrete elements subjected to shear. *ACI Journal*, 83:219–231.

Vu, K. and Stewart, M. (2000). Structural reliability of concrete bridges including improved chloride-induced corrosion models. *Structural Safety*, 22:313–333.

Wong, P., Vecchio, F., and Trommels, H. (2013). *VecTor2 & FormWorks User's Manual*.

Woodward, R. J. (1988). Collapse of a segmental post-tensioned concrete bridge. *Transportation Research Record*, 1211:38–59.

Zhu, J., Huang, F., Guo, T., and Song, Y. (2015). Residual life evaluation of prestressed reinforced concrete highway bridges under coupled corrosion-fatigue actions. *Advanced Steel Construction*, 11:372–382.

APPENDIX A

DERIVATION OF SELECT EQUATIONS

Warping Compatibility - Equation 4.16 Figure A.1 shows that a differential element taken from a beam in pure torsion has two deformation components that produce warping: twist and shear.

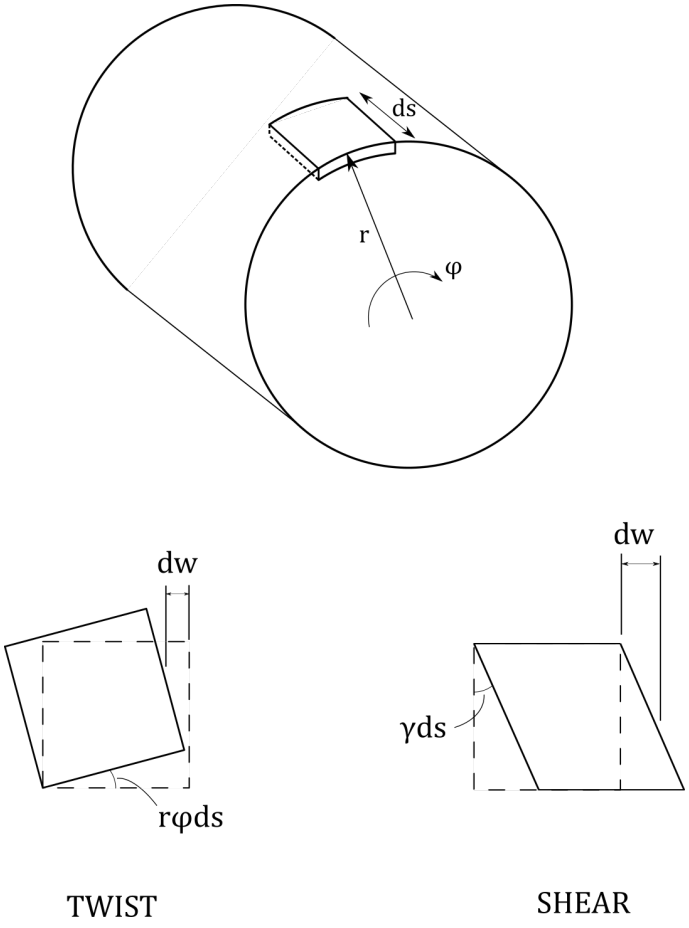

Figure A.1: Twist and shear deformation of a differential element taken from a beam in pure torsion

Warping compatibility requires that the line integral of warping around the surface of the beam must equal zero. Contributions to warping from twist and shear are given:

$$dw_{twist} = r\phi ds\frac{ds}{2} \tag{A.1}$$

$$dw_{shear} = \gamma ds\frac{ds}{2} \tag{A.2}$$

Now, the warping compatibility requirement can be written:

$$\oint dw_{twist} + dw_{shear} = 0 \tag{A.3}$$

$$\oint dw_{twist} + dw_{shear} = \oint \gamma ds - \oint r\phi ds \tag{A.4}$$

Finally, substituting $\oint r\phi = 2A_0$, a relationship is obtained between the shear strain and the twist rate:

$$\oint \gamma ds = 2\phi A_0 \tag{A.5}$$

Prandtl Stress Boundary Conditions for a Thin Tube - Equation 4.18 An expression for the potential energy of the system is given in Eq. A.6 as the internal strain energy minus the work done by external loads.

$$U = \frac{1}{2}\int_A \boldsymbol{\sigma} : \boldsymbol{\epsilon}\, dA - M_T\phi \tag{A.6}$$

Equation A.6 can be made more manageable. Recall from Eq. 4.8 that the only surviving components of the stress tensor, $\boldsymbol{\sigma}$, are the shear stresses with a longitudinal component. These components will be called τ. Similarly, the remaining components of the strain tensor, $\boldsymbol{\epsilon}$, can be written as $\tau/2G$. The differential area, dA, can be written as hds for the thin-walled problem. Finally, the shear stress

can be rephrased in terms of the Prandtl stress function boundary conditions if the membrane analogy is recalled; the slope of the membrane is analogous to the shear stress due to torsion. Approximating the membrane slope as linear for the thin-walled problem results in $\tau = \frac{\Phi_{inner}}{h}$. The potential energy expression is now written in terms of the inner boundary condition:

$$U = \frac{\Phi_{inner}^2}{2G} \oint \frac{ds}{h} - 2\phi A \Phi_{inner} \tag{A.7}$$

The Prandtl stress function at the inside boundary is constant, so the derivative of the potential with respect to Φ_{inner} will equal 0. This operation yields the following result for the inside boundary condition for a single-cell section:

$$\frac{dU}{d\Phi_{inner}} = \frac{\Phi_{inner}}{G} \oint \frac{ds}{h} - 2A\phi = 0 \tag{A.8}$$

$$\Phi_{inner} = \frac{(a-h)h}{2} G\phi \tag{A.9}$$

where a is the outer dimension of a square cell,

h is the wall thickness (assumed constant in Eq. 4.18), and

ϕ is the twist rate per unit length of the member

CFT Compatibility - Equation 4.26 The Compression Field Theory compatibility equation is derived by considering the shear strain that results from three independent strains imposed onto a truss element. The truss element is composed of longitudinal reinforcement, transverse reinforcement and a diagonal concrete strut. The deformed shape due to each deformation is shown in Fig. A.2.

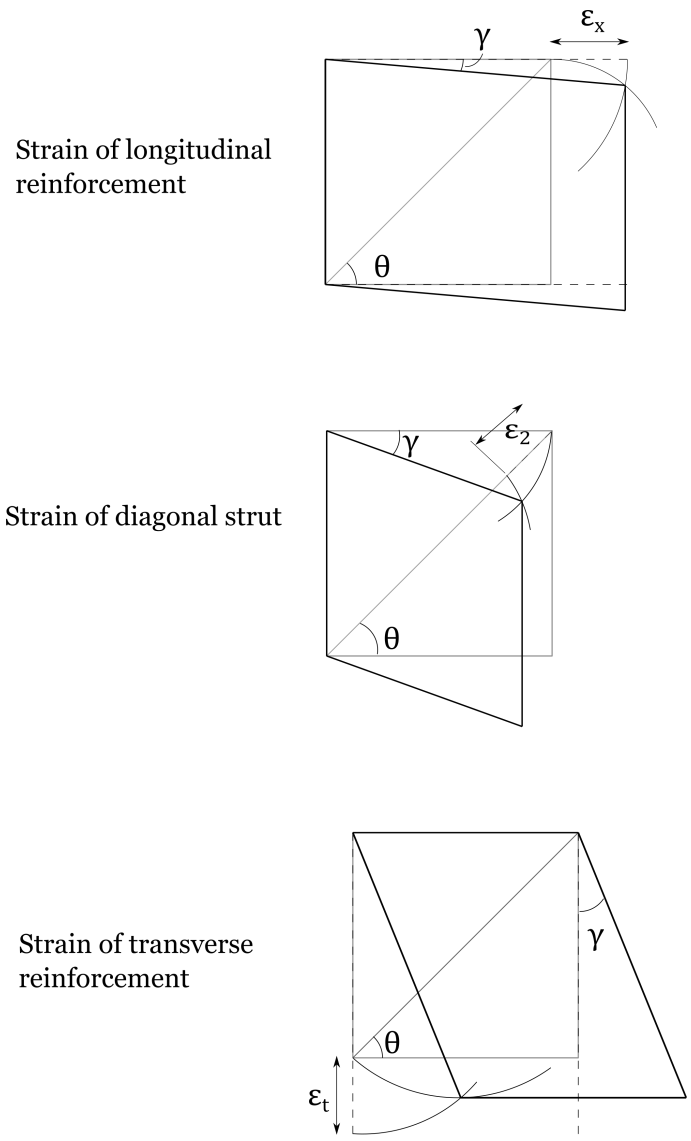

Figure A.2: Deformed shape of a truss element due to three independent strains

Pure longitudinal strain requires the diagonal strut to rotate and maintain its original length. Similar rotations are required for pure transverse strain and diagonal strain, each of which contributes some shear strain to the total shear strain that results from the combination of the three effects.

The shear strains from each of the deformations are given in terms of the strut inclination angle, θ.

$$\gamma_x = \epsilon_x \cot\theta \tag{A.10}$$

$$\gamma_2 = \epsilon_2(\tan\theta + \cot\theta) \tag{A.11}$$

$$\gamma_t = \epsilon_t \tan\theta \tag{A.12}$$

Combination of the three shear strains gives the following total shear strain:

$$\gamma = \gamma_x + \gamma_t + \gamma_2 = (\epsilon_x - \epsilon_2)\cos\theta + (\epsilon_t - \epsilon_1)\tan\theta \tag{A.13}$$

The deformed truss will find the configuration that minimizes Eq. (A.13):

$$\tan\theta^2 = \frac{\epsilon_x + \epsilon_2}{\epsilon_t + \epsilon_2} \tag{A.14}$$

APPENDIX B

VERIFICATION OF TWIST PROGRAM

The torque-twist response of beams with varying wall thickness were obtained by Hsu [Hsu (1973)]. The response of one beam, D4, from his set of experiments is verified using the TWIST program.

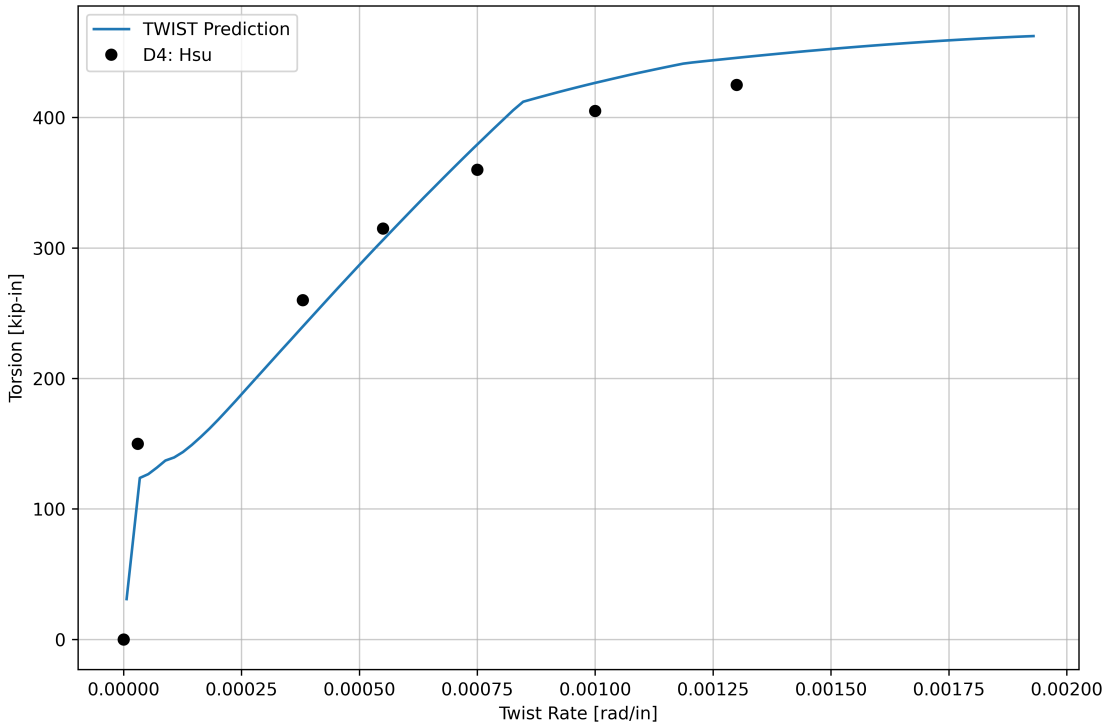

Figure B.1: Predicted torsional response of beam D4, from [Hsu (1973)]

Mitchell and Collins performed experiments to determine the effect of cover thickness on the torsional response of beams. The response of a beam from the experiments, PT6, with 1 9/16" cover is predicted with the TWIST program. The response from TWIST is compared with the response from Rahal's theory [Rahal and Collins (1995)]. Sirage [Sirage and Gebreyouhannes (2020)] comments that state of the art models wildly predict the torsional response of members with thick concrete cover.

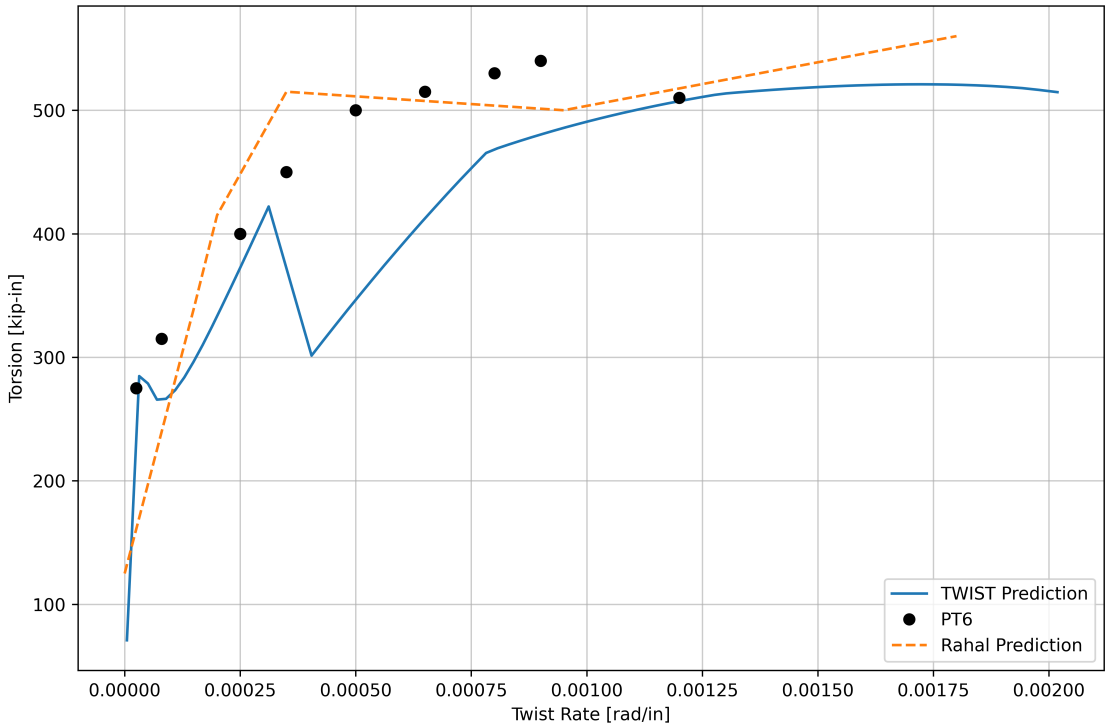

Figure B.2: Predicted torsion response of beam PT6, from [Mitchell and Collins (1974)]

The TWIST program is tested for the torsional response of a box girder from Hsu's textbook [Hsu and Mo (2010)], which used the softened truss model.

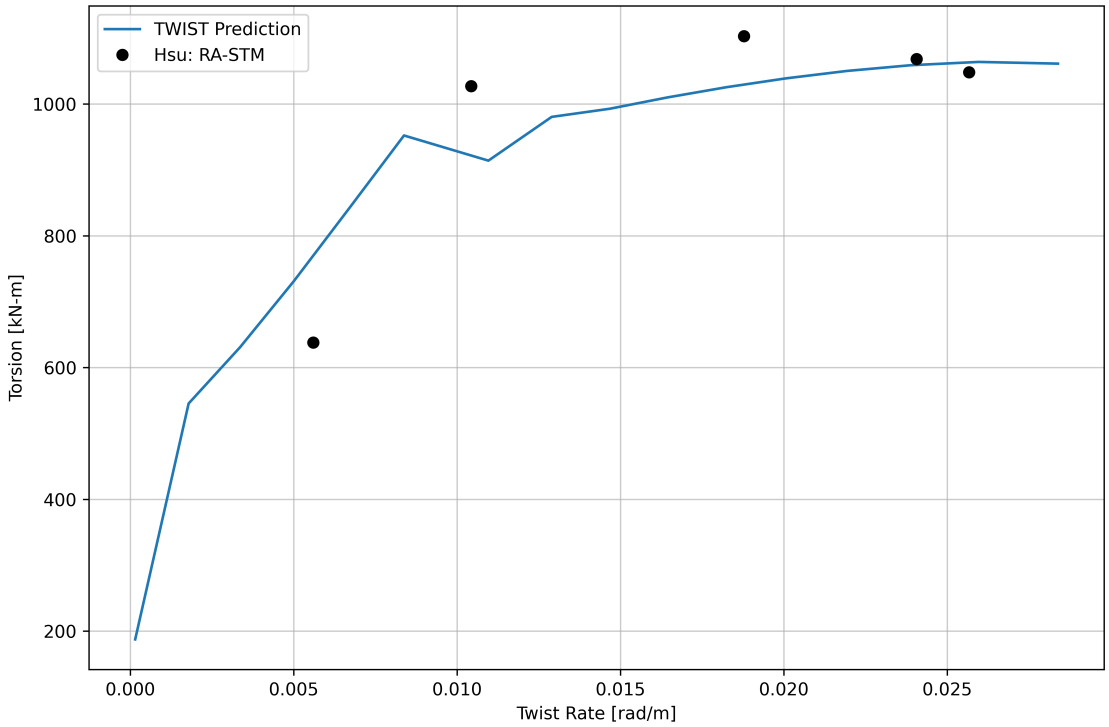

Figure B.3: Predicted torsion response of box-girder, from Hsu and Mo (2010)

APPENDIX C

VERIFICATION OF TOR-SHEAR-N PROGRAM

Klus experimentally obtained the torsional response of beams with various ratios of applied torsion and shear [Klus (1968)]. The responses of three of Klus' beams are predicted by TOR-SHEAR-N. The program struggles to converge for low twist rates.

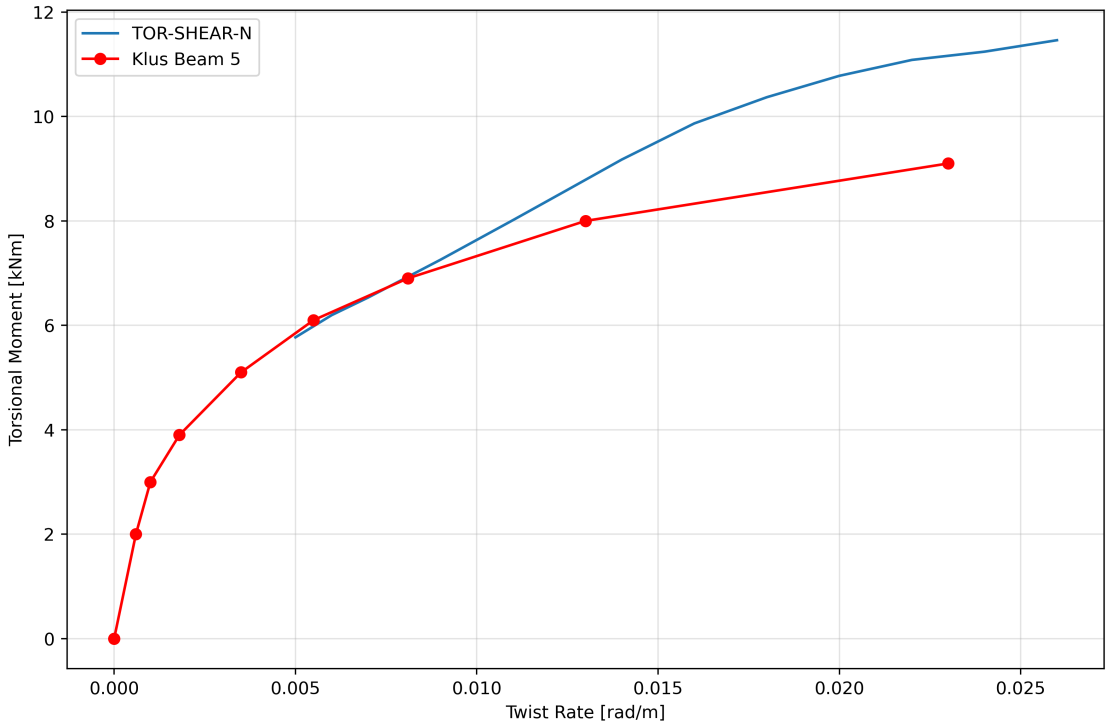

Figure C.1: Predicted torsion response of beam 5, from Klus (1968)

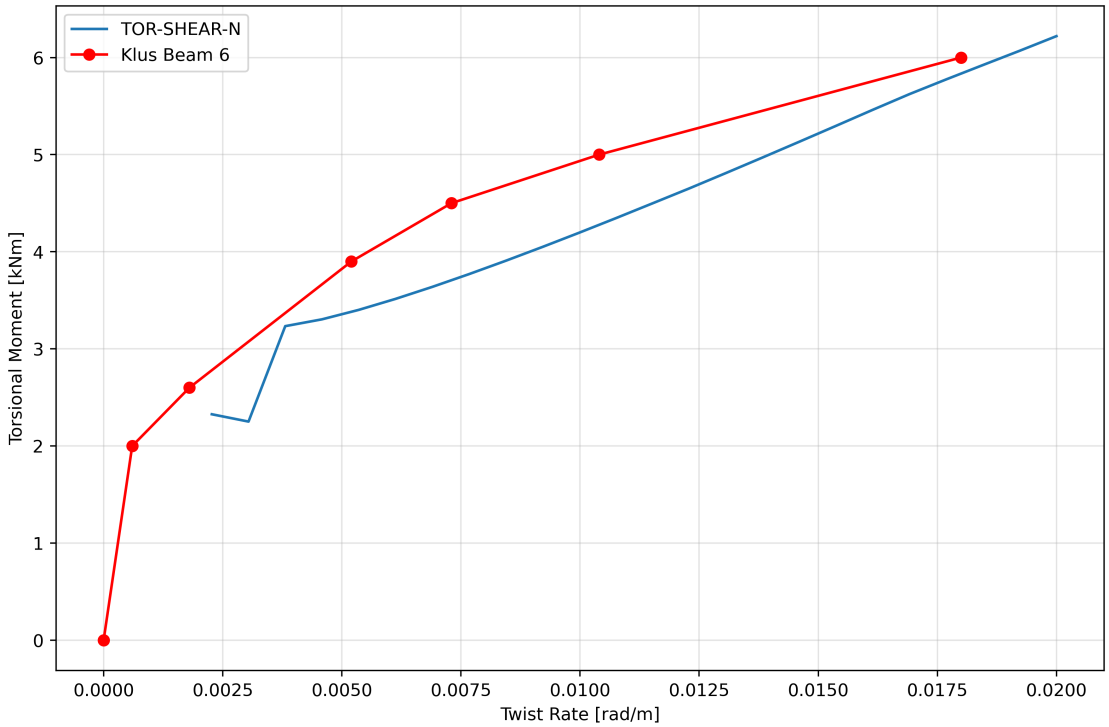

Figure C.2: Predicted torsion response of beam 6, from Klus (1968)

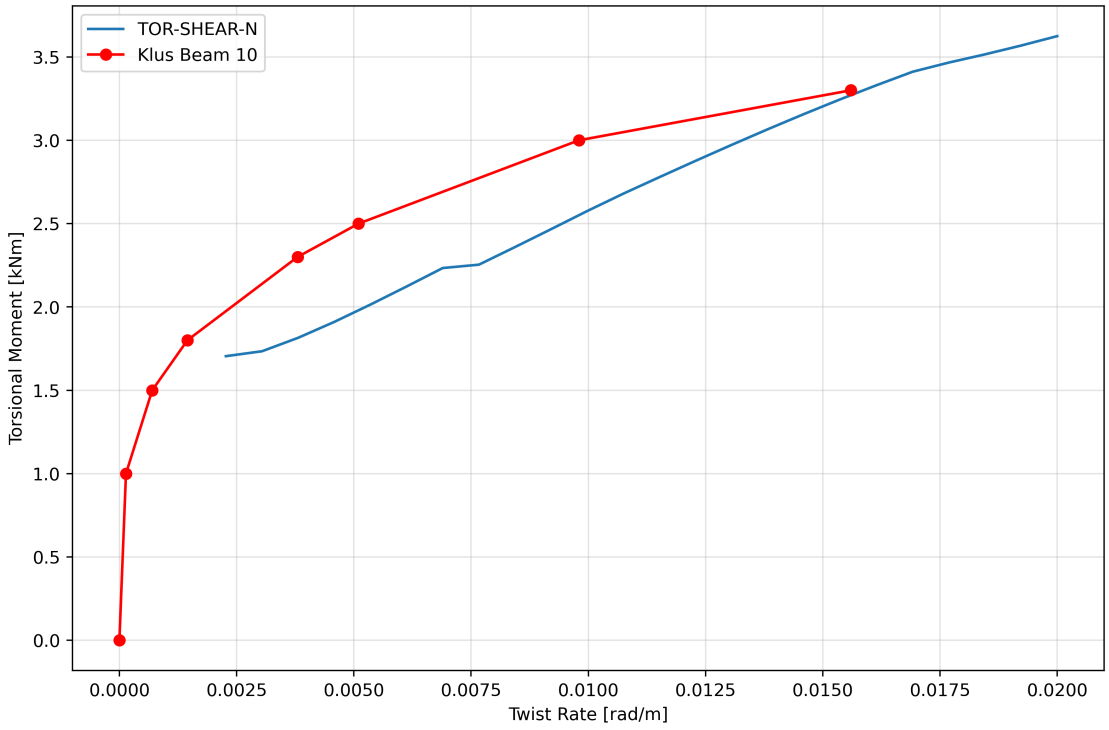

Figure C.3: Predicted torsion response of beam 10, from Klus (1968)